Elektrische Energietechnik an der TU Berlin Band 2

Aris Gkountaras

Modeling Techniques and Control Strategies for Inverter Dominated Microgrids

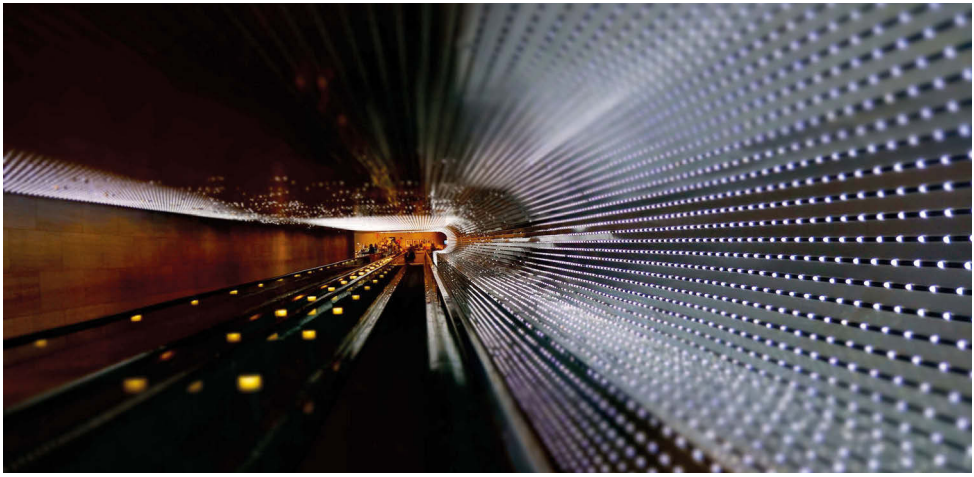

Universitätsverlag der TU Berlin

Technische Universität Berlin

Aris Gkountaras

Modeling Techniques and Control Strategies for Inverter Dominated Microgrids

Die Schriftenreihe *Elektrische Energietechnik* an der TU Berlin wird herausgegeben von:
Prof. Dr. Sibylle Dieckerhoff,
Prof. Dr. Julia Kowal,
Prof. Dr. Ronald Plath,
Prof. Dr. Uwe Schäfer

Elektrische Energietechnik an der TU Berlin | 2

Aris Gkountaras

Modeling Techniques and Control Strategies for Inverter Dominated Microgrids

Universitätsverlag der TU Berlin

Bibliografische Information der Deutschen Nationalbibliothek
Die Deutsche Nationalbibliothek verzeichnet diese Publikation in der Deutschen Nationalbibliografie; detaillierte bibliografische Daten sind im Internet über http://dnb.dnb.de abrufbar.

Universitätsverlag der TU Berlin, 2017
http://verlag.tu-berlin.de

Fasanenstr. 88, 10623 Berlin
Tel.: +49 (0)30 314 76131 / Fax: -76133
E-Mail: publikationen@ub.tu-berlin.de

Zugl.: Berlin, Techn. Univ., Diss., 2016
Gutachter: Prof. Dr.-Ing. Sibylle Dieckerhoff
Gutachter: Prof. Dr.-Ing. Friedrich W. Fuchs
Gutachter: Prof. Dr. Nikos Hatziargyriou
Gutachter: Dr.-Ing. Tevfik Sezi
Die Arbeit wurde am 21. März 2016 an der Fakultät IV unter Vorsitz von Prof. Dr.-Ing. Clemens Gühmann erfolgreich verteidigt.

Umschlagfoto:
Ted Eytan | https://www.flickr.com/photos/taedc/12311698465/
CC BY-SA| https://creativecommons.org/licenses/by-sa/2.0/

Druck: Meta Systems Publishing & Printservices GmbH, Wustermark
Satz/Layout: Aris Gkountaras

ISBN 978-3-7983-2872-3 (print)
ISBN 978-3-7983-2873-0 (online)

ISSN 2367-3761 (print)
ISSN 2367-377X (online)

Zugleich online veröffentlicht auf dem institutionellen Repositorium der Technischen Universität Berlin:
DOI 10.14279/depositonce-5520
http://dx.doi.org/10.14279/depositonce-5520

Contents

Abstract

The character of modern power systems is changing rapidly and inverters are taking over a considerable part of the energy generation. A future purely inverter-based grid could be a viable solution, if its technical feasibility can be first validated. The focus of this work lies on inverter dominated microgrids, which are also mentioned as 'hybrid' in several instances throughout the thesis. Hybrid, as far as the energy input of each generator is concerned. Conventional fossil fuel based distributed generators are connected in parallel to renewable energy sources as well as battery systems. This co-existence of different generator types serves as a means of accelerating the grid integration of inverter-based generators. The main contributions of this work comprise of: The analysis of detailed models and control structures of grid inverters, synchronous generators and battery packs. The utilization of these models to formulate modular control strategies for the distributed generators of medium voltage microgrids and evaluate their performance in real time simulation test scenarios. The first control strategy involves the development of a synchronization technique for grid forming inverters. Secondly, achieving load sharing among distributed generators employing conventional droop control is analyzed. Furthermore, the problem of transient load sharing between grid forming units with different time constants is addressed. The transient response of the microgrid upon a load step change is optimized with a developed control modification for grid forming inverters. The negative effect of transient load sharing is in this way minimized, in parallel with evaluating the case of more than one inverters working in parallel. Moreover, a control algorithm is introduced that incorporates the grid secondary control to primary control. In this way, load sharing is influenced by the state of charge of battery packs and a certain level of grid autonomy can be achieved. Finally, the developed microgrid structures are tested in fault conditions: A short circuit strategy is developed for grid forming and feeding inverters. The main guideline for the short circuit strategy is that the fault isolation should be based on traditional protection means. Therefore the developed control modifications should not be based on communication between generators and maximizing the short circuit current is the main objective. For grid forming units, various current limiting methods are compared in standalone and parallel operation. Its components overrating and the parallel operation with a synchronous generator are investigated. For the grid feeding inverters, the reactive current injection strategy is optimized through the proposed mixed current injection with the objective of maximizing its fault current contribution.

Kurzfassung

Die Struktur der modernen Energieversorgung hat sich in den letzten Jahrzehnten massiv geändert. Dezentrale Generatoren, die auf Wechselrichtern basieren, übernehmen einen großen Teil der Energieerzeugung. Ein ausschließlich wechselrichterbasiertes Netz wäre ein realistischer Ansatz, wenn seine technische Machbarkeit verifiziert werden könnte. Der Fokus dieser Arbeit liegt auf wechselrichterdominierten Inselnetzen, welche auch als 'hybride' Netze bezeichnet werden, da die primäre Energieversorgung von konventionellen Kraftstoffen und erneuerbaren Energien kommt. Die Untersuchung der Koexistenz von unterschiedlichen dezentralen Generatoren kann die Integration von erneuerbaren Energien beschleunigen. Die wichtigste Beiträge dieser Arbeit sind: Die Analyse von Modellen und Regelstrukturen von Netzwechselrichtern, Synchrongeneratoren und Batterieanlagen. Die entwickelten Modelle werden verwendet, um Regelstrategien für dezentrale Generatoren in Mittelspannungsinselnetzen zu formulieren. Ihre Funktionsweise wird mittels Echtzeitsimulation validiert. Die erste Strategie ist eine Synchronisationsmethode für netzbildende Wechselrichter. Zweitens wird die Leistungsaufteilung in Mittelspannungsinselnetzen mittels Droop Regelung analysiert. Weiterhin erfolgt die Untersuchung der transienten Lastaufteilung zwischen netzbildenden Einheiten mit unterschiedlichen Zeitkonstanten. Die dynamische Reaktion eines Inselnetzes wird durch eine Regelungsmodifikation für die netzbildenden Wechselrichter optimiert. Dadurch werden die Oszillationen während der transienten Lastaufteilung minimiert. Beim Betrieb mehrerer paralleler Wechselrichter wird der Einfluss der Netzimpedanz auf die transiente Lastaufteilung analysiert. Die dritte entworfene Regelstrategie umfasst die Integration der Sekundärregelung in die Primärregelung. Der Ladezustand von Batterien wird mit der Lastaufteilung gekoppelt, um die Autonomie des Netzes zu stärken. Abschließend wird eine Kurzschlussstrategie für netzbildende und netzspeisende Wechselrichter entwickelt. Die grundlegende Richtlinie ist, dass die Fehlerisolation auf traditionellen Schutzmaßnahmen basieren sollte. Ziel der Strategie ist die Maximierung des Kurzschlussstromes. Als zusätzliche Randbedingung soll keine Kommunikation zwischen Generatoren stattfinden. Verschiedene Strombegrenzungsmethoden für netzbildende Wechselrichter werden im Einzel- und Parallelbetrieb mit einem Synchrongenerator verglichen. Für den netzspeisenden Wechselrichter wird die Blindstromeinspeisung mit dem vorgestellten Prinzip der gemischten Stromeinspeisung optimiert, um den Betrag des Fehlerstroms zu maximieren.

1 Introduction

The german term 'Energiewende' is becoming more and more international over the years. This term could be briefly translated as the transition of electrical energy production from conventional fossil fuel based electrical generation means to more environmental friendly and therefore sustainable solutions, such as renewable energy sources. Most of such regenerative sources are interfaced to the grid through inverters. Upon connecting more and more of such inverters, conventional power plants should be disconnected, or operated for less hours during the day. These conventional power plants are based mostly on electrically excited synchronous generators that possess enormous rotating masses. These masses are coupled with the grid frequency and are exploited in favor of grid stability. By disconnecting such generators, and integrating to the grid robust inverter-based generators a significant amount of technical challenges arise. One of the key challenges is grid operational planning. This is an inherent problem of the integration of volatile energy sources that deliver stochastically their energy input to the grid. This energy generation should be ideally coordinated with load demand. However, generation and load planning is not the focus of this thesis. The focus lies mainly on a shorter time range, namely on the transient response of inverter dominated grids after a disturbance. The goal is to demonstrate that power electronics based generators can cooperate smoothly with each other and with conventional synchronous generators.
More specifically, this work concentrates on the investigation of transient operational issues of medium voltage hybrid microgrids. The term microgrid is first introduced in [1] and describes "a cluster of loads and microsources operating as a single controllable system that provides both power and heat to its local area". In this work heat interchanges between microgrid components are not considered, and only power flow between generators and loads is investigated. The term hybrid refers to the hybrid energy sources included in the investigations [2], [3], which combine renewable energy based sources with conventional fossil fuel based distributed generators. To balance excessive power generation from the renewable energy sources, storage means are required. Only battery-based solutions are here investigated, whereas also thermal storage could also be an economically viable solution. In the case of microgrids, the inverters should take over most of the grid supporting functions that normally conventional generators possess. It is typical for the majority of standalone real microgrids to assign the role of grid forming units to diesel generators [3]. The focus of this thesis lies on shifting the role of grid support to inverter-interfaced units. It was first shown in [4], more than four decades ago, that voltage source inverters

can work on grid forming mode, namely produce and stabilize a three phase microgrid of variable voltage and frequency. Working on a similar direction, in this thesis the priority is set to the detailed control structure of distributed generators that are responsible for grid control. In conventional grids, control is applied in various time scales, such as primary, secondary and tertiary control [5], [6]. This hierarchical structure is organized as follows: Primary control is the inner control structure of each distributed generator, ensuring stable grid operation in steady state and transients. The objective of secondary control is to restore frequency to its nominal operating point. In emerging microgrid structures secondary control for voltage is also introduced [6]. Tertiary control is applied to regulate power flows within different grid interconnections, such as e.g. two interconnected microgrids. The contributions of this work are located only in the area of primary and secondary control.
There are two main concepts for the control objectives of any grid interfaced inverter [5]. The first one, the grid feeding mode, is when the main objective is to control the DC-link voltage at its input. In this way, the energy balance of the DC-link remains intact, and the full amount of power that reaches the DC-link is tried to be 'fed' to the grid. In modern power systems, all renewable energy sources are interfaced to the grid through a grid feeding inverter. Under the principle of maximum power point tracking (MPPT), the power electronic components that connect the renewable energy sources to the grid should maximize their power output, independent of other loads or generators conditions. The second one, is the grid forming mode, when the inverter controls the output voltage and frequency, trying to 'form' an autonomous grid. In this case, the energy flow coming out from the DC-part of the inverter is determined through the grid demands. In case of power excess, e.g. when the regenerative sources are feeding-in their rated power and the load is relatively low, the grid forming inverter should feed this excess energy to its storage element. On the other hand, if there is a lack of energy, e.g. the regenerative sources are not feeding any power to the grid and simultaneously there is an increased load demand, the storage element of the grid forming inverter should cover the load needs.
Load sharing between grid forming units is a significant aspect of any grid structure. In this work, despite the fact that microgrids are considered a new and alternative grid topology, a conventional control scheme is utilized to achieve load sharing, namely droop control. Droop control has been successfully the backbone of modern power systems and the means of achieving load sharing without any communication means between synchronous generators since the introduction of the first AC grids. Its operation has been thoroughly analyzed for conventional synchronous generators [7]. In this work, the same concept that applies for conventional generators is implemented for grid forming inverters. The suitability of droop control is further investigated for the parallel operation of grid forming inverters with synchronous generators.

Thesis structure

The thesis is organized as follows:

- Chapter 2 starts with the fundamentals of grid stability and power sharing. Grid stiffness and the various power sharing concepts for microgrids are briefly explained. Furthermore, the derivation of droop control is analyzed and its suitability for medium voltage microgrids is investigated.
- In chapter 3 the core of this work is presented, the distributed generators models and control structures. An electrically excited synchronous generator operating as a controlled diesel generator is firstly introduced. The grid inverters follow, in their both possible configurations, namely in grid feeding or grid forming mode. Their control structure is formed and the respective controllers are designed, identifying their appropriate control plants. The model of a battery-based distributed generator is further analyzed, which comprises of battery cells as well as a DC/DC converter for controlling the output DC voltage. Finally, the transition to real time simulation is explained, accompanied with the necessary modifications to the models previously explained.
- In chapter 4, the first control strategy of this work is introduced, which is a straight forward synchronization scheme for grid forming inverters. This control scheme enables any grid forming inverter to connect smoothly to an existing grid, without the presence of any unwanted transient effects. The black start of a medium voltage microgrid once with the synchronous generator working as the master generator, and once the grid forming inverter is also documented to demonstrate the superiority of inverter-interfaced grid forming units.
- In chapter 5, load sharing between grid forming units is investigated. The necessary derivations for implementing droop control for grid forming inverters are documented. The problem of transient load sharing between grid forming units with different time constants is introduced. A control strategy is then developed, which successfully broadens the spectrum of any possible step load change that the microgrid can withstand. Transient load sharing with more than one grid forming inverters in parallel is further analyzed. Furthermore, a new control algorithm for battery based grid forming inverters is proposed, which couples the state of charge (SoC) of battery packs with the selection of setpoints for droop control. The introduced control algorithm is called SoC-Adaptive droop control, since the setpoints of droop control of the grid forming inverter are 'adapted' according to the SoC level of the battery pack in the DC part of the distributed generator. In this way, the autonomy of the grid is increased, since SoC-Adaptive droop control is a means of secondary control, and is incorporated in primary control without any communication means between generators.
- The last contribution of this work is the formulation of a short circuit strat-

egy for the inverter-interfaced distributed generators, explained in chapter 6. Starting from the grid forming inverters, several current limiting methods are presented and analyzed. The two most promising are implemented in real time simulation scenarios, to compare their robustness in standalone operation, as well as their stability in parallel operation with a synchronous generator. Furthermore, overrating grid forming inverter's components is investigated in test scenarios that involve complex microgrid topologies. As far as the grid feeding inverters are concerned, the state of the art for fault-ride-through (FRT) in stiff grids is first presented. Then, the reactive current injection strategy is further analyzed in the case of medium voltage microgrids and implemented in test scenarios. The limits of this strategy are identified, and a control modification is proposed, namely the principle of mixed current injection, with the clear objective of maximizing the fault current.

- The last chapter is devoted to summarizing the main points of this work as well as discussing further research points that can be developed from the results of this thesis.

The main attributes of the operating strategies proposed in this thesis can be observed in Fig. 1.1. In this figure the major contributions of this work are classified based on three factors: (*i*) their investigation focus, (*ii*) the required modeling depth for the power electronic components and (*iii*) the time scale of interest.

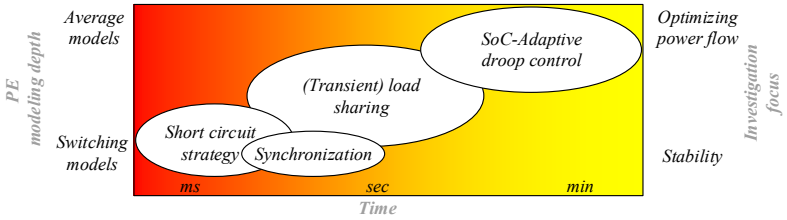

Fig. 1.1: Classification of proposed operational strategies

The modeling depth of power electronic components is directly coupled with the time scale of interest. Starting from the short circuit strategy, switching models for the power electronic components are needed since the investigations are focused at a time frame of as low as a few milliseconds. Stable operation as well as the maximization of the fault current are the objectives of the strategy. Moving on the synchronization technique for grid forming inverters, stability should be also in this case validated in a short time focus, since connecting a generator to the grid is considered a transient disturbance. The problematic of transient load sharing between grid forming units with different time constants, which expands up to a time frame of a few seconds, is further investigated. The

investigation focus lies on both ensuring that the grid remains stable after such a severe disturbance, as well as maintaining power sharing among generators. Therefore, the power flow is also in this case considered. Finally, the SoC-Adaptive droop control is located in a different time and investigation focus. In that case, average models of power electronics components or even ideal voltage and current sources could be deployed, since the objective is to optimize the power flow in the area of secondary control, from tens of seconds up to several minutes of operation. In this work, real time simulation is selected to validate the proposed models and control strategies. With this selection a degree of freedom is obtained as far as modeling is concerned, since the simulation duration of complex models is further reduced with the use of a powerful real time simulator. Furthermore, the developed models can be deployed for hardware in the loop (HIL) applications, where hardware demonstrators can be connected in parallel with simulation models, to accelerate model prototyping [8], [9].

2 Stability and power sharing fundamentals

The theoretical investigations in this chapter focus on the vital foundation of any type of electrical network, its grid forming units. Similar to mainland grids, also in the case of microgrids for reliability issues more than one grid forming units should be at all times present. The interactions of such ideal grid forming units working in parallel are evaluated in this section. Ideal means at this point that the inner electrical, mechanical, or control delays are neglected, and these units can regulate the voltage and frequency in their output with no restrictions. The conditions for power sharing as well as voltage and frequency stability are investigated. The coupling of grid forming units is based on droop control which is first theoretically derived and its limitations for the implementation in medium voltage microgrids are investigated. Before analyzing however the fundamentals of power sharing, it is necessary to comment on the terms grid stability and stiffness, which characterize any type of grid. Grid feeding units are in this chapter omitted and are considered as a part of the overall load of the microgrid.

2.1 Grid stability principles

The decisive criterion for any operating strategy developed for modern power systems is grid stability. Power system stability is defined in [10] as "the property of a power system to remain in a state of operating equilibrium under normal operating conditions and to regain an acceptable state of equilibrium after being subjected to a disturbance". In the following section two important points deriving from the definition of stability of a power system are further discussed, namely how can stability be validated, and what type of disturbances can be employed for this validation.
System stability is analyzed in order to verify the feasibility of the strategies proposed in this work. Throughout this thesis stability is validated through two different methods depending on the modeling detail of grid components: *(i)* In this chapter, where only ideal distributed generators are considered, system stability is verified through small signal stability analysis. The physical coupling between generators is analytically calculated and system stability around an operating

point is validated by analyzing the behavior of the eigenvalues of the characteristic matrix of the system. Stability analysis of an equilibrium can be also investigated through the identification of a Lyapunov function, in other words proving Lyapunov stability. An alternative would be applying mathematical theorems to the characteristic matrices of the sytem, such as the Routh-Hurwitz criterion for linear time-invariant (LTI) systems [11]. *(ii)* On the other hand, when detailed modeling of the grid components is required, analytical derivations of stability can become cumbersome. In that case, real time simulation scenarios are prepared, which include in-depth models of distributed generators. The modeling techniques in the direction of real time simulation are found in chapter 3.
As far as the power system disturbances are concerned, the disturbance type is dependent on the time focus of each investigation. In the case of small signal stability analysis small disturbances are applied in all system variables for the analysis of the system eigenvalues. In the real time simulation scenarios that follow in the next chapters the disturbances have various attributes as far as time scale and intensity are concerned: starting from the synchronization of a unit and a (step) load change, to more severe disturbances such as grid faults. An attribute directly linked to the transient response of a system and therefore stability is grid stiffness, which is further analyzed in the next section.

Grid stiffness

Grid stiffness in general is defined as the capability of the grid to preserve its voltage and frequency stability during and after the presence of a disturbance. More specifically, stiffness at a certain grid point is determined traditionally in power systems through short circuit power: the power that flows through that grid node in case of a short circuit. Considering a distributed energy generator to be connected to a grid, the term "short circuit ratio" at its point of common coupling (PCC) is further introduced. The short circuit ratio is defined as the short circuit power that flows to the PCC, divided by the rated power of the generator. The two decisive factors for the calculation of the short circuit power at a certain PCC are (i) the grid impedance connecting the PCC to the rest of the grid and (ii) the characteristics and limitations of the existing grid components. Fig. 2.1 shows distributed energy resources (DER) connected to two grid configurations with different stiffness.
Fig. 2.1a shows the integration of a distributed generator to a voltage bus which is connected through a reactance to an ideal voltage source. That could be the case of a high voltage grid with the distributed energy resource, typically coupled through a step-up transformer to the medium or low voltage level. The ideal voltage source represents a grid feeder as a standard representation used for power system stability studies. The short circuit power in such a configuration can be calculated if the connecting terminals of the feeder are short-circuited. The lower the value of the grid reactance X_g the higher the amount of short

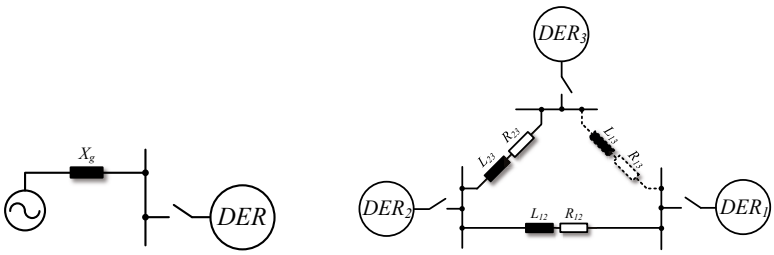

(a) a stiff grid (b) a weak grid

Fig. 2.1: Typical network examples

circuit current reaching the terminals of the feeder. Typical stiff grids are considered with a short circuit ratio of more than 5 [10]. In such electrical networks the distributed generator to be connected does not have a major influence on grid stability. On the other hand, the grid structure shown in Fig. 2.1b possesses different attributes. That would normally be a case of a radial grid in medium or low voltage level. An alternative to the radial configuration is the meshed structure, where the distributed generators are connected with distribution lines not only to the loads but also to each other. In this way, grid reliability increases, since in case of a line malfunction, the faulted line can be disconnected and the majority of the loads remain unaffected from this separation. In Fig. 2.1b the distribution line that closes the ring of the three distributed generators is dashed to demonstrate the variant of a meshed configuration. Meshed structures are however not common in distribution grids up to 100kV, since 85 % of the distribution grid level is radial, realized as open-ring formations [12]. Both radial and meshed configurations are considered in this work to demonstrate that the control strategies proposed are independent of the grid topology.
There are a few attributes that classify this network as a weak grid. First of all, there is no feeder present. There is no ideal voltage source that can guarantee voltage and frequency stability as well as a high short circuit power. This microgrid is based only on distributed generators that typically have low short circuit power. Furthermore, the grid impedances are no more inductive with low values, such as X_g, but high impedances with an ohmic and an inductive part, Rij and Lij respectively, where i, j denote the generators connected through the line. This leads to a severe change as far as power sharing and therefore frequency and voltage control are considered. In summary, in such a grid structure, generators behavior and response are strongly interconnected and a transient disturbance affects all grid participants. Therefore, such a microgrid is considered a worst case scenario for the control challenges of distributed generators which should take over the majority of grid supporting functions.

2.2 Power sharing in microgrids

After the introduction of the concept of grid stiffness, the goal of power sharing among multiple generators should be further analyzed. In any modern power system the presence of multiple generators is required for reliability issues. To ensure proper system operation and controllability, the load of the grid should be equally distributed among the generators . This load distribution is named power sharing and is a vital concept of any electrical grid.

Power sharing definition Power sharing is defined as the operating steady state point where the active and reactive power output of all generators present in the grid are being governed by the following equations:

$$\frac{P_1}{x_1} = \frac{P_2}{x_2} = \frac{P_3}{x_3} = \ ... \ = \frac{P_i}{x_i} \tag{2.1}$$

$$\frac{Q_1}{y_1} = \frac{Q_2}{y_2} = \frac{Q_3}{y_3} = \ ... \ = \frac{Q_i}{y_i} \tag{2.2}$$

where: $1,2,3...i$ is the number of generators connected, P_i, Q_i is the active and reactive power output of each generator respectively and x_i, y_i design factors that rule power sharing. In case that a proportional power sharing is desired, the design factors are selected equal to the rated power of each generator, namely $x_i = y_i = S_i$.

In case power sharing fails, it is certain that the grid will be led to instability, since the limitations of the generators will cause severe transient disturbances. Primary control is typically responsible for achieving power sharing, as the first level of control of each distributed generator. There are various concepts to achieve proportional power sharing, that can be classified in three different variants, as shown in figures 2.2 & 2.3, *(i)* Droop control, *(ii)* central control and the *(iii)* master-slave principle. In the case of droop control, only local measurements are needed to achieve power sharing. Local measurements means that each generator has a controller that requires only parameters measured at its point of common coupling (PCC). In Fig. 2.2 the implementation of droop control for the case of three generators of a radial microgrid is shown. For simplification purposes the load is considered central, the droop control concept however would achieve sufficient results also for the case of distributed loads. The index $i = 1...3$ stands for each generator, V & I are the voltage and current at the output of each generator (single or three-phase) and V^* & δ^* are the voltage amplitude and angle references that each generator should apply at its output to achieve proportional power sharing. With dashed lines additional measured signals required for each local controller are depicted, such as for the case of synchronous generators, their rotational speed.

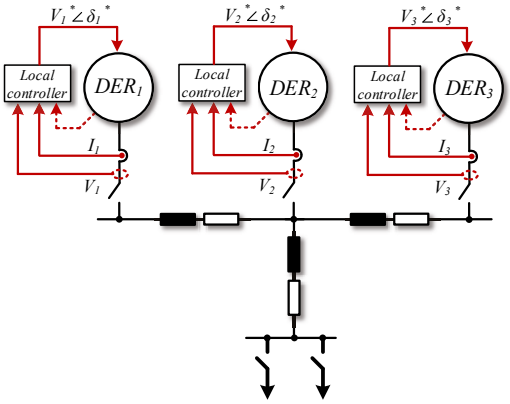

Fig. 2.2: Power sharing achieved through droop control

Both alternatives to droop control are based on rapid information exchange between generators [13–16]. The first one considers flat hierarchy between generators. All measurements are processed through a central controller unit that calculates and delivers the required setpoints for each generator. Voltage and current measurements for the load, V_L and I_L respectively, might be also needed for power sharing optimization purposes, but are not a prerequisite, therefore drawn with dashed lines in Fig. 2.3a. The inner local controllers of each generator are omitted in Fig. 2.3. Typical industry products for microgrids are central controllers that receive and react upon local measurements at various grid feeders [17–19].
The other alternative for power sharing is not based on flat hierarchy between generators. One generator is assigned as the master unit and receives the majority of the measured signals. This master unit calculates the references for all generators of the microgrid and sends the respective commands to the slave units, see Fig. 2.3b. The implementation principle can change, depending on the grid topology as well as the attributes of the distributed generators. The slave units can operate in both grid feeding and grid forming mode.
A proper comparison of the performance of the three control concepts exceeds the focus of this work. Droop control is chosen for the first control level of the grid forming units and the reason is twofold:

- Reliability: Droop control is the only primary control concept that can operate without any means of robust communication. This provides a significant advantage in comparison with both alternatives which in communication failure can no longer ensure grid stability. Communication of slower dynamics is only required in the case of droop control for the secondary

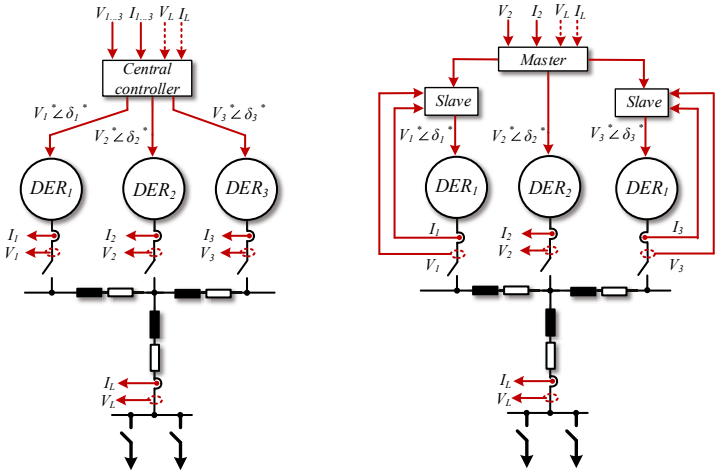

(a) with a central controller (b) with the master-slave principle

Fig. 2.3: Power sharing through communication

and tertiary level of control. If this communication fails grid stability is further maintained, as long as the power reserves of the generators allow it.

- Smoother integration of inverter-dominated grids: A priority in this work is to compare inverter-based with conventional distributed generators and accelerate their integration. Therefore, it needs to be validated that inverter-based distributed generators can overtake all grid services that synchronous generators have provided with conventional means for more than a few decades [10]. Droop control is a fundamental attribute of modern power systems and therefore choosing it for the primary control of grid forming inverters will not alter the rest of the traditional grid structure.

2.2.1 Derivation of droop control

Droop control has been successfully implemented not only for synchronous generators in modern power systems but also for inverter-based grids, [20], [21]. The following section focuses on the derivation of droop control, starting from power calculation between two bus bars, A and B with a distribution line in-between, as shown in Fig. 2.4. The objective of this section is to demonstrate the inherent connection between active power, P to frequency, f and reactive power, Q to voltage, V. This interconnection can be exploited to achieve load sharing be-

tween distributed generators only with the help of local measurements at their PCC.

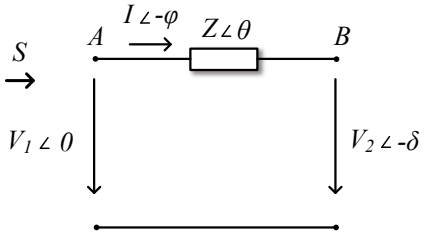

Fig. 2.4: Voltage bus bars with a distribution line

The complex apparent power for the single phase system of Fig. 2.4 is as following calculated:

$$\bar{S} = P + jQ = \bar{V_1} \cdot \bar{I}^* = \bar{V_1}(\frac{\bar{V_1} - \bar{V_2}}{\bar{Z}})^* = V_1(\frac{V_1 - V_2 \cdot e^{j\delta}}{Ze^{-j\theta}}) = \frac{{V_1}^2}{Z}e^{j\theta} - \frac{V_1 V_2}{Z}e^{j(\theta+\delta)} \tag{2.3}$$

The real and imaginary part of equation (2.3) can be extracted, providing the expressions for active and reactive power calculation.

$$\begin{aligned} P &= \tfrac{{V_1}^2}{Z}\cos\theta - \tfrac{V_1 V_2}{Z}\cos(\theta+\delta) \\ Q &= \tfrac{{V_1}^2}{Z}\sin\theta - \tfrac{V_1 V_2}{Z}\sin(\theta+\delta) \end{aligned} \tag{2.4}$$

Bearing in mind that the distribution line has the following parameters:

$$Ze^{j\theta} = R + jX \tag{2.5}$$

The equations (2.4) are transformed to:

$$\begin{aligned} P &= \tfrac{V_1}{R^2+X^2}[R \cdot (V_1 - V_2\cos\delta) + \mathrm{X} \cdot V_2 \sin\delta] \\ Q &= \tfrac{V_1}{R^2+X^2}[-R \cdot V_2 \sin\delta + \mathrm{X}(V_1 - V_2\cos\delta)] \end{aligned} \tag{2.6}$$

Trying to solve equations (2.6) for voltage and angle, which are the main variables to be tuned from the control algorithm, one obtains:

$$\begin{aligned} V_2 \sin\delta &= \tfrac{XP - RQ}{V_1} \\ V_1 - V_2\cos\delta &= \tfrac{RP + XQ}{V_1} \end{aligned} \tag{2.7}$$

Concluding from equations (2.7) it can be clearly noted that V_i and δ, voltage amplitude and angle respectively, are both coupled with active and reactive power, and further assumptions should be made in order to decouple the parameters of the system. The first assumption is that the distribution line between the voltage buses is predominantly inductive. That is the case of high voltage lines, where conventional generators are commonly connected. In this perspective, the resistance can be neglected for further calculations. In our case, where medium voltage lines are considered, the line impedance attributes are further investigated in the next section. For completing the calculations, the conventional assumption of high voltage lines is considered. The inductive character of the lines results also in the simplification of the trigonometric functions of Eq. 2.7 since the voltage angle is relatively small.

$$X >> R \qquad \sin\delta \approx \delta \qquad \cos\delta \approx 1 \tag{2.8}$$

Based on these assumptions, equations (2.7) can be simplified to the following form:

$$\begin{aligned} \delta &= \tfrac{XP}{V_1 V_2} \\ V_1 - V_2 &= \tfrac{XQ}{V_1} \end{aligned} \tag{2.9}$$

At this point, it can be observed that the voltage angle is coupled only with active power, and the difference of the voltage amplitude defines the reactive power flow through the line. Equations (2.9) can be therefore further exploited to form the first level of control of each conventional synchronous generator in modern power systems, namely primary control. Primary control typically involves only the coupling of active power with voltage angle and therefore frequency. However, in the case of microgrids, it is advantageous to couple also reactive power with voltage amplitude to optimize reactive power sharing. By introducing frequency and voltage amplitude deviation and coupling them with active and reactive power respectively, the following equation can be formed:

$$\begin{aligned} \omega - \omega_0 &= -k_p(P - P_0) \\ V_1 - V_0 &= -k_q(Q - Q_0) \end{aligned} \tag{2.10}$$

Active power is therefore 'drooped' from the angular frequency deviation, and reactive power is drooped from the voltage deviation, with the so-called droop gains, k_p and k_q respectively. To perform this action a nominal point is considered, where at the nominal angular frequency and voltage amplitude, ω_0 and V_0, the generator should provide a set of setpoints for the power, namely P_0 & Q_0. Droop control is typically graphically depicted, as shown in Fig. 2.5. The maximum angular frequency deviation, $\Delta\omega$ voltage amplitude deviation ΔV, as well as the maximum reactive power provision from each generator, ΔQ are further discussed in the following chapters. For simplicity reasons, in the next sections in the graphical representation of droop control, the angular frequency ω is replaced by frequency f. The transient response of any system of droop controlled

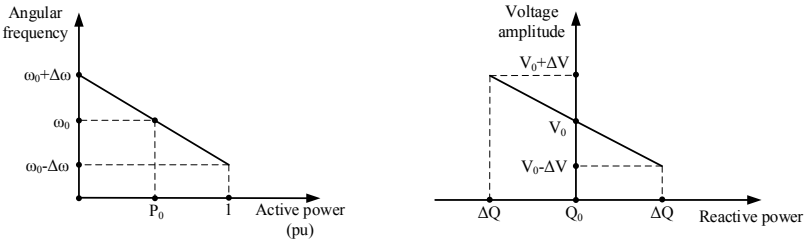

(a) P/ω (b) Q/V

Fig. 2.5: Theoretical droop characteristics

generators can be tuned by adjusting the droop control gains, depending on the dynamics of the investigated grid structure. Before selecting appropriate droop gains however, the assumption of inductive lines is further investigated in the next section for the case of medium voltage microgrids.

2.2.2 Line impedance determination

For the derivation of the fundamental equations of droop control, given in Eq. 2.10, it has been assumed that the connecting path between both voltage buses is mainly inductive. In this section the line impedance ratio is more precisely calculated for the case of medium voltage microgrids. The two voltage buses of Fig. 2.4 are for this investigation replaced by a microgrid with two distributed generators working in parallel. The generators are considered ideal and are modeled as voltage sources that are connected through distribution lines to a central load. The lines have an ohmic and inductive impedance part, as shown in Fig. 2.6 with R_i, L_i. A step up transformer is also included in this analysis, depicted only with its leakage inductance L_{Ti}. The range of parameters used in this sec-

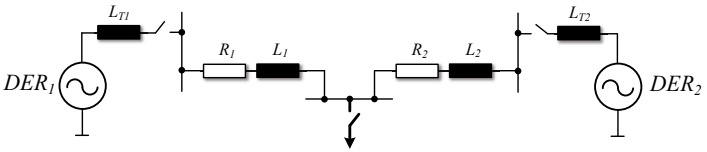

Fig. 2.6: Typical microgrid with two generators

tion are summarized in Table 2.1. The focus lies on calculating the impedance ratio of such a generic microgrid, and not identifying a worst case scenario, since

a flexibility on the microgrid topology for the investigations of the next chapters is desired. For simplification purposes, the rated power of the distributed generators is considered equal. It is assumed that the generator connecting voltage

Variable	Value
Generator voltage (kV)	$[\ 0.69 - 3.3\ ]$
Generator rated power (MVA)	$[\ 1 - 10\ ]$
Transformer short-circuit impedance (pu)	0.05
Line cable inductance ($mH\ per\ km$)	$[\ 0.296 - 0.363\ ]$
Line cable resistance ($\Omega\ per\ km$)	$[\ 0.0467 - 0.09\ ]$

Table 2.1: System parameters range

increases in a linear manner with the rated power. The inductance and resistor range is defined by $1kV$ and $10kV$ cable datasheets [22], [23]. The inductance remains almost constant with decreasing voltage, the resistance however increases its value with lower voltages. The upper limit corresponds to the $1kV$ cable.

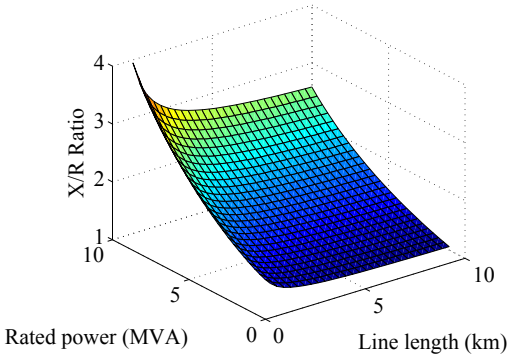

Fig. 2.7: Variation of line impedance

It can be observed from Fig. 2.7 that the impedance ratio is always higher than 1, but not high enough so that the resistive part can be neglected. In low voltage grids, the impedance would be mainly resistive, causing problems in the effectiveness of the implementation of droop control [24], [25]. Alternative droop control concepts have been already introduced for resistive networks, which couple different variables depending on the impedance, or try to estimate the grid impedance [25,26]. Another alternative solution proposes using a phase angle droop characteristic for the active power sharing [27]. However, in that case, higher droop gains are required, that in turn affect the system stability and require also a supplementary control loop to overcome this problem. Furthermore, it has been already shown in [28] that with decreased impedance ratio and therefore more resistive grid impedances, the poles of a system of droop

controlled ideal generators connected in the same voltage bus are shifted closer to, or into the right half-plane, causing instability. To get a further insight on the system dynamics, a small signal stability analysis is performed to evaluate the suitability of droop control in medium voltage microgrids and the allowed range of droop gains.

2.2.3 Small signal stability analysis

Small signal stability analysis can be a useful method to analyze the behavior of a system for small disturbances around a steady state point. It has already been a powerful tool to analyze the parallel transient behavior of synchronous machines in the past [7] and recently transfered to the stability analysis of droop controlled inverters [29]. Similar to [29], small signal stability analysis for a medium voltage standalone microgrid is performed, to derive necessary conclusions on the selection of droop characteristics for both control loops, active power to frequency P/f and reactive power to voltage Q/V. When implementing droop characteristics, selecting appropriate droop gains is a criterion that determines the transient response of the system. To identify stable and non stable regions, small signal analysis of a two ideal generators system is performed. Starting from the typical droop equations, as defined in Eq. 2.10, and for simplification purposes selecting zero setpoint for the active and reactive power:

$$\omega = \omega_0 - k_p P \tag{2.11}$$

$$V = V_0 - k_q Q \tag{2.12}$$

where ω and ω_0 are the actual and the nominal angular frequency respectively and V and V_0 are the actual and nominal voltage amplitude respectively. A low pass filter is introduced for the measurement of active and reactive power, to introduce a form of virtual inertia to the inverter. In this way, the inverter-based distributed generator will not react to each instantaneous change of P and Q. The low pass filter equations, Eq. 2.13 & 2.14 are given with the help of the Laplace transformation:

$$P_{meas}(s) = \frac{\omega_f}{s+\omega_f} P(s) \tag{2.13}$$

$$Q_{meas}(s) = \frac{\omega_f}{s+\omega_f} Q(s) \tag{2.14}$$

where ω_f is the corner frequency of the low pass filter, selected identical for both P and Q. The Laplace transformation is selected for the calculation of the low pass filter to ease the derivative calculation performed in the next equations.
Considering small disturbances around the steady state and integrating the low pass filter for power measurement, equations (2.11) and (2.12) can be linearized:

$$\begin{aligned}\Delta\omega(s) &= -\tfrac{k_p\omega_f}{s+\omega_f}\Delta P(s)\\ \Delta V(s) &= -\tfrac{k_q\omega_f}{s+\omega_f}\Delta Q(s)\end{aligned} \tag{2.15}$$

and in the time domain the following equations are obtained:

$$\begin{aligned}\Delta\omega &= -\omega_f\Delta\omega - k_p\omega_f\Delta P\\ \Delta V &= -\omega_f\Delta V - k_q\omega_f\Delta Q\end{aligned} \tag{2.16}$$

The voltage vector at the connecting terminals of each generator is further defined through Fig. 2.8 and Eq. 2.17 & 2.18. Linearizing Eq. (2.18) for δ, the

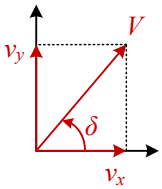

Fig. 2.8: Voltage vector coefficients

$$\overrightarrow{V}_i = v_{xi} + jv_{yi} \tag{2.17}$$

where i denotes generator numbering, in our case $i = 1,\ 2$

$$\begin{aligned}v_x &= V\cos(\delta)\\ v_y &= V\sin(\delta)\\ \delta &= \arctan(\tfrac{v_y}{v_x})\end{aligned} \tag{2.18}$$

angular position of the voltage V:

$$\Delta\delta = \tfrac{\partial\delta}{\partial v_x}\Delta v_x + \tfrac{\partial\delta}{\partial v_y}\Delta v_y \tag{2.19}$$

Due to Eq. (2.18), Eq. (2.19) can be transformed to:

$$\Delta\delta = -\tfrac{v_y}{{v_x}^2+{v_y}^2}\Delta v_x + \tfrac{v_x}{{v_x}^2+{v_y}^2}\Delta v_y \tag{2.20}$$

Since

$$\Delta\omega = \Delta\delta \tag{2.21}$$

the following equation can be deduced based on (2.20) and (2.21)

$$\Delta\omega = -\tfrac{v_y}{{v_x}^2+{v_y}^2}\Delta v_x + \tfrac{v_x}{{v_x}^2+{v_y}^2}\Delta v_y \tag{2.22}$$

Linearizing once more, now the equation (2.17) transforms to

$$\Delta V = \tfrac{v_x}{\sqrt{{v_x}^2+{v_y}^2}}\Delta v_x + \tfrac{v_y}{\sqrt{{v_x}^2+{v_y}^2}}\Delta v_y \tag{2.23}$$

and it follows that its derivative can be directly calculated:

$$\Delta V = \tfrac{v_x}{\sqrt{{v_x}^2+{v_y}^2}}\Delta v_x + \tfrac{v_y}{\sqrt{{v_x}^2+{v_y}^2}}\Delta v_y \tag{2.24}$$

Solving the system of the above equations for the derivatives of the voltage coefficients and angle, one obtains:

$$\Delta v_x = \frac{n_y}{m_x n_y - m_y n_x}\Delta\omega + \frac{m_y n_x \omega_f}{m_x n_y - m_y n_y}\Delta v_x + \frac{m_y n_y \omega_f}{m_x n_y - m_y n_x}\Delta v_y + \frac{k_q m_y \omega_f}{m_x n_y - m_y n_x}\Delta Q \quad (2.25)$$

$$\Delta v_y = \frac{n_x}{m_y n_x - m_x n_y}\Delta\omega + \frac{m_x n_x \omega_f}{m_y n_x - m_x n_y}\Delta v_x + \frac{m_x n_y \omega_f}{m_y n_x - m_x n_y}\Delta v_y + \frac{k_q m_x \omega_f}{m_y n_x - m_x n_y}\Delta Q \quad (2.26)$$

bearing in mind that:

$$m_x = -\frac{v_y}{{v_x}^2+{v_y}^2} \qquad m_y = \frac{v_x}{{v_x}^2+{v_y}^2} \qquad n_x = \frac{v_x}{\sqrt{{v_x}^2+{v_y}^2}} \qquad n_y = \frac{v_y}{\sqrt{{v_x}^2+{v_y}^2}} \quad (2.27)$$

Using equations (2.16), (2.25), & (2.26) the state space equations of the system can be derived, which describe the behavior of each generator in case of small disturbances around a steady state point.

$$\begin{bmatrix} \Delta\omega \\ \Delta v_{xi} \\ \Delta v_{yi} \end{bmatrix} = [M_i] \begin{bmatrix} \Delta\omega \\ \Delta v_{xi} \\ \Delta v_{yi} \end{bmatrix} + [C_i] \begin{bmatrix} \Delta P_i \\ \Delta Q_i \end{bmatrix} \quad (2.28)$$

where the auxiliary matrices M_i and C_i are defined as follows:

$$\Big[M_i\Big] = \begin{bmatrix} -\omega_f & 0 & 0 \\ \frac{n_y}{m_x n_y - m_y n_x} & \frac{m_y n_x \omega_f}{m_x n_y - m_y n_y} & \frac{m_y n_y \omega_f}{m_x n_y - m_y n_x} \\ \frac{n_x}{m_y n_x - m_x n_y} & \frac{m_x n_x \omega_f}{m_y n_x - m_x n_y} & \frac{m_x n_y \omega_f}{m_y n_x - m_x n_y} \end{bmatrix} \quad (2.29)$$

$$\Big[C_i\Big] = \begin{bmatrix} -k_p\omega_f & 0 \\ 0 & \frac{k_q m_y \omega_f}{m_x n_y - m_y n_x} \\ 0 & \frac{k_q m_x \omega_f}{m_y n_x - m_x n_y} \end{bmatrix} \quad (2.30)$$

By deriving the nodal admittance matrix equation and combining it with the state space equations (2.28) the characteristic matrix A of the system can be found. In Eq. 2.31 the definition of the characteristic matrix of a scalar system is given:

$$\Big[\Delta \mathrm{X}\Big] = [A]\,[\Delta \mathrm{X}] \quad (2.31)$$

In our investigations, $X = [\ \Delta\omega,\ \Delta v_{xi},\ \Delta v_{yi}\ ]$, as already given in Eq. 2.28.
A parameter sweep can now be performed, to investigate the stability of the

eigenvalues of the characteristic matrix. Considering the system of the two generators in Fig. 2.9, the nodal admittances matrix can be obtained. The angle of the first generator is chosen equal to zero to minimize the variables involved in the calculation.

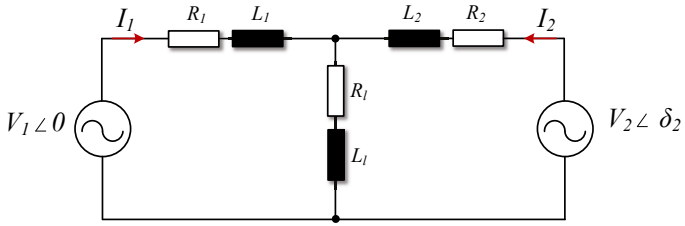

Fig. 2.9: Two ideal generators feeding a load

where:

$$Z_1 = R_1 + j\omega L_1 \quad , \quad Z_2 = R_2 + j\omega L_2 \quad , \quad Z_l = R_l + j\omega L_l \tag{2.32}$$

represent the impedances of the distribution lines and the load, δ_2 the voltage angle of the second generator, V_1, V_2 and I_1, I_2 the voltage and current amplitudes of both generators respectively. The following equation, Eq. (2.33) gives the admittance matrix of the system, calculated from the line and load impedances.

$$\begin{bmatrix} \bar{I}_1 \\ \bar{I}_2 \end{bmatrix} = \begin{bmatrix} \frac{Z_l+Z_2}{(Z_l+Z_1)(Z_l+Z_2)-Z_l^2} & -\frac{Z_l}{(Z_l+Z_1)(Z_l+Z_2)-Z_l^2} \\ -\frac{Z_l}{(Z_l+Z_1)(Z_l+Z_2)-Z_l^2} & \frac{Z_l+Z_1}{(Z_l+Z_1)(Z_l+Z_2)-Z_l^2} \end{bmatrix} \begin{bmatrix} \bar{V}_1 \\ \bar{V}_2 \end{bmatrix} \tag{2.33}$$

or, in its compact form:

$$[I] = [Y][V] \tag{2.34}$$

Defining vector coefficients for the current similar to the voltage (Eq. 2.17 & 2.18), the active and reactive power can be calculated:

$$P_i = v_{xi} i_{xi} + v_{yi} i_{yi}, \quad , \quad Q_i = v_{xi} i_{yi} - v_{yi} i_{xi} \tag{2.35}$$

Considering small disturbances from a steady state point, Eq. 2.35 can be transformed to:

$$[\Delta S] = [I][\Delta v_i] + [V_i][\Delta I] \tag{2.36}$$

Substituting in (2.28), the transfer matrix A of the system is can be fully de-

scribed, where K_s is an auxiliary matrix consisting only from ones and zeros.

$$[A] = ([M_s] + [C_s]([I_s] + [V_s][Y_s])[K_s]) \tag{2.37}$$

The index s introduced in Eq. 2.37 denotes system, since the angle, voltage and power expressions for each generator are now merged in a single matrix that describes the full system of two generators. By finding the eigenvalues of the matrix A, we can derive the necessary conclusions for the stability of our system in small deviations from the steady state. In Table 2.2 the steady state parameters of a specific operation point are given. The linearization takes place around this system operating point:

Variable	Value
Voltage V_1 (V)	$2685 + 0i$
Voltage V_2 (V)	$2651 + 205i$
Impedance Z_1 (Ω)	$0.01 + 0.0165i$
Impedance Z_2 (Ω)	$0.01 + 0.0165i$

Variable	Value
Current I_1 (A)	$265.5 - 78.95i$
Current I_2 (A)	$261.9 + 37.8i$
Impedance Z_l (Ω)	$5 + 0.5i$

Table 2.2: Steady state parameters

The operation point is selected arbitrarily, whereas a selection of a different steady state point should not influence the results of the small signal stability analysis [29]. A 3.3 kV system is considered. The eigenvalues of the characteristic matrix are plotted for a different set of droop gains and lengths of the distribution lines connecting both generators. In this way, the stability of the system upon implementing droop control can be verified and the limitations, as far as droop gains are concerned, can be derived. These limitations can be used in the next chapters where more complex microgrids are formed.

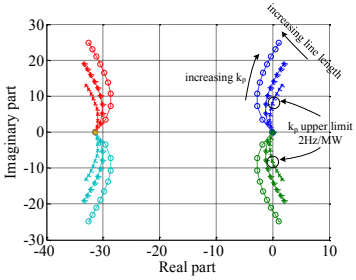

Fig. 2.10: Root locus for k_p sweep

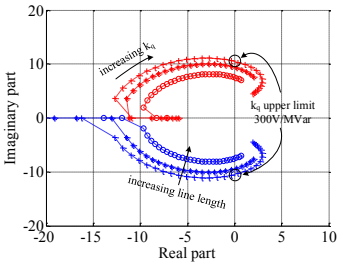

Fig. 2.11: Root locus for k_q sweep

Observing Fig. 2.10 and 2.11 useful conclusions can be drawn on the selection of appropriate droop gains for our system. In Fig. 2.10 a parameter sweep of the

droop gain for the P/f characteristic is performed, for three different distribution line lengths, $L = [1,\ 5,\ 10]$ km between the generators and the eigenvalues of the system are drawn. The system matrix given in Eq. 2.37 has 6 eigenvalues, only 4 of them are depicted in Fig. 2.10 since the other two have negligible values. The different colors stand for different eigenvalue of the matrix. Important for our observations are the eigenvalues that have a positive real part, which could lead to system instability. In Fig. 2.11 only two eigenvalues are shown, which by increasing k_q penetrate the right real positive part of the root locus. From the intersection of the eigenvalues with the imaginary axis, the upper limits for k_p and k_q can be obtained respectively. It is shown that the system matrix eigenvalues experience a different change depending on droop gains and line lengths. It can be observed that for longer distribution lines the limits for droop gains that ensure stable operation increase. In other words, it is demonstrated that for shorter lines, the generators coupling increases and smaller droop gains are required to achieve same stability performance. This line lengths conclusion is also verified with a poles-zeros stability consideration in [30]. Figures 2.10 & 2.11 are not employed to calculate suitable droop gains that can deliver the most stable transient response of the system, yet identify the allowed regions of droop gains that can be employed in a system. Furthermore, the two-generators-system used in this section does not cover the whole spectrum of possible microgrid configurations. However, when the system is expanding with longer distribution lines, the limitations for the droop gains derived from the small signal stability analysis also expand. Therefore, the two generators system is considered from this perspective a worst case scenario.
The small signal stability analysis demonstrated that even in the case of medium voltage lines, conventional droop control can deliver a stable response. Therefore, it is selected as the first level of control for the grid forming units and responsible for ensuring load sharing. Its performance will be evaluated in the real time simulation scenarios of the next chapters.

3 Generator modeling and control

The generators are an essential part of the microgrid. Their modeling requirements for investigations in system-level, as well as the analysis of their control structure is the focus of this chapter. A detailed overview is given about the two most common type of generators:

- Synchronous generator based distributed generators: A model of an electrically excited synchronous generator is in detail presented and analyzed. This model can be employed to represent the characteristics of a diesel generator, which prevail in real microgrids, such as islanded grids.
- Inverter-based distributed generators: The focus of this work lies on the interfacing element of these generators to the grid, namely the inverter. A classification is performed according to its control objective to grid feeding and grid forming mode of operation. The DC part of the inverter is further modeled in detail in the case of grid forming mode of operation with a battery pack.

3.1 Diesel generator

The diesel generator is modeled as an electrically excited synchronous generator, as shown in Fig. 3.1. There are two control loops present: The automatic voltage regulator (AVR) and the speed governor. Both control loops apply the droop characteristics explained in Eq. 2.10 for active and reactive power, where Q_g is the reactive power measured at the output of the generator and P_{set} the droop control setpoint.

3.1.1 Electrical and mechanical part

There are several methods of modeling an electrically excited synchronous generator depending on the analysis depth required for the investigations. The synchronous generator consists of two main components: the armature and field windings. The field winding is supplied with direct current to produce a magnetic field which induces alternating voltages in the armature windings. When three-phase currents flow through the armature winding, a magnetic field in the air-gap rotating at synchronous speed will be created. The field winding is placed in the rotor of the machine. To acquire steady torque both fields must

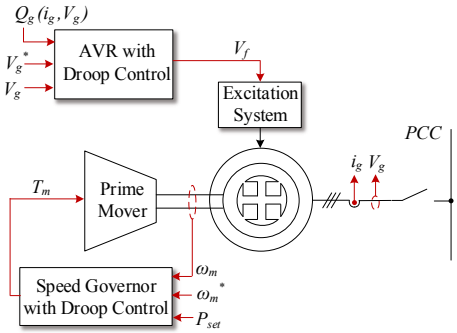

Fig. 3.1: Control structure of synchronous generator

rotate at the same speed, namely the synchronous speed of the machine.
Two axes are defined to identify the characteristics of a synchronous machine. The direct (d) axis, centered magnetically in the center of the north pole of the stator and the quadrature (q) axis, 90 degrees ahead of the d-axis. An alternative would be to choose the (q) axis to lag the (d) axis by 90 degrees [10]. The interconnection between the three-phase (abc) system and the selected dq system is shown in Fig. 3.2. The rotor position relative to the stator is defined by the angle θ between the (d) axis and the magnetic axis of phase α winding, see Fig. 3.2. To develop the equations of the synchronous machine the following assumptions are made:

- The distribution of the stator's windings is considered sinusoidal along the air-gap, as far as the interaction with the rotor is concerned.
- The stator slots cause no variation of the rotor inductances with rotor position.
- Magnetic hysteresis and saturation effects are negligible.

Fig. 3.2 shows the circuits involved in the analysis of the operation of the machine. The rotor circuits comprise of field and amortisseur (or damper) windings, as shown in the left sub-figure of Fig. 3.2. The field winding is considered to be connected with a source of direct current, I_{fd} whereas the current flowing through the amortisseur windings is assumed circulating in two sets of closed circuits in the d- and q-axis, I_{kd} and I_{kq} respectively. These short-circuited windings are intended to damp out speed oscillations. The machine model developed in this section is oriented to the structure and operation of a salient-pole machine. The parameters of Fig. 3.2 are explained in Table 3.1 [1] & 3.2.

[1]The notation for the voltage amplitude in this section, "E", is used, in compliance with the typical literature notation on machine modeling. In the rest of this work the symbol "V" is preferred.

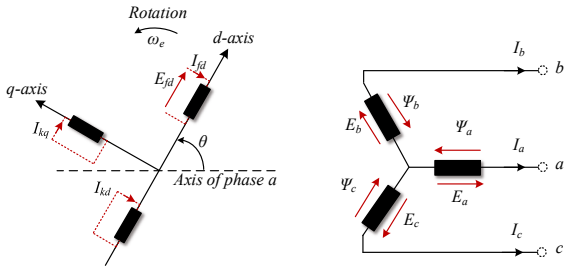

Fig. 3.2: Coupling of dq and abc equivalent circuits

The core of the machine model is the dq-circuit based on the L_{ad} reciprocal pu system [10], [31] as shown in Fig. 3.3. In this system, the base current in any rotor circuit is defined as the current which induces in each phase 1 *pu* voltage induced by the mutual inductance L_{ad} [10]. This circuit represents the electrical characteristics of the machine.

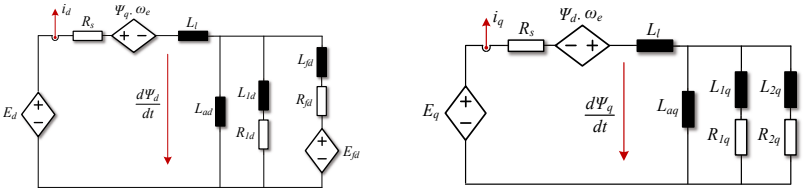

Fig. 3.3: DQ equivalent circuit

Variable	Description
E_{dq}	Induced terminal voltage
Ψ_{dq}	Flux linkage
f_d	Field winding
k_d & k_q	$d-$ & $q-$axis amortisseur circuit
k	1,2... n; n=no. of amortisseur circuits
ω_e	Rotor angular velocity

Table 3.1: Machine parameters in dq & description

The pu base units are summarized in Table A.1. An important observation on calculating impedances in pu values is that inductances and reactances are the same when calculated in pu. In the described model, time is also in pu, which affects all integrators in the model. The dq equivalent circuit parameters given

Variable	Description
L_l & R_s	Self inductance & resistance of stator winding
L_{adq}	DQ components of mutual inductance between stator & rotor windings
L_{1dq} , L_{2dq}	Self inductances of DQ amortisseur circuits
L_{fd} & R_{fd}	Self inductance & resistance of rotor circuit
L_{dq}	DQ-axis synchronous reactance

Table 3.2: DQ equivalent parameters

in Table 3.2, which are also called *fundamental* or *basic* parameters, cannot be directly measured from the machine terminals. Instead, it is common to list in the datasheet the *operational* parameters of the machine, which can be obtained through a variety of experimental methods, such as open-circuit (OC) and short-circuit (SC) tests. The operational parameters, given in Table 3.3 are in pu and similar expressions apply also for the q-axis. The coupling of the

Variable	Description
$T_{d0}^{'}$	D-axis OC transient time constant
$T_{d}^{'}$	D-axis SC transient time constant
$T_{d0}^{''}$	D-axis OC sub-transient time constant
$T_{d}^{''}$	D-axis SC sub-transient time constant

Table 3.3: Datasheet parameters required

fundamental machine parameters, such as the rotor and stator inductances and resistors, with the *operational* parameters is based on interconnecting the stator and rotor circuits with the incremental values of terminal quantities, as shown in Fig. 3.4. More specifically, by examining the machine response under small perturbations (this is denoted through the suffix Δ) the operational parameters can be derived.
Introducing $G(s)$, the stator to field transfer function and L_{dq}, the operational d- and q-axis inductance, Figure 3.4 can be quantified in Eq. 3.1 & 3.2.

$$\Delta\Psi_d(s) = G(s)\Delta E_{fd}(s) - L_d\Delta i_d(s) \tag{3.1}$$

$$\Delta\Psi_q(s) = -L_q\Delta i_q(s) \tag{3.2}$$

where s is the Laplace operator. For the d-axis equivalent, the analytical expression for $L_d(s)$ can be calculated from the left part of Fig. 3.3 and Eq. 3.1 and written in factored form in Eq. 3.3. The analytical mathematical derivation can be found in [10].

$$L_d(s) = L_d\frac{1+(T_4+T_5)s+T_4T_6s^2}{1+(T_1+T_2)s+T_1T_3s^2} \approx L_d\frac{(1+sT_d^{'})(1+sT_d^{''})}{(1+sT_{d0}^{'})(1+sT_{d0}^{''})} \tag{3.3}$$

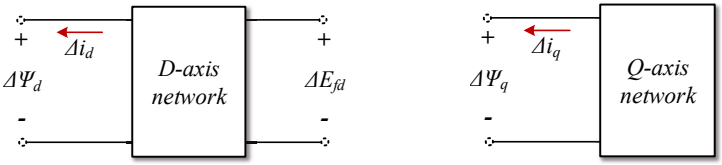

Fig. 3.4: d- and q-axis networks identifying terminal quantities

where:

$$
\begin{aligned}
T'_{d0} = T_1 &= \frac{L_{ad}+L_{fd}}{R_{fd}} \\
T''_{d0} = T_3 &= \frac{1}{R_{1d}}(L_{1d}+\frac{L_{ad}L_{fd}}{L_{ad}+L_{fd}}) \\
T'_{d} = T_4 &= \frac{1}{R_{fd}}(L_{fd}+\frac{L_{ad}L_{l}}{L_{ad}+L_{l}}) \\
T''_{d} = T_6 &= \frac{1}{R_{1d}}(L_{1d}+\frac{L_{ad}L_{l}L_{fd}}{L_{ad}L_{l}+L_{ad}L_{fd}+L_{fd}L_{l}}) \\
L_{ad} &= L_d - L_l
\end{aligned}
\tag{3.4}
$$

Similar expressions apply also for the q-axis equivalent circuit. The parameters that appear in Eq. 3.4 are named in Table 3.3 and can be directly obtained from the machine datasheet. The missing parameters of Table 3.2 can be calculated solving the $5x5$ system of Eq. 3.4.
The developed model in the dq rotating reference frame has to be able to connect with all other models in a three-phase system. Therefore, a controlled current source is developed as shown in Fig. 3.5]. The inherent problem of this interconnection scheme is that no inductive component can be directly connected at its output. This can be easily bypassed by using a large resistive component in parallel with the inductive element.

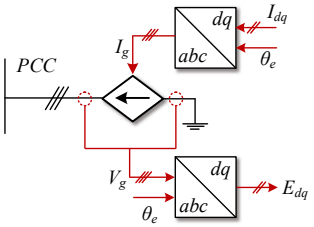

Fig. 3.5: DQ model connection

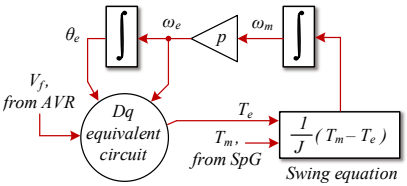

Fig. 3.6: Model of the mechanical part

The electrical torque T_e, seen as an output of the dq equivalent circuit in Fig. 3.6, is directly calculated in the dq equivalent circuit as given in the following equation:

$$T_e = \Psi_d i_q - \Psi_q i_d \tag{3.5}$$

In Fig. 3.6 the *SpG* stands for speed governor.

3.1.2 Controller design

Both control loops of the diesel generator are shown in Fig. 3.7 and 3.8[2]. All parameters are in pu with the base units given in Table A.1. For the automatic voltage regulator (AVR) a simplified mathematical model of the AC5A brushless excitation system based model, as defined in [32], is implemented. The simplifications are performed due to the modeling focus of the synchronous generator [33]:

- The load compensator and power factor controller terms are not implemented since a reactive power/voltage droop characteristic is selected to investigate the reactive power flow among distributed generators. Proportional reactive power sharing cannot be achieved when these two terms are present.
- Over/under excitation & Volts per Hertz limiters are not implemented, since they are activated only under steady state operation which exceeds the time focus of this work.

Both exciter and prime mover of the generator are not modeled deeper than a low pass filter with an appropriate time constant. The focus of the investigations in this work are directed to the grid coupling between different distributed generators. Thus, a detailed modeling approach of a diesel turbine or the excitation circuit would not provide a better insight of the machine transient response.
Droop characteristics are implemented for both control loops, as theoretically analyzed in chapter 2. More specifically for the speed governor, the droop characteristic is implemented as a setpoint for the mechanical torque in pu, T_m^* which is identical to the setpoint for active power, as both of them are in pu as explained in [10] & [31].
The output voltage reference, V_g^* as well as the angular velocity reference ω_m^* are selected equal to 1 pu.

[2]For each control structure shown in this work, for each sum of signals the plus sign is considered as standard input sign and not depicted in the control diagram.

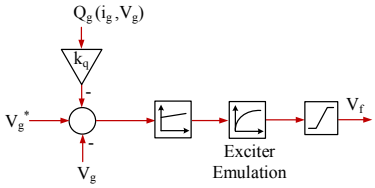

Fig. 3.7: AVR

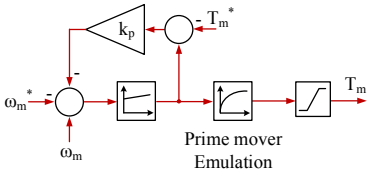

Fig. 3.8: Speed governor

AVR design The controller parameters of the AVR are calculated based on pole placement. Similar to [34] and [35], the machine/exciter system can be represented by first order models. The control plant and the PID controller can be emulated with the following transfer functions:

$$G_{AVR}(s) = \frac{1}{(1+sT_{g,oc})(1+sT_e)} \quad , \quad G_C(s) = \frac{k_d s^2 + k_p s + k_i}{s} \tag{3.6}$$

where: $T_{g,oc}$ is the generator open circuit time constant, T_e the exciter open circuit time constant and k_d, k_p, k_i the derivative, proportional and integral gains of the controller. Regarding pole placement, a certain amount of trial and error can be involved during design validation, since the direct placement of the closed loop poles gives rise to zeros of the transfer function that might affect the transient response of the system. The characteristic equation of the closed loop system is expressed as:

$$G_{AVR}(s)G_C(s) = -1 \tag{3.7}$$

Although it's a third order system, by placing the third pole on the far left real axis the system response can be approximated with a second order system's response. In this way, choosing a minimum response overshoot and setting the settling time equal with the open circuit time constant of the machine, the controller gains are obtained.

Speed governor design Similar to AVR, a PID controller is also realized for the speed governor [36]. Direct pole placement for the controller gains is once more selected as the most appropriate tuning method. Emulating the machine/diesel turbine system with the following transfer function:

$$G_{SG}(s) = \frac{1}{(1+sT_{g,m})(1+sT_t)} \tag{3.8}$$

where $T_{g,m}$ is the starting time of the machine which is based on the moment of inertia J:

$$T_{g,m} = 2H = 2(\frac{1}{2}J(\frac{\omega}{p})^2\frac{1}{S_{base}}) \tag{3.9}$$

with H being the inertia constant of the machine which can be physically interpreted by:

$$H = \frac{stored\ energy\ at\ rated\ speed\ in\ MWs}{MVA\ rating} \tag{3.10}$$

and T_t the diesel turbine time constant. The characteristic equation of the closed loop system is once more obtained, and the gains of the PID controller are once more calculated based on pole placement.

Validation of controllers The controllers designed in the previous paragraphs are verified in operation with a medium voltage salient pole machine [37]. A detailed list of the synchronous generators parameters are given in Table A.3 & A.4 and the corresponding controller parameters in Table A.5. The Bode plots of the open loop transfer function of the control plant with the PID controller are drawn, to evaluate the frequency response of the selected controller gains.

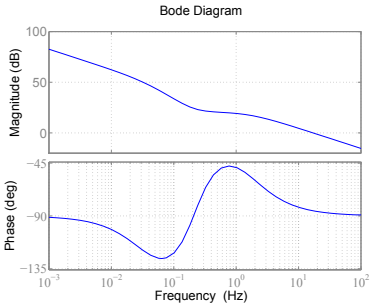

Fig. 3.9: Bode plot of AVR controller

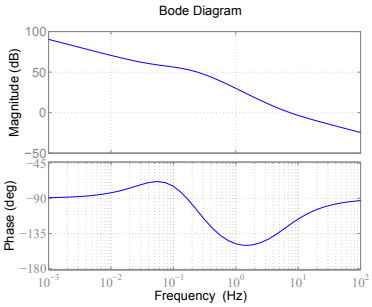

Fig. 3.10: Bode plot of SpG controller

The Bode plots in Fig. 3.9 & 3.10 can aid to the direct calculation of the phase margin of the control loop. The crossing point of the magnitude bode plot with the 0dB axis (@ 20 for the AVR and @ 8Hz for the SpG) is required for the phase margin calculation. Noting at this crossing point the difference between the phase bode plot and the 180° phase limit delivers the controller margin. An adequate phase margin of 90° and 50° for the AVR and the speed governor respectively delivers a transient stable response of the control plant in both cases (phase margin > 30° [38], [39]).

The root locus of the system is also plotted to further examine the stability of the system. The far left placed pole can be observed from Fig. 3.11 & 3.12. It is also shown that all poles and the root locus curves connecting poles and zeros remain in the left plane. At this point it should be noted that both controllers are working in parallel and in the controller design explained in this section their

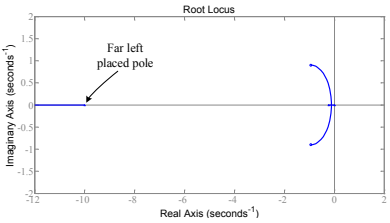

Fig. 3.11: Root locus of AVR controller

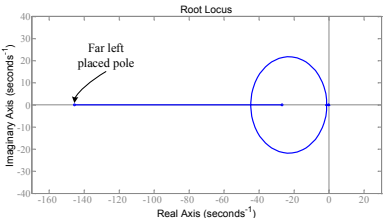

Fig. 3.12: Root locus of SpG controller

interconnection is not considered. That could lead to small deviations, as far as the transient response of the generator is concerned, in the selected overshoots and settling time of the closed control loops of the machine.

3.2 Grid inverter

A generic model of an inverter connected to the rest of the microgrid through a LC(L) filter at its output is the next component to be modeled. This converter is the interfacing element of any inverter-based distributed generator with the grid and is in detail analyzed. Since grid studies is the focus of this work, the control algorithm governing the inverter is the model core and losses calculation or the analysis of the switching process of the semiconductors are neglected. Transformation methods for three-phase systems are implemented, derived from the equivalent ones for modeling synchronous machines [40]. The synchronous rotating reference frame (SRRF), also called the $dq0$ coordinates system, is selected as appropriate control base for our algorithms as an industry standard method. Alternatives can be found, such as the $\alpha\beta\gamma$ stationary reference frame or the *abc* natural reference frame. The natural reference frame could be a meaningful alternative if unsymmetrical faults are considered [41]. In that case, an alternative would be the implementation of separate controllers in the synchronous rotating or stationary reference frame, for controlling the symmetrical components of voltage and currents [42]. A control concept in synchronous rotating frame in combination with symmetrical components analysis has been successfully implemented for the case of two parallel inverters in unsymmetrical loading conditions in [13]. The following figure presents a vectorial representation of the abc to dq transformation, where X could be any three phase system, such as voltage, current, flux linkages, etc. The X_γ, X_0 components of the transformations calculated in Eq. 3.11 & 3.12 are identical and only relevant for non- symmetrical systems and are not further mentioned in this work. In Fig. 3.13 and Eq. 3.11 & 3.12 ω is the rotating angular velocity of the coordinates system, θ_0 is the angle between D- and a-axis of the system, and $\theta = \omega t + \theta_0$ the full angle of the new DQ rotating reference frame. These transformations

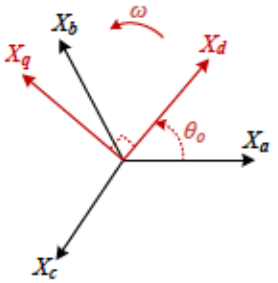

Fig. 3.13: abc & dq vectors

$$\begin{bmatrix} X_\alpha \\ X_\beta \\ X_\gamma \end{bmatrix} = \begin{bmatrix} \frac{2}{3} & -\frac{1}{3} & -\frac{1}{3} \\ 0 & \frac{1}{\sqrt{3}} & -\frac{1}{\sqrt{3}} \\ \frac{1}{3} & \frac{1}{3} & \frac{1}{3} \end{bmatrix} \begin{bmatrix} X_a \\ X_b \\ X_c \end{bmatrix} \tag{3.11}$$

$$\begin{bmatrix} X_d \\ X_q \\ X_0 \end{bmatrix} = \begin{bmatrix} \cos(\theta) & \sin(\theta) & 0 \\ -\sin(\theta) & \cos(\theta) & 0 \\ 0 & 0 & 1 \end{bmatrix} \begin{bmatrix} X_\alpha \\ X_\beta \\ X_\gamma \end{bmatrix} \tag{3.12}$$

can be quite useful for control algorithms, where signals can be easily controlled in other reference frames than the natural reference frame. To elaborate this convenience a three-phase symmetrical voltage system is shown in all three coordination systems below. As seen in Fig. 3.14c, the d- and q- component of the sinusoidal voltage are DC quantities in steady state, since they are rotating with the angular frequency of the system ω, and PI controllers can be employed to govern them.

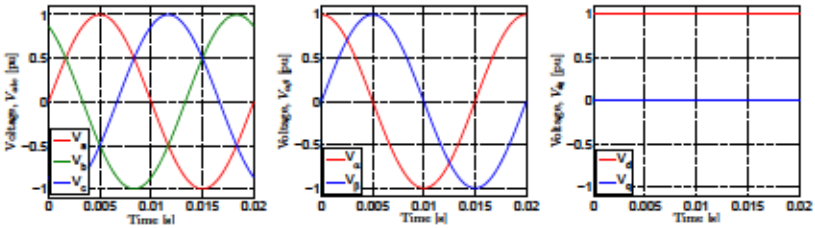

(a) in abc (b) in $\alpha\beta$ (c) in dq

Fig. 3.14: Transformation of a three-phase voltage

Inverter topology The topologies selected for the grid inverter are shown in Fig. 3.15. The left one, in Fig. 3.15a is the standard 2-level topology with a capacitor fed DC-link as input. The right one, in Fig. 3.15b, is the 3-level Neutral Point Clamped (NPC) topology with a capacitor fed DC-link as input. In Fig. 3.15 the inverter is portrayed with IGBT-diode semiconductors, as most appropriate candidates for low/medium voltage and high power applications. Pulse Width Modulation (PWM) is implemented as a standard modulation technique for grid inverters.

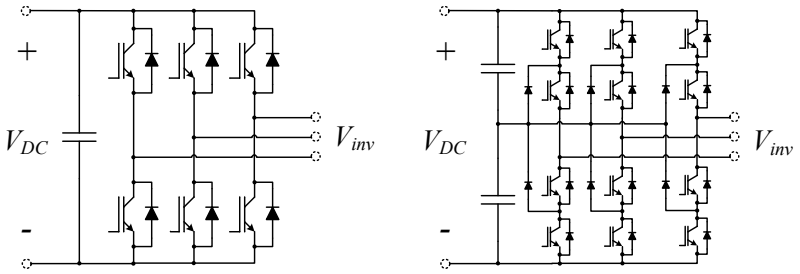

(a) 2-level (b) NPC

Fig. 3.15: Grid inverter topologies

The main difference between topologies is the output voltage, as shown in Fig. 3.16. The phase to DC-link middle point voltage at the output of the inverter together with the sinusoidal reference voltage are depicted.

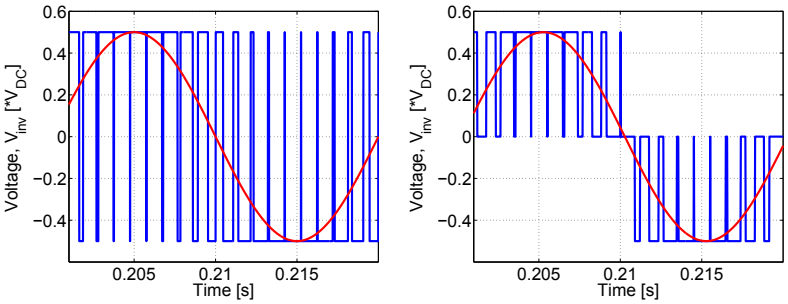

(a) 2-level (b) NPC

Fig. 3.16: Output phase voltage

The inherent advantage of the NPC topology is that, as a three-level topology, the output phase voltage depending on the switching pattern can get three different values ($+\frac{V_{DC}}{2}$, 0, $-\frac{V_{DC}}{2}$), whereas at the 2-level inverter only two ($+\frac{V_{DC}}{2}$, $-\frac{V_{DC}}{2}$). By having more voltage levels the form of a sinusoidal signal is approached, minimizing the need for an output filter. These two topologies are selected to demonstrate the independence of the topology for the control algorithms and grid studies performed in this work. Furthermore, the topology selection is additionally based on the voltage and power level of the inverter-interfaced distributed generator.

Mathematical model of inverter with LCL filter The mathematical model of a single-phase inverter connected through a LCL filter is depicted in Fig. 3.17. The resistors present in Fig. 3.17 are the equivalent series resistances (ESR) of the filter inductors and are in the order of 0.005 pu, which is quite reasonable for medium voltage, high power inductors [43]. The equations of the system are formed, where:

V_i	:	inverter output voltage	C_f	:	filter capacitor
V_g	:	grid voltage	V_C	:	filter capacitor voltage
L_1, R_1	:	converter side L & R	L_2, R_2	:	grid side L & R

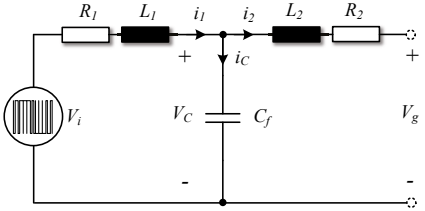

Fig. 3.17: Inverter model with LCL filter

$$\frac{d\bar{i_1}}{dt} = -\frac{R_1}{L_1}\bar{i_1} - \frac{\bar{V_c}}{L_1} + \frac{\bar{V_i}}{L_1} \tag{3.13}$$

$$\frac{d\bar{V_c}}{dt} = -\frac{1}{C_f}(\bar{i_1} - \bar{i_2}) \tag{3.14}$$

$$\frac{d\bar{i_2}}{dt} = -\frac{R_2}{L_2}\bar{i_2} + \frac{\bar{V_c}}{L_2} - \frac{\bar{V_g}}{L_2} \tag{3.15}$$

To describe the inverter output voltage, switching functions are introduced [44], defined in the following equations with the variable p. In the case of a 2-level converter, which is shown in Fig. 3.15a, the switching function for a single leg of the inverter is equal to 1 when the upper switch is closed and 0 when the lower switch is closed. Similar to equations 3.11 & 3.12, equation 3.16 shows their transformation to the synchronous rotating reference frame.

$$\left[\bar{p}_{dq}\right] = \begin{bmatrix} \cos(\theta) & \cos(\theta - \frac{2\pi}{3}) & \cos(\theta + \frac{2\pi}{3}) \\ \sin(\theta) & \sin(\theta - \frac{2\pi}{3}) & \sin(\theta + \frac{2\pi}{3}) \end{bmatrix} \begin{bmatrix} p_a \\ p_b \\ p_c \end{bmatrix} \tag{3.16}$$

With the use of switching functions, the voltage at the output of the converter can be calculated from the available DC-link voltage:

$$\bar{V}_{inv}(t) = \bar{p}_{dq}\,\frac{V_{DC}(t)}{2} \tag{3.17}$$

We conclude to the following state space equations of the mathematical model of the inverter by combining equations (3.13) – (3.17) and transforming them to

the dq coordinates:

$$\frac{d}{dt}\begin{bmatrix} V_{cd} \\ V_{cq} \\ i_{1d} \\ i_{1q} \\ i_{2d} \\ i_{2q} \end{bmatrix} = \begin{bmatrix} 0 & \omega & \frac{1}{C_f} & 0 & -\frac{1}{C_f} & 0 \\ -\omega & 0 & 0 & \frac{1}{C_f} & 0 & -\frac{1}{C_f} \\ -\frac{1}{L1} & 0 & -\frac{R_1}{L_1} & \omega & 0 & 0 \\ 0 & -\frac{1}{L1} & -\omega & -\frac{R_1}{L_1} & 0 & 0 \\ \frac{1}{L_2} & 0 & 0 & 0 & -\frac{R_2}{L_2} & \omega \\ 0 & \frac{1}{L_2} & 0 & 0 & -\omega & -\frac{R_2}{L_2} \end{bmatrix} \begin{bmatrix} V_{cd} \\ V_{cq} \\ i_{1d} \\ i_{1q} \\ i_{2d} \\ i_{2q} \end{bmatrix} + \begin{bmatrix} 0 & 0 \\ 0 & 0 \\ 0 & 0 \\ 0 & 0 \\ -\frac{1}{L_2} & 0 \\ 0 & -\frac{1}{L_2} \end{bmatrix} \begin{bmatrix} V_{gd} \\ V_{gq} \end{bmatrix} + \begin{bmatrix} 0 & 0 \\ 0 & 0 \\ \frac{V_{DC}}{L_1} & 0 \\ 0 & \frac{V_{DC}}{L_1} \\ 0 & 0 \\ 0 & 0 \end{bmatrix} \begin{bmatrix} p_d \\ p_q \end{bmatrix} \quad (3.18)$$

The impact of the dq transformation is seen in Eq. 3.18 with the coupling terms between the d and q components of voltage and current. In case a transformer connects the inverter to the grid, its leakage inductance can be added to L_2. The damping resistor in series with the filter capacitor is neglected for the formulation of the above equations.

DC-link capacitance sizing The selection of the DC-link capacitance is based on the maximum permissible voltage ripple. Assuming linear increase of the variation of the output power ΔP_{max} during one switching period T_s [45] & [46], the maximum energy ΔW to be transferred through the DC-link during one switching period can be calculated:

$$\Delta W \approx \frac{\Delta P_{max} T_s}{2} \quad (3.19)$$

This energy deviation can be however also calculated from the energy that can be stored in the capacitor:

$$\Delta W \approx C_{DC} V_{DC} \Delta V_{DC} \quad (3.20)$$

where V_{DC} and ΔV_{DC} are the DC-link voltage and voltage ripple respectively. Taken into consideration that the maximum power in case of distributed generators is the rated power, namely $\Delta P_{max} = P_n$, Eq. 3.19 & 3.20 can be combined into:

$$C_{DC} = \frac{P_n T_s}{2 V_{DC} \Delta V_{DC}} \quad (3.21)$$

It is however acknowledged that Eq. 3.21 results in significantly lower capacitance values from those realistically selected [45] & [46]. This calculation scheme does not take into consideration the DC-link voltage control dynamics, which have a significant impact on the stability of the DC-link. To obtain a reasonably stable response even in the case of grid faults, it is common to oversize the capacitance derived from this calculation. In [45], a multiple of the switching period is used for this calculation to improve the selection. In this work the permissible allowed DC-link voltage ripple is selected quite low $\Delta V_{DC} = 1 - 2\,\%$, since a stable response of the inverter during grid faults is also a focus. Further investigations on the proper selection of the capacitance should include calcu-

lation of the capacitor current and choosing appropriate capacitors to ensure that enough power cycles are guaranteed. Since system cost reduction is not the priority of this work, but the investigations in system level with realistic components, the selection of DC-link capacitance is not further investigated.

LC(L) Filter Design For the development of operational strategies for grid inverters in the next chapters, different control objectives, voltage and power levels are involved. Therefore, a generic algorithm is developed for the design of the inverter grid filter that can be easily scaled based on the inverter's different attributes. The algorithm has four main steps:

- Calculate the required inverter-side filter inductor based on a pre-defined maximum allowable current ripple
- If it is the case of a LCL filter, the grid-side inductor is designed as a fraction of the inverter-side inductor.
- The capacitance is selected through the choice of the filter's resonance frequency.
- A passive damping resistor is selected based on a desired damping factor.

The design process followed in this work starts from the calculation of the current ripple at the output of the inverter. The inductor equivalent series resistance is for this calculation neglected and the grid voltage, or in our case, the voltage across the capacitor is considered constant through a switching event. For this calculation, the capacitor's influence to the ripple current is considered minimal, since it is also designed to dampen the higher order harmonics, and the inverter-side inductor filters the biggest harmonic proportion of the current. The derivation of the current ripple calculation is performed according to [47]. The worst case current ripple is obtained during the zero crossing of the phase voltage, see Fig. 3.18.

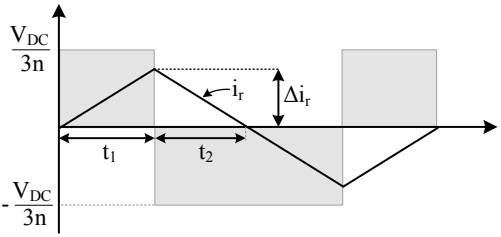

Fig. 3.18: Current ripple by phase voltage zero crossing

Both curves are drawn based on the assumption that the grid voltage is constant during one switching period and the phase voltage drops across the inverter-side filter inductance. From this figure the following equation can be obtained:

$$\Delta i_r = \frac{V_{DC} t_1}{3 n L_f} \ , \quad where \quad t_1 = t_2 = \frac{\sqrt{3} m_{max}}{8 f_s} \tag{3.22}$$

In Eq. 3.22, $m_{max} = 1.15$ is the maximum modulation factor for the case of space vector PWM, or PWM with third harmonic injection, and $n = 1$ *or* 2 in the case of 2-level or 3-level inverters respectively. From Eq. 3.22, by setting a maximum permissible current ripple, $\Delta i_r = 15...25$ % of the nominal current, the required minimum inverter-side filter inductance can be chosen [43]. The second step of the design process is to select the filter resonance frequency (f_f). A guidance rule is given in Eq. 3.23. An alternative would be to design the capacitor based on its reactive power requirements, as a proportion of the rated power of the inverter [48].

$$10 \cdot f_g < f_f < \frac{f_s}{10} \tag{3.23}$$

where f_g is the grid nominal frequency (in our case, 50 Hz) and f_s the selected switching frequency for the semiconductors. This equation can be however successfully followed only in low voltage applications, where the switching frequency lies in the area of $f_s > 5kHz$. In medium voltage applications compromises should be found, where the switching frequency can obtain values lower than $1kHz$. In this case the resonance frequency can reach values down to $f_f = 250Hz$ [43]. Since different factors are involved in this selection, designing an LC(L) filter should be performed in an iterative manner, taking into consideration grid code requirements for the output current [49] or voltage [50] harmonics. In this work, the optimization of the LCL filter is not the investigation focus. The priority is set to realistically model inverter-based medium voltage systems. The filter resonance frequency is set in the range of $f_s = 450...550Hz$, depending on the switching frequency of the inverter. After selecting the desired resonance frequency, the filter capacitance value can be calculated from Eq. 3.24.

$$\omega_f = \frac{1}{\sqrt{L_f C_f}} \quad \Rightarrow \quad C_f = \frac{1}{\omega_f^2 L_f} \tag{3.24}$$

where L_f could be, in the case of a LC filter a single inductor, or in the case of a LCL filter the parallel connection of both inductors, $L_f = \frac{L_1 L_2}{L_1 + L_2}$, as depicted in Fig. 3.17. The selection of the grid-side inductor in the case of a LCL filter is performed typically as a fraction of the inverter-side inductor. The grid-side inductor L_2 is normally smaller than the inverter-side inductor L_1, since it does not have to dampen the whole harmonic current spectrum directly at the inverter output and is considered a less cost-driving component than the inverter-side filter inductor. Typical values for L_2 are in the area of $L_2 = 0.1...0.25 L_1$ [43].
The last filter component is required to dampen unstable transient dynamics

triggered by disturbances or sudden variation of the inverter operating point. The proper damping of these dynamics is achieved through the insertion of passive elements to the filter structure. Although active damping methods can be found in the literature [51], the method of passive damping is further followed in this work. In this method, a resistor is placed in series with the shunt capacitor. To select the value of the passive damping resistor, the damping factor ζ_p should be introduced. Integrating the resistor, R_d in the circuit of Fig. 3.17, the dynamics of the filter should be analyzed [43]. The inverter's forward self-admittance, $Y_1(s) = \frac{I_1(s)}{V_i(s)}$ and the forward trans-admittance $Y_2 = \frac{I_2(s)}{V_i(s)}$ are therefore formulated:

$$Y_1(s) = \frac{1}{L_1} \frac{s^2 + \frac{R_d}{L_2}s + \frac{1}{L_2 C_f}}{s(s^2 + 2\zeta_p \omega_f s + \omega_f^2)} \quad , \quad Y_2(s) = \frac{R_d}{L_1 L_2} \frac{s + \frac{R_d}{C_f}s}{s(s^2 + 2\zeta_p \omega_f s + \omega_f^2)} \tag{3.25}$$

where ω_f is the filter resonance angular frequency and $\zeta_p = \frac{R_d}{2}\sqrt{\frac{C_f}{L_f}}$ the dominant damping factor. These two factors define the dynamic response of the system, as shown from the denominators of Eq. 3.25. Once the reactive components of the filter are selected, the damping resistor can be directly calculated from the desired damping factor. A variation of the damping factor in the range of $\zeta_p = 0.21...0.37$ was performed in [43]. The value of $\zeta_p = 0.3$ delivered an acceptable compromise between damping and attenuation, and is further selected in this work.

As far as the filter type is concerned, the control objective of the inverter could have been a selection criterion. It has been demonstrated in chapter 2 that droop control for grid forming units is based on inductive distribution lines. That has been verified with the calculation of the stability margins of the eigenvalues of a two-generators system. These margins increase with increased impedance path between them, as shown in Fig. 2.10 & 2.11. Therefore, it would be reasonable to select for grid forming inverters a filter type that increases the output grid impedance, e.g. an LCL filter. However, that would not be a realistic approach. Grid forming units connect storage elements to the grid which should be typically able to work in both grid forming and feeding mode. Therefore, the inverter filter should be independent of the control mode of the inverter. In this work, to validate that the control strategies proposed are fully operational independent of the filter type, a differentiation on the filter selection is performed depending on the inverter voltage. For inverters that are connected at $1kV$ a LCL filter is chosen, whereas for inverters connected at $3.3kV$ a LC filter is implemented. At this point it should be mentioned that all inverters are connected to the grid through a step-up transformer, therefore its leakage inductance serves in all cases as an increased output grid impedance. The filter parameters depending on the voltage and power level can be found in Table A.6.

3.2.1 Grid feeding inverter

In modern power systems, all renewable energy based distributed generators that work with the principle of Maximum Power Point Tracking (MPPT) are equipped with a grid feeding inverter. The concept of MPPT is to extract the highest amount of energy from the input source, which could be the case of a solar cell or a wind turbine. The main objective of the grid feeding operational mode is to deliver to the grid the full amount of energy that reaches the DC-link of the inverter. Furthermore, depending on the grid frequency and voltage, grid supporting functions, such as active power / frequency droop and reactive current / voltage droop are also implemented. The explanation of this cascaded control mode starts from the inner fundamental control plant of the inverter and leads to the upper grid-related control functions.

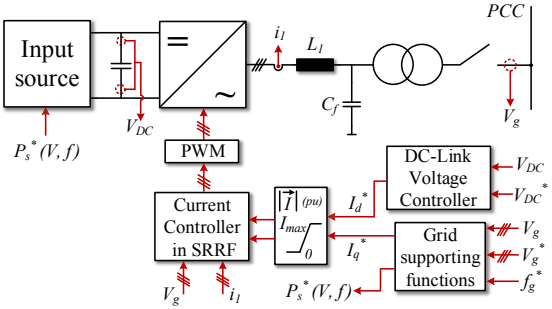

Fig. 3.19: Overall control structure of a grid feeding distributed generator

3.2.1.1 Mathematical model of inverter control plant

For the derivation of the control structure of Fig. 3.19, the mathematical model of the inverter control plant in steady state operating conditions is first obtained. Starting from the inner current controller and assuming that the DC-link voltage is constant, one can obtain the equations of the model with the use of Eq. 3.13, 3.17 and Eq. 3.18:

$$L_1 \frac{di_{1d}}{dt} = L_1 \omega i_{1q} - R_1 i_{1d} + V_{i_d} - V_{Cd} \tag{3.26}$$

$$L_1 \frac{di_{1q}}{dt} = -L_1 \omega i_{1d} - R_1 i_{1q} + V_{i_q} - V_{Cq} \tag{3.27}$$

The voltage across the filter capacitor, V_C, can be accounted as a disturbance for the faster inner current controller and can be fed forward along with the

coupling terms due to the transformation to the synchronous rotating reference frame (SRRF). V_C does not need to be directly measured, but estimated from V_g, i_1 and L_{tr}, the transformer's leakage inductance and calculated in Laplace domain:

$$V_C(s) = \frac{L_{tr} i_1(s) s + V_g(s)}{1 - L_{tr} C_f s^2} \tag{3.28}$$

The equations Eq. 3.26 and Eq. 3.27 can be graphically depicted in the following figure, Fig. 3.20, where $G_c(s) = \frac{k_{p_c} s + k_{i_c}}{s}$ is the PI controller for the d- and q-axis.

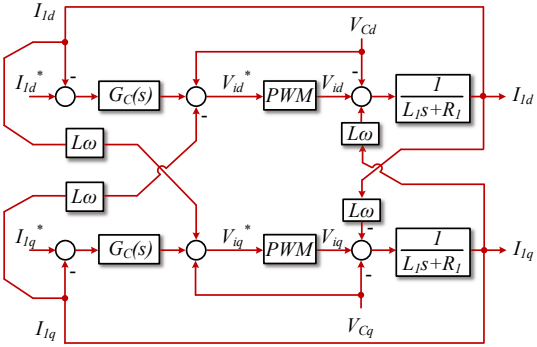

Fig. 3.20: Control block diagram of the grid feeding inverter

The current controller is connected to the control plant though the inverter, as seen in Fig. 3.20. To calculate the transfer function of the system, the coupling and feed-forward terms are neglected, as well as the inverter and transformation calculations, which are considered ideal components. Defining appropriate controller gains, the closed-loop transfer function can be represented by a first order linear system:

$$\frac{I_{dq}(s)}{I^*_{dq}(s)} = \frac{1}{T_i s + 1} \tag{3.29}$$

The appropriate gains for the PI controller are given by:

$$k_{p_c} = \frac{L_1}{T_i} \quad , \quad k_{i_c} = \frac{R_1}{T_i} \tag{3.30}$$

where T_i is the time constant of the closed-loop system, identical for each axis. This time constant is a designer' choice, and it should be quite small for a fast control response, but the bandwidth ($\frac{2\pi}{2T_i}$) should also be at least ten times smaller than the switching frequency of the inverter (expressed in rad/sec) [52],

[53]. This bandwidth requirement ensures that the inverter can be neglected during the formulation of the transfer function of the current controller. Typical values for T_i are in the range of $0.5-5$ ms [54].
Since in this work medium voltage applications are considered and the switching frequency is selected between 2 and 2.5 kHz, see Table A.6, the bandwidth requirement is not met. Therefore, the alternative of the technical optimum (or modulus optimum) criterion is applied [55], [56]. In this case, the control plant of the inductor and resistor in series of the filter is identified with the addition of the delay due to the switching frequency of the inverter. It should be noted that also for the case of technical optimum a dominant pole should be present [56], which in our case is the first order system of the inductor and resistor in series, $T_{RL} = \frac{L_1}{R_1}$ with a gain of $K_{RL} = \frac{1}{R_1}$. The PWM block of figure 3.20 is replaced by $G_{PWM} = \frac{K_{PWM}}{T_s s+1}$, where K_{PWM} is the inverter voltage gain, and T_s the time constant due to the switching frequency and the rest of processing delays, typically selected equal to $T_s = 1.5T_{sf}$, with T_{sf} the time constant of the switching frequency. The transfer function of the closed loop system can then be calculated as follows:

$$G_{cc} = \frac{1}{\frac{T_{RL}T_s}{K_{pc}K_{PWM}K_{RL}}s^2 + \frac{T_{RL}}{K_{pc}K_{PWM}K_{RL}}s + 1} \tag{3.31}$$

Identifying the damping factor D of the second order system and setting it equal to $D = \sqrt{2}/2$ for a critically damped system [55], the current controller can be fully calculated:

$$k_{p_c} = \frac{T_{RL}}{2T_s K_{PWM}K_{RL}} \quad , \quad k_{i_c} = \frac{k_{p_c}}{T_{RL}} \tag{3.32}$$

The initial objective of replacing the closed current control loop with a first order system has been obtained with this method too. Since $T_{RL} >> T_s$, the first order system of the current control loop is obtained by:

$$G_{cc} = \frac{1}{2T_s s+1} \tag{3.33}$$

The DC-link controller is built as an outer loop, resulting in a cascaded control structure, shown in Fig. 3.21. Starting from the energy stored in the DC-link capacitor C_{DC}:

$$E_c = \frac{1}{2}C_{DC}V_{DC}^2 \tag{3.34}$$

The time derivative of this energy should lead to the power balance equation of the DC-link. Defining the power coming from the input source P_{in}, and the

power delivered to the grid as P_{out}:

$$\frac{1}{2}C_{DC}\frac{d}{dt}V_{DC}^2 = P_{in} - P_{out} \tag{3.35}$$

Similar to the current control loop, a linear system is the objective of the DC-link controller. Therefore, the DC-link voltage V_{DC} is substituted with a control variable u. For the practical implementation of this controller, the reference and measured voltage will be squared and then substracted to obtain the input error of the PI controller, $\epsilon(t)$. Neglecting the filter resistor R_1 as it is responsible for less than 1% of the transferred power, the instantaneous power delivered to the grid calculated in dq coordinates is $P_{out} = \frac{3}{2}V_{C_d}I_d + V_{C_q}\overset{0}{I_q}$, while the power input source is considered a disturbance, $\delta(t)$ [52]. The q-component of the voltage V_{C_q} is zero since the selected axis for the dq transformation is aligned with the axis of phase a, and V_{C_d} is therefore equal to the voltage amplitude, $\hat{V}_C$:

$$\frac{1}{2}C_{DC}\frac{d}{dt}u = \delta(t) - \frac{3}{2}\hat{V}_C I_d \tag{3.36}$$

The transfer function of the system is derived, taking also into consideration the D-axis current reference I_d^* as control variable, and the transfer function of the underlaying current controller:

$$G_{DC}(s) = \frac{u(s)}{I_d(s)} = -\frac{3\hat{V}_C}{C_{DC}}\frac{1}{s}\frac{1}{2T_s s + 1} \tag{3.37}$$

The transfer function has one pole in the origin, and symmetrical optimum criteria can be applied to design the PI controllers. Defining once more a PI controller with a transfer function of:

$$G_{PI_{DC}}(s) = k_{p_v}(1 + \frac{1}{T_v s}) \tag{3.38}$$

The symmetrical optimum criterion is based on designing the amplitude and phase plot of the open loop transfer function being symmetrical about the crossover frequency [56], [57]& [58]. The gain of the controllers are then given by [55]:

$$k_{p_v} = \frac{C_{DC}}{4\alpha T_s} \quad , \quad T_v = 4T_s \tag{3.39}$$

where $\alpha = 2.4$ is selected to result in a critically damped second order system, and the time constant of the voltage controller is increased because of the sampling delay of the measured DC-link voltage. It can be observed that the amplitude of the output voltage is eliminated from Eq. 3.39, since the controller is designed in pu. Several alternatives can be found for designing the PI controller of the DC-link voltage, including the principle of the Internal Model Control (IMC) [52]. The IMC method has the objective of subtracting the control plant

from the closed loop transfer function and selecting then an appropriate controller bandwidth based on the application.
The overall control structure of the controller is given in Fig. 3.21.

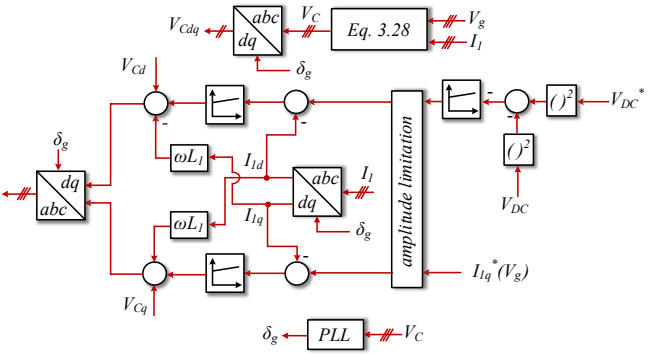

Fig. 3.21: Cascaded control structure of grid feeding inverter

The phase locked loop (PLL) which is needed to acquire the grid voltage angle, δ_g is based on input/output power balance equations, or phase balance method as described in [59]. An alternative would be the standard DQ- control structure, where the Q-component of the voltage is controlled to zero to produce the system frequency [60]. More on the implementation of the PLL can be found in Appendix A.

3.2.1.2 Dynamic grid supporting functions

There are several codes and norms that have been issued for grid feeding inverters connected to stiff grids for the provision of grid support during transients [61], [62]. In a microgrid, which is classified as a weak grid prone to stability disturbances, the grid supporting functions are of fundamental importance for stable operation. In Fig. 3.22 & 3.23, typical droop curves for supporting grid voltage and frequency are depicted. The limits for the reactive current (or power) injection are taken from [61] and for active power/frequency dependence from [62]. These functions are formed by taking into consideration the inductive character of a stiff grid.

The grid supporting functions influence the operation of the grid feeding inverter and the controller of the input power source. The grid feeding inverter is responsible for the power balance of the DC-link and can also control separately the reactive current reference, depending on the grid voltage. It is however not responsible for the input power to the DC-link. Therefore, if over/under-frequency occurs, the controller of the input power source should intervene to prohibit rise

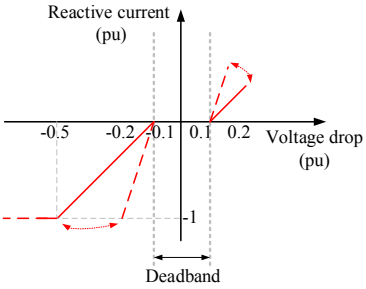

Fig. 3.22: Reactive current/voltage

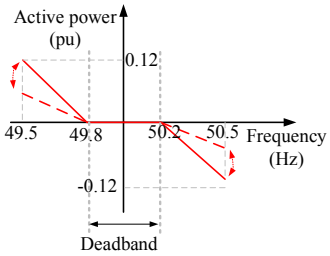

Fig. 3.23: Active power/frequency

of the DC-link voltage. It should be also explained why in the case of voltage deviations the grid feeding inverter obtains a direct current reference, whereas in the case of frequency deviations the inverter obtains a power reference. Power is directly coupled with voltage, therefore in the case of voltage deviations applying a power reference would not meaningful, since the voltage varies. Frequency deviations are not however coupled with power amplitude, therefore it is reasonable to give to the inverter a power reference in that case. In Fig. 3.22, the so-called *'k-factor'* can be identified as the proportionality factor between reactive current reference and voltage drop, which is in this case equal to 2. In [63] the impact of different values of this k-factor on the stability of a relatively stiff grid is investigated. Further discussions on reactive current injection are given in chapter 6, where the dynamic response in fault case is analyzed, and the curve of Fig. 3.22 is optimized for medium voltage microgrids.

3.2.1.3 Static grid supporting functions

The supporting functions explained in the previous section refer to abnormal states, where the grid voltage or frequency experience deviations from their nominal values. Further requirements however exist, which demand power setpoints from renewable energy based generators during normal operation. These are called static grid supporting functions, with the most typical one being controlling the power factor at the PCC of the grid feeding inverter. The grid operator can define a reference point for the reactive power, Q_g^* or directly for the power factor, e.g. $\cos\phi = 0.95$. In this case, the control structure of Fig. 3.19 should be modified with an additional PI controller for the calculation of the new reactive current reference, I_q^*. In Fig. 3.24 the Q_g^* variant is depicted.

The PI controller dynamics should be carefully designed, so that unwanted transient effects can be avoided. These dynamics should be at least 10 times slower

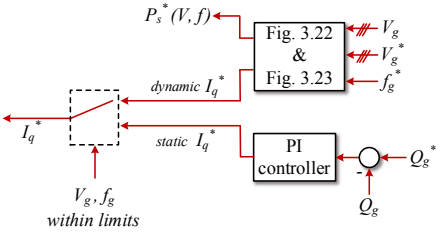

Fig. 3.24: Static support of grid feeding inverter

than the dynamics of the DC-link PI controller to avoid operational states where the two outer PI controllers are working against each other. The active and reactive power the generator feeds to the grid P_g & Q_g, can be calculated from the grid voltage, V_g and the output current.

3.2.1.4 Grid feeding inverter controller verification

Although the focus of this work is in system level, the dynamics of each component were also tested in standalone mode to verify the selected design process. In this paragraph the dynamics of the grid feeding inverter are validated through a step response applied to its closed control loop.

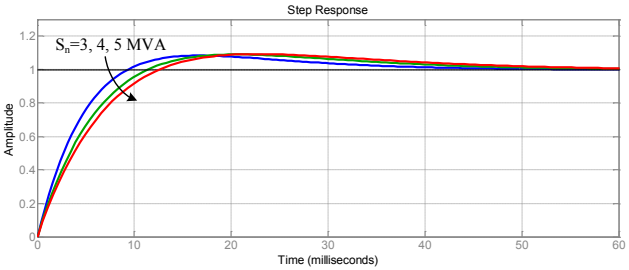

Fig. 3.25: Grid feeding inverter controller verification

The outer control reference to which the step input is applied is the DC-link voltage controller. The grid impedance or grid voltage dynamics are neglected for this theoretical investigation. The closed control loop consists of the cascaded DC-link voltage controller and inner current controller with their control plants accordingly. It is demonstrated in Fig. 3.25 that the cascaded control delivers a robust performance towards the step disturbance. The selected rated

powers of $S_n = 3,\ 4,\ 5\ MVA$ correspond to grid feeding inverter models used in the investigations of the following chapters. The inverter, filter and controller parameters can be found in Table A.6. Analyzing Fig. 3.25, an overshoot of almost 10% is observed, which can be explained through the DC-link controller design. The DC-link voltage is an essential stability element for the grid feeding inverter. The DC-link controller time constant derived from symmetrical optimum criteria was reduced to allow this overshoot. It is selected in this way to enable fast tracking of the voltage reference upon load changes or faults.

3.2.1.5 Grid feeding inverter in PQ control

In case the input source of the distributed generator is able to control the DC-link voltage, a variation of the grid feeding control can be applied, in this work named PQ control. The outer DC-link voltage control is replaced by the direct calculation of the d- and q-axis component of the current reference:

$$\begin{aligned} P_{set} &= \frac{3}{2} V_{C_d} I_d^* + V_{C_q}^{0} I_q \\ Q_{set} &= -\frac{3}{2} V_{C_d} I_q^* + V_{C_q}^{0} I_d \end{aligned} \tag{3.40}$$

As previously explained, the q-component of the voltage is zero due to the axis alliance of the angle produced from the PLL, identical to the axis of phase a. The overall control structure is depicted in Fig. 3.26. The setpoints for active

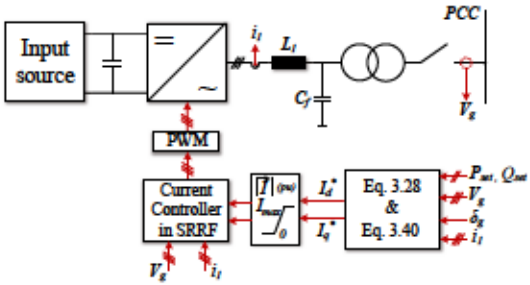

Fig. 3.26: Control structure of grid feeding inverter in PQ control

and reactive power, P_{set} and Q_{set} respectively, can be given from the utility grid operator, or can vary depending on the incoming energy of the input source. Fuel cells, batteries and flywheels would be ideal candidates for this control mode, since they can regulate their output power. This operational mode is quite useful for grid supporting strategies, because of the flexibility it offers depending on grid demands, and not necessarily in the incoming energy as in the case of renewable energy sources.

3.2.2 Grid forming inverter in standalone mode

The topology of the grid forming inverter, depicted in Fig. 3.27, is quite similar to the one of the grid feeding inverter. A LCL filter is selected in this case, together with a step-up transformer for the grid connection. The grid forming inverter requires a DC input source that provides the energy required from the grid. The case when the DC power capacity cannot fulfill the grid demands is not considered in this work. In such a scenario, the grid forming inverter should disconnect from the grid to avoid internal damage of its DC source. If the grid forming inverter is the only grid forming unit in that case, then load shedding should be performed. The input source controls also the DC-link voltage of the system. The objective of the inverter's control algorithm is to regulate the amplitude voltage and frequency at its output and provide the necessary active and reactive power to the rest of the microgrid. A cascaded control structure is here implemented [64].

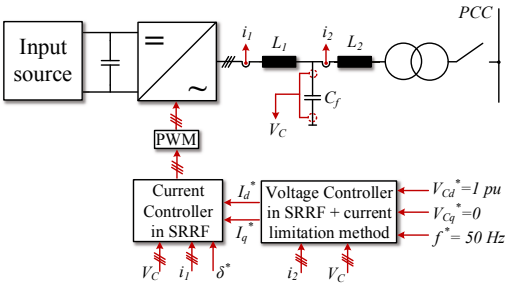

Fig. 3.27: Overall control structure of grid forming standalone inverter

The mathematical model of the inner current controller was in detail explained in section 3.2.1. The control variation is located at the outer voltage control loop. The main objective of this loop is to regulate the voltage at the output of the inverter V_C across the filter capacitor C_f. The dynamics of this control loop are governed by equations 3.14 and in dq frame 3.18, once more documented here:

$$C_f \frac{dV_{C_d}}{dt} = C_f \omega V_{C_q} + i_{1d} - i_{2d} \tag{3.41}$$

$$C_f \frac{dV_{C_q}}{dt} = -C_f \omega V_{C_d} + i_{1q} - i_{2q} \tag{3.42}$$

If the dynamics of the inner current controller are also taken into consideration, Fig. 3.28 is obtained. The control plant of the grid forming inverter is depicted, where $T_i = 2T_s$, as previously explained. From equations 3.41 & 3.27 and Fig. 3.28, the PI controller for the voltage loop can be designed. A direct selection

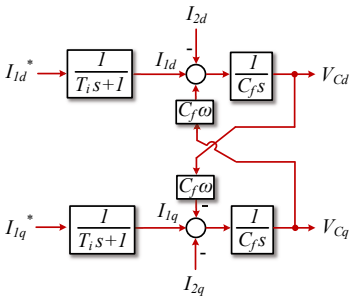

Fig. 3.28: Voltage control plant of the grid feeding inverter

of the phase margin of the open loop is selected as design process [54]. Let

$$G_{PI_V}(s) = k_{p_v}\frac{s+z}{s} \tag{3.43}$$

be the transfer function of the PI controller for the voltage loop. The open loop gain can then be calculated as:

$$l(s) = \frac{k_{p_v}}{2T_s C_f}\left(\frac{s+z}{s+2T_s^{-1}}\right)\frac{1}{s^2} \tag{3.44}$$

Defining the gain crossover frequency $\omega_c = \sqrt{zT_s^{-1}}$, and selecting a phase margin of $\delta_m = \sin^{-1}\left(\frac{1-2T_s z}{1+2T_s z}\right) = 53°$, the PI controller gain can be calculated as $k = C_f\omega_c$. This direct selection of the phase margin equal to 53° is similar to the implementation of the symmetrical optimum criterion [54]. The advantage of this method is that the phase margin can be further tuned, in cases where the symmetrical optimum criterion does not achieve satisfactory results. The proposed cascaded control structure is depicted in Fig. 3.29. Similar to section 3.2.1, decoupling terms for the voltage are present, as well as feed-forward terms of system outputs, here the load current. The feed-forward term of the current can be multiplied with a factor ranging from $F = 0.5...0.8$ to minimize the effect of a severe disturbance in the slower outer voltage loop [64]. Different combinations for the DQ components of the voltage reference $V_{C_{dq}}^*$ exist, the one followed in this work is selecting $V_{C_d}^* = \hat{V}_C = 1$ pu and $V_{C_q}^* = 0$ [54].

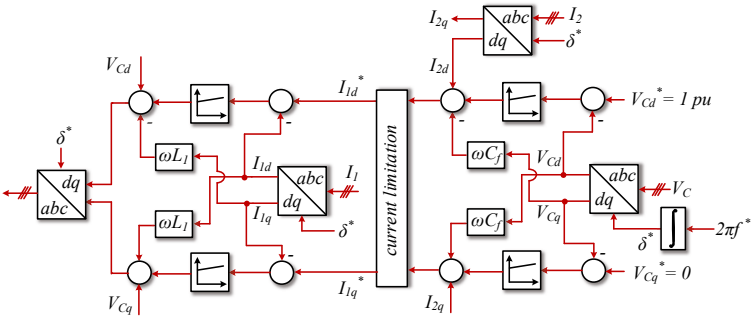

Fig. 3.29: Cascaded control structure of grid forming standalone inverter

3.2.3 Grid forming inverter in parallel mode

In parallel mode of operation more than one grid forming units are working in parallel to share the grid load. In this case, droop control is implemented to achieve proportional power sharing among the distributed generators, as explained in chapter 2. The inner voltage and current controllers in SRRF remain the same as with the standalone mode of operation. The outer references for the

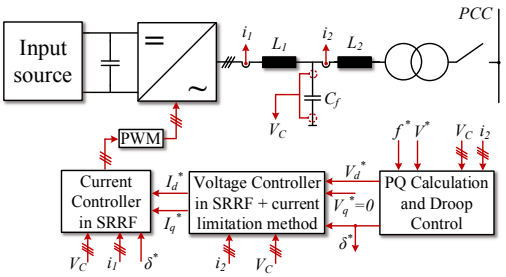

Fig. 3.30: Overall control structure of grid forming inverter in parallel mode

voltage and transformation angle change, as shown in Fig. 3.31. An interesting component of the implementation of droop control is the selection of the cut-off frequency of the low pass filter applied after the calculation of active and reactive power. According to [25] and [29], a designated range for this frequency is $f_{LPF} = 5-10Hz$. In chapter 2 this range is proven to provide stable operation. The allowed region for the droop gains k_p , k_q for medium voltage, high power grid forming units was investigated in chapter 2. The selection of the appropriate droop gains and power setpoints, P_{set}, Q_{set} depends on the configuration of

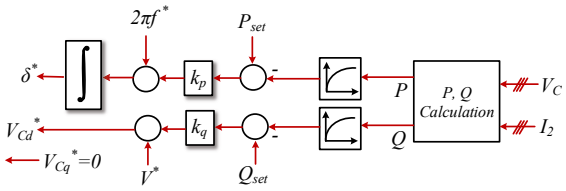

Fig. 3.31: Droop control implementation for grid forming inverter

each microgrid and will be further discussed in chapters 5 & 6.
In parallel operation of a great number of grid forming inverters, system cost reduction is always an issue. To reduce these hardware costs (in expense of increasing programming complexity however), the measurement points can be minimized. Similar to the estimation of the capacitor voltage from the grid voltage and converter current, given in Eq. 3.28, the output current I_2 can be also estimated. The grid voltage V_g and converter current are measured, and according to Fig. 3.17 the following equation is formed:

$$I_2(s) = \frac{I_1(s)}{C_f(L_2+L_{tr})s^2+R_2C_fs+1} - \frac{V_g(s)C_fs}{C_f(L_2+L_{tr})s^2+R_2C_fs+1} \tag{3.45}$$

where R_2 is the resistance of the grid side inductor, as previously explained. The required measurements for the overall control structure are I_2 and V_g, in case the components values are known with adequate precision. Since these kind of estimations are sensitive to noise disturbances and parameters change, it is typical in hardware setups to implement more complex state observers with variable error feedback, such as in [65]. The capacitor's voltage V_C has to be measured for the synchronization of the grid forming inverter in parallel operation.

Grid forming controller validation Similar to the grid feeding inverter, the dynamic of the grid forming inverter is tested through a 1 *pu* step response of its closed control loop. The closed control loop includes the inner current and voltage controller, as well as their control plants, namely the time constants of the LCL filter. For the investigations performed in this work, the power and voltage level of the grid forming inverter vary depending on the test scenario, as depicted in Fig. 3.32. Therefore the performance of the developed controller, in combination with the designed filter parameters is evaluated for a spectrum of the rated power, S_n. The figure depicts the step response of the closed loop system of the control structure of the grid forming inverter in standalone mode. The outer power calculation and droop control loop is neglected, since the dy-

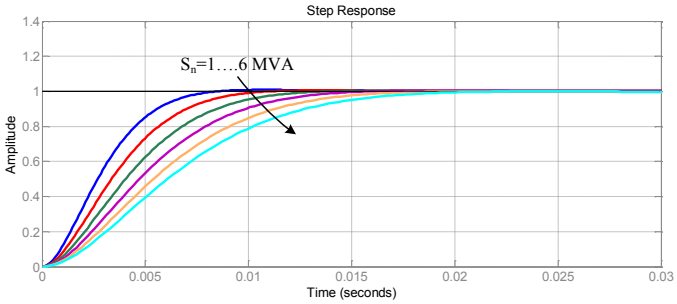

Fig. 3.32: Grid forming inverter controller verification

namics of droop control are of a higher order and do not influence the response of the grid forming inverter. The step response refers to the input reference of the two-loop closed system, which in this case would be the voltage amplitude across the filter capacitor. The dynamics of the control loop do not show any over-transients and the transient response becomes slower by increasing the rated power. It can be observed that the grid forming inverter manages to control its output voltage in all cases in less than two grid periods. The theoretical step response of the ideal closed control loop is not taking into consideration the dynamics of the input power source, the DC-link of the inverter as well as the grid load. The dynamics of the DC-part could introduce a further delay, depending on the ability of the DC power source to provide the necessary power that the grid load demands.

3.2.4 Limiting signals in cascaded control structures

To prevent component malfunction or even destruction, limitation should be employed in strategic positions of the cascaded control structure. This is typically performed by signal saturation, where the variables are limited to a predefined zone. Due to the presence of PI controllers in the cascaded control structures previously explained, an antiwind-up scheme is implemented to prevent the PI controllers integrators to augment the error. Wind up is a well known phenomenon that degrades PI controller's performance, with several schemes already developed to minimize its effects [66].

3.2.4.1 Design of Anti-windup Loop

Anti-windup or back calculation [53] is a common practice in the implementation of PI controllers. Starting from Fig. 3.33, the basic equations that govern the PI controller can be formulated.

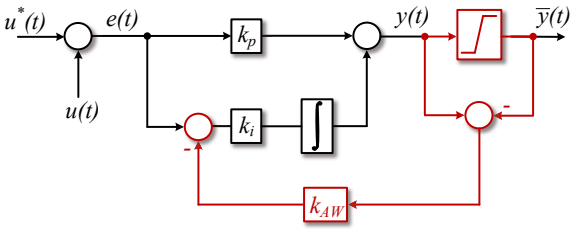

Fig. 3.33: Anti-windup structure

$$y(t) = k_p e(t) + \int k_i e(t) \tag{3.46}$$

defining

$$I(t) = \int e(t) \tag{3.47}$$

and extracting k_i from the integration as a time invariant factor, one obtains:

$$y(t) = k_p e(t) + k_i I(t) \tag{3.48}$$

To avoid integrator windup, the error to be integrated, $e(t)$ should be modified so that the outcome of the integration, $I(t)$, could remain stable once the output $y(t)$ is saturated. Defining the modified error as $\bar{e}(t)$, the saturated output $\bar{y}(t)$ can be calculated then as:

$$\bar{y}(t) = k_p \bar{e}(t) + k_i I(t) \tag{3.49}$$

The modified error that the integrator should receive as input can then be calculated by subtracting Eq. 3.46 from Eq. 3.49:

$$\bar{e}(t) = \frac{1}{k_p}[\bar{y}(t) - y(t) + k_p e(t)] = e(t) + \frac{1}{k_p}[\bar{y}(t) - y(t)] \tag{3.50}$$

The modified error contains the original error and the difference that the integrator produces because of the saturated value. The anti-windup gain can be calculated as in Eq. 3.50 and realized in Fig. 3.33, with $k_{AW} = \frac{1}{k_p}$ [52]. The selected anti-windup gains for each inverter case are given in Table A.6.

3.2.4.2 PWM-voltage limitation

To avoid over-modulation, the voltage references routed to PWM are limited. The limits can be set according to the modulation technique used and the degree of freedom that the grid filter provides. Typical values range from 1 to 1.15 pu, depending on the modulation method used, namely sinusoidal-triangle or space vector/injection of third harmonic modulation . The voltage vector can be limited with a control element shown in Fig. 3.34, which extends the previously shown control structures.

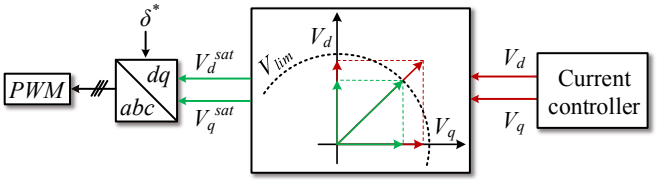

Fig. 3.34: Reference voltage amplitude limitation

3.2.4.3 Current limiting methods

The current limiting element in the inverter's controller structure serves as the main protection mechanism for all power electronic components. There are two main approaches for the implementation of a current limiting method in the cascaded controller structure in SRRF:

- *current reference saturation*: It has been demonstrated in the previous sections that all grid inverters are equipped with an inner current controller. This current limiting method saturates the current reference at the input of this controller. The reference value can be limited either direct at its d- and q-components, or through the amplitude of the current. An alternative for the current amplitude limiting would be to set saturated values for each current component, as soon as the current exceeds a threshold value.
- *transient virtual impedance*: In this approach the controller's reference signals are not saturated. An artificial impedance is built from the measured voltage and current at the output of the inverter, successfully limiting the inverter current as soon as a threshold value is reached.

The different current limiting concepts are further analyzed and compared for the case of grid forming inverters in standalone and parallel operation in chapter 6.

3.3 Battery pack

Batteries play a crucial role in the smooth grid integration of renewable energy since they can transform chemical to electrical energy and consequently store it. This is a significant benefit towards balancing electrical energy production and consumption. In this work, only secondary batteries that can be charged and discharged providing several operational cycles are taken into consideration [67].

3.3.1 Battery cell

The structure of a battery cell is shown in Fig. 3.35 discharging to an ohmic load [68], [69]. Two subcells are the main components, which are inside an electrolyte and isolated through a separator, so that internal short circuit can be avoided. The respective chemical equations are also included in Fig. 3.35. Further explanations to the chemical reactions as well as the proper selection on anode and cathode materials can be found in [68]. The main characteristic

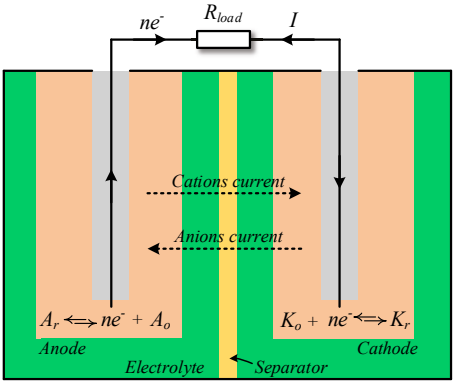

Fig. 3.35: Battery cell structure

of any battery cell is the direct dependence of the voltage at its output, namely the open circuit voltage (V_{OC}) to the state of charge (SoC) of the battery cell. This dependence is documented in the Nernst equation that directly relates the voltage potential of a battery half-cell to the concentration of the reactants used [68]. Since the direct calculation of the open circuit voltage depends on the reaction coefficients, it is common to experimentally obtain its characteristics. Based on these measurements, this relation can be expressed as a curve and varies for each battery type and also for the charging and discharging process.

The focus of our work is not to examine this discharging and charging curve of a specific battery type, but to develop a model that can receive and implement these curves. Since for most battery types the charging and discharging curves possess similar characteristics, in order to decrease the complexity of the model it is decided to simulate the battery model with an universal SoC-output voltage curve. An exemplary curve of a lithium-ion battery [70] is shown in Fig. 3.36, where C_b is the nominal battery capacity. It can be observed that when the SoC drops below 10%, the voltage experiences a significant drop. This voltage drop defines the operational limit of the battery cell, the lowest SoC that can be tolerated during deep discharging.

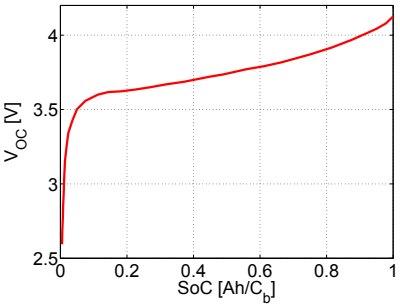

Fig. 3.36: State of charge vs open circuit voltage

3.3.1.1 Dynamic behavior of a battery cell

The dynamic behavior of a battery cell under load is determined mainly through three different mechanisms, named in electrochemistry over-potentials, η.

- First of all, the conductance of the electrolyte as well as of the battery leads and electrodes can be represented as an ohmic element, mostly described as R_e, the inner resistance of the battery cell.
- The transition between the conduction of ions and electrons in the active material, as shown in Fig. 3.35, is not ideal and produces charge transfer losses. These can be represented as a parallel RC element, R_{ct} and C_{dl}. The charge transfer resistance, R_{ct} depends on the geomentry of the battery cell and the current exchange density. The capacitive element appears due to the rise of charge carriers with positive and negative charge at the interface layer of the active material. Due to the double charge characteristic, the capacitive element is called double layer capacitor C_{dl}.
- The last loss mechanism can be found in the Nernst equation, where the galvanic potential is calculated directly from the concentration gradients and the consequent diffusion processes of the ions in the electrolyte [68].

These losses are called diffusion overvoltages and their exact effect on the dynamical behavior can be found through measurement of the dynamic battery impedance. The diffusion losses can be accurately represented through an additional parallel RC element, called Warburg impedance [71].

The battery equivalent circuit with the passive elements that reproduce its electrochemical dynamical model is depicted in Fig. 3.37, where V_{BAT} is the output voltage of the battery cell. The passive components of the battery equivalent

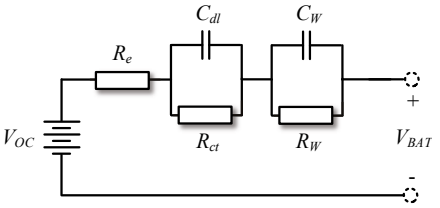

Fig. 3.37: Equivalent circuit of battery cell

circuit are parametrized through the method of electrochemical impedance spectroscopy (EIS). In the method of EIS a small ac current flows through the device under investigation and its voltage response is measured by calculating the device impedance for a wide frequency range. In [71] the impedance of a Li-ion battery cell is measured and used to calculate the passive components of the equivalent circuit. The measurement is performed for $SoC = 50\%$ and surrounding temperature $T = 25°\text{C}$ and is depicted together with the calculated impedance model in Fig. 3.38. The impedance spectroscopy takes place for a frequency rage of 2.1m Hz to 21.7 Hz, with 21.7 Hz being the point where the impedance spectrum cuts the real axis. In the following section the interpretation of the measured impedance is analyzed, which is then deployed for the derivation of the parameters of the equivalent circuit. The four decisive points for the derivation of the parameters are depicted, along with the frequency at which they appear.

- The Warburg impedance as well as the diffusion (charge transfer) losses are negligible for higher frequencies [68]. Therefore, the section point of the impedance with the real axis at $f_1 = 21.7\ Hz$ represents the inner battery resistance $R_e = 50m\Omega$.
- Towards the end of the first semicircle, at $f_3 \approx 21.7mHz$, the charge transfer resistance R_{ct} can be calculated. At that point the only active resistances are R_{ct} and R_e, and their sum, read from Fig. 3.38 is around 130 $m\Omega$. So $R_{ct} \approx 80m\Omega$.
- To calculate the double layer capacitance its impedance, in parallel with

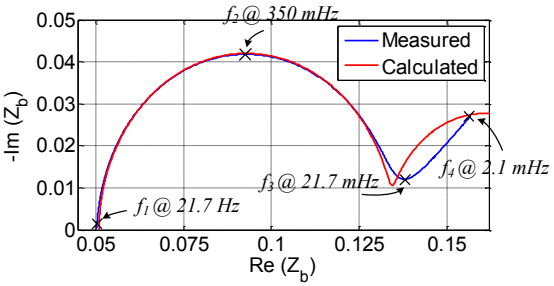

Fig. 3.38: Impedances comparison

the charge transfer resistance, is required:

$$Z_{ct//dl} = \frac{R_{ct}}{1+\omega^2 R_{ct}^2 C_{dl}^2} - j\frac{\omega^2 R_{ct}^2 C_{dl}^2}{1+\omega^2 R_{ct}^2 C_{dl}^2} \tag{3.51}$$

At $f_2 = 350mHz$ the semicircle caused by the parallel impedance of charge transfer resistance and double layer capacitance reaches its maximum, and the real and imaginary parts of the equation 3.51 are equal [68]. Therefore:

$$\frac{1}{R_{ct}C_{dl}} = 2\pi \cdot 350mHz \quad \Rightarrow \quad C_{dl} = 5.7F \tag{3.52}$$

- The Warburg impedance dominates in the lower frequencies region between f_3 and f_4 [71]. The Warbung capacitance C_W is calculated from the lowest frequency point and the Warbung resistance, R_W from curve fitting of the desired impedance to the measured value [69], as seen in Fig. 3.38:

$$C_W = 2.2kF \quad , \quad R_W = 54m\Omega \tag{3.53}$$

The dynamic impedance of a battery cell can lightly variate depending on the state of charge [71]. For dynamic impedance models that are valid for a wider SoC-range the integration of non-linear passive elements has been proposed [72].

3.3.2 Battery pack with DC/DC converter

In the previous section the detailed modelling technique of a battery cell was presented. A single cell however cannot be connected to the rest of the microgrid. Depending on the desired voltage and power level, several battery cell strings should be connected. To reduce model complexity, in our work it is assumed that, when forming a battery pack, the single battery cell model remains and

the voltage is calculated from the current SoC and multiplied with the number of cells in series. In case of more cell strings in parallel, the charge capacity of a single cell is consequently multiplied and added to the model.
An overview of several estimation methods of the battery SoC is given in [68]. A straight-forward method is measuring the output cell current i and integrating it to obtain the battery charge, Q:

$$Q = \int i dt \tag{3.54}$$

and setting an initial SoC value (SoC_0) the instantaneous state of charge can be estimated:

$$SoC(t) = SoC_0 - \frac{\int i dt}{C_b} \tag{3.55}$$

where C_b is the nominal battery capacity, measured in Ah.
A grid inverter is needed to connect the battery pack to any AC microgrid. Connecting directly the battery pack to the DC-link of the inverter could be problematic, since the battery output voltage can experience a severe drop in lower $SoCs$. The DC-link voltage should be over-dimensioned, so that the battery-based distributed generator could stay connected when operating in lower $SoCs$. An alternative would be to connect intermediately a DC/DC converter to boost the voltage to the required level. Despite the fact that the full bridge DC/DC converter could be an attractive solution for this application, since its voltage input limits can reach quite low values [69], the half bridge was selected to realistically minimize switches number and losses. The complete configuration of the DC/DC converter with its control structure and the implementation of the battery cell model is depicted in Fig. 3.39, where n_p is the number of cells connected in series.

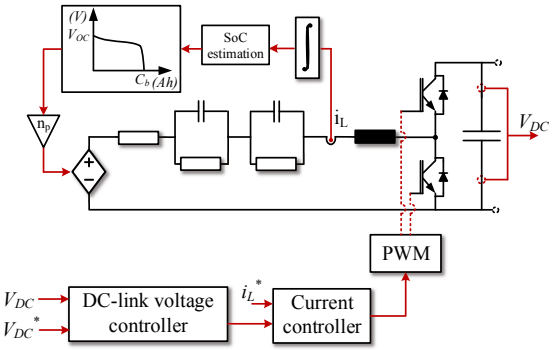

Fig. 3.39: Battery pack model with DC/DC converter

3.3.2.1 DC/DC converter model

The control structure shown in Fig. 3.39 is a cascaded control structure with a faster inner current control loop and an outer voltage control loop. A single voltage control loop is not considered in this work, since it induces an unstable dynamic behavior of the current. In that case, the system is constituted non minimum-phase, as it is shown in [73] for an ideal boost converter. An alternative to this control structure would be to develop two control structures and depending on the operation mode of the half-bridge, as boost or buck converter, to switch between these structures [74]. This control method was not followed in this work, since the mode transition between control loops can induce unwanted transient behavior as well as increasing the model complexity. The simplified battery model with the half-bridge topology is depicted in Fig. 3.40 to ease the deviation of the differential equations that govern its operation, where $R_B = R_e + R_{ct} + R_W$. The capacitances of the two parallel branches are neglected, since their time constants are negligible for the operation of the robust DC/DC converter. The inverter is replaced with a resistor, R_L, since the

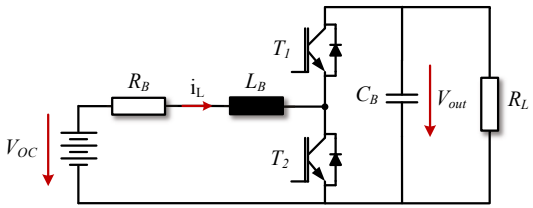

Fig. 3.40: Halfbridge converter with simplified battery model

direction of the power flow does not have an effect in the formulation of the state space equations. A more appropriate representation of the inverter would be with a controlled current source. However, since a steady state operation point and not the transient response is considered, the simplified resistor model can be utilized. The state variables of the system are identified as the current that flows through the inductor at the input of the half-bridge, and the DC-link voltage at its output. The equations that govern these state variables when the upper switch T_1 is conducting can be formulated, where each switch is modeled through its on-state resistance R_{on}:

$$L_B \frac{di_L}{dt} = V_{OC} - i_L(R_B + R_{on}) - V_{out} \tag{3.56}$$

$$C_B \frac{dV_{out}}{dt} = i_L - \frac{V_{out}}{R_L} \tag{3.57}$$

and when the lower switch T_2 is conducting respectively:

$$L_B \frac{di_L}{dt} = V_{OC} - i_L(R_B + R_{on}) \tag{3.58}$$

$$C_B \frac{dV_{out}}{dt} = -\frac{V_{out}}{R_L} \tag{3.59}$$

The on-state resistance of a semiconductor can be calculated with any given technical semiconductor datasheet. In our case medium voltage, higher power IGBTs are selected. The on-state resistance is then calculated at $T = 125°C$, for IGBT modules with a maximum collector-emitter voltage, $V_{CE} = 3.3kV$ and maximum continuous DC collector current $I_C = 200A$ in the range of $R_{on} \approx 10m\Omega$ [75]. The state space equations 3.56-3.59 can be written in a more compact form, if we define the control variable u equal to 1 when T_1 is conducting and 0 when T_2 is conducting, $R_T = R_B + R_{on}$, and $x_1, x_2 = V_{out}, i_L$:

$$x_1 = \frac{1}{C_B}(ux_2 - \frac{x_1}{R_L}) \tag{3.60}$$

$$x_2 = \frac{1}{L_B}(V_{OC} - R_T x_2 - ux_1) \tag{3.61}$$

Setting the derivatives of the state variables equal to zero in Eq. 3.60&3.61 the equilibrium point of the system can be found. Solving for the control variable in the steady state point, u_s:

$$u_s = \frac{V_{OC}}{2x_{1_s}} \pm \sqrt{\left(\left(\frac{V_{OC}}{2x_{1_s}}\right)^2 - \frac{R_T}{R_L}\right)} \tag{3.62}$$

From Eq.3.62 a condition can be formulated in order the control variable u_s to be a real number, when the output voltage obtains its minimum value, $x_1 = V_{OC}$:

$$R_{L_{min}} \geq 4R_T \tag{3.63}$$

It has been shown in [69] that, to overcome this limitation, a different topology for the DC/DC converter could have been selected, such as the full bridge circuit. However, $R_{L_{min}}$ results in a multiple of the maximum power that the battery can provide and is an unrealistic loading condition for our investigations. Therefore, despite this limitation the half-bridge is further considered for the DC/DC converter topology of the battery pack.

3.3.2.2 Controller design

Instead of implementing the usual cascaded PI-controllers structure [74] for the half-bridge, a linearized inner proportional controller is used for the current and a standard PI-controller for the outer voltage loop. The input-output feedback linearization is selected, with the relative degree of the transfer function $\delta = 1$ being smaller than the system order $n = 2$ [76]. The relative degree δ is equal to 1, since the control variable of the system u appears at the first derivative function of the state variable, as given in Eq. 3.61. A PT1-element can be selected for the desired performance of the linearized current control loop:

$$y(s) = \frac{s_x}{s + s_x} r(s) \tag{3.64}$$

with r, y the reference and output of the current loop respectively, and $s_x > 0$ a design variable. By integrating Eq. 3.64 into 3.61 the state feedback term that corresponds to the proportional current controller can be found:

$$u = -\frac{L_B}{x_1}(s_x r - s_x x_2 - \frac{V_{OC}}{L_B} + \frac{R_T}{L_B} x_2) \tag{3.65}$$

Using Eq. 3.65 and Eq. 3.60&3.61, the transfer function of the inner current control loop and therefore the control plant for the outer voltage control loop can be found:

$$G_{i_L}(s) = \frac{-\left(s + 2\frac{R_T}{L_B} - \frac{V_{OC}}{L_B x_{2_s}}\right)}{\frac{C_B x_{1_s}}{L_B x_{2_s} s_x}\left(\left((s + s_x)\, s + \frac{x_{2_s}}{C_B x_{1_s}^2 (V_{OC} - R_T x_{2_s}) + \frac{1}{C_B R_L}}\right)\right)} \tag{3.66}$$

where $x_{1_s} = V_{out}^*$, the reference for the output voltage, and $x_{2_s} = r$ are the desired equilibrium points of the system. Pole placement can be successfully implemented for the voltage control loop [69, 77]. Starting from defining a transfer function for the voltage controller:

$$K_{x_1}(s) = k_{x_1} \frac{(s + \beta_1)(s + \beta_0)}{s(s + \alpha_1)} \tag{3.67}$$

This form for the voltage controller is selected so that the poles of the transfer function of 3.66 can be directly eliminated through the zeros of the controller. In combination with the pole cancellation, an additional pole and gain factor is needed to enhance the stability of the closed looop system. The controller's pole, α_1 is placed in the far left plane of the real axis, as seen from Fig. 3.41b, to shift the crossing point of the root locus curves of the open loop system to the far left plane of the real axis. To ensure that a minimum-phase system is obtained, despite the presence of zeros in the right plane of the real axis, the

derivative of the open loop transfer function in the system equilibrium can be of assistance. More specifically, the equilibrium of the system is chosen at the crossing point of the root locus curves, where the derivative of the open loop tranfer function becomes zero [76]:

$$\frac{d(G_{i_L}(s)\cdot K_{x_1}(s))}{ds} = 0 \quad , \quad \Rightarrow \quad k_{x_1} = \frac{L_B x_{2_s} s_x}{C_B x_{1_s}} \tag{3.68}$$

Solving Eq. 3.68 the last controller parameter k_{x_1} can be found. All battery model and controller parameters are listed in Appendix A, in Table A.8.

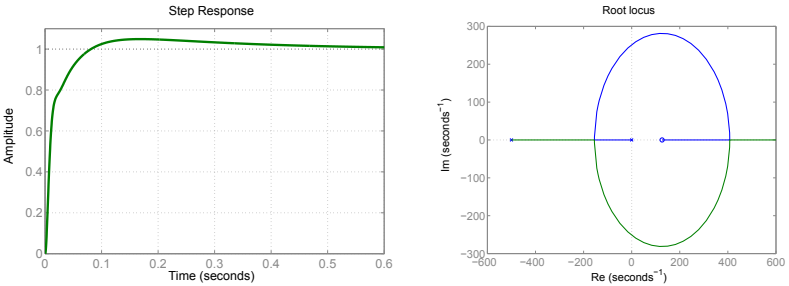

(a) step response of closed loop (b) root locus of open loop

Fig. 3.41: DC/DC converter controller validation

A small overshoot is observed in the step response of the closed control loop shown in Fig. 3.41a. It is however in an acceptable region and lines along with the guideline followed also for the design of the DC-link voltage controller of the grid feeding inverter, namely to achieve fast response of the DC-link control unit in case of transients.

3.4 Modeling towards real time simulation

The previously explained theoretical models are implemented for real time simulation scenarios of different hybrid microgrids configurations. To prepare real time simulation models, a few design rules are explained in the following sections.

Discretization principles For any type of simulation of a model based on an electrical system, the differential equations governing the system should be solved. Starting from the following generic differential equation:

$$\frac{dx}{dt} = f(x,u) \tag{3.69}$$

where u is the input variable and x is the output variable. The notation can be simplified, setting $f[x(t_k), u(t_k)] = f[(x(k)), u(k)]$ [78]. By integrating the differential equation 3.69, the following equation is obtained:

$$x(k) = x(k-1) + \int_{(k-1)h}^{kh} f \; dt \tag{3.70}$$

where h is the sampling time of the discretization method. As most appropriate method the Tustin method or also known as trapezoidal integration method is selected:

$$x(k) = x(k-1) + \frac{h}{2}[f(k) - f(k-1)] \tag{3.71}$$

In the following table useful functions based on the continuous Laplace operator, s are transformed with the help of the Tustin method and the discrete z-operator: It is highly recommended to discretize each function used in any model intended

Ideal integrator, $\frac{1}{s}$	$\frac{h}{2}\frac{z+1}{z-1}$
1^{st} order system, $\frac{1}{Ts+1}$	$\frac{h(z+1)}{z(2T+h)+h-2T}$

Table 3.4: Exemplary discretized functions

for real time simulation to minimize modeling complexity.

PWM sampling implementation The expressions stated in Table 3.4 can be useful when in a simulation environment different sample times are present. This is the case when a controller is working with specific sampling intervals trying to regulate a 2- or 3- level, 3-phase inverter. A quite popular solution is the asymmetrical regular sampling, or double-edge modulation. With this sampling technique, the reference signal is compared with the carrier signal only when the carrier signal reaches its edges, that means, twice in each switching period. The benefits of asymmetrical regular sampling based PWM can be briefly summarized:

- Compared to natural sampling based PWM, regular sampling results in symmetrical modulation [79]. For higher switching f_s to fundamental frequency f ratios($\frac{f_s}{f} > \approx 10$), regular sampling can not only suppress the third, fourth and fifth lower sidebands of the carrier, but overall improve the frequency spectrum of the output pulse width modulated signal.
- The digital implementation of regular sampling can be not only significantly convenient for modern microprocessor based control platforms [80], but also for simulation purposes. First of all, the simulation models represent the system under investigation more precisely with a realistic sampling

method, since regular sampling is state of the art in PWM implementations. Second and most important, the complexity of the simulation model is significantly reduced. With double-edge modulation all measurement signals are sampled at a slower rate than the sample time in which the simulation solver works to discretize and solve the differential equations of the system. In this way, all data coupled with the inverter's controller change their values in a slower rate than the solver sample time and decrease the amount of data the solver has to manage during one 'solving' interval.

Combining asymmetrical regular sampling with one sixth third harmonic injection a PWM scheme with high dc-link voltage utilization, superior harmonic performance [43] [54] and equivalent results with space vector modulation can be obtained [81].

Employing a commercially available real time simulator Parallel to the previously mentioned modeling aspects, when working with a commercially available real time simulator a few additional features can be exploited. In this work the OP5600 real time simulator from the company Opal-RT® is used. This simulator provides extensive model libraries designed for real time simulation. More specifically, an intermediate model between average value based models of semiconductors, which retain the average voltage dynamics neglecting the PWM process and consequently harmonics [54], and ideal switching models that neglect losses can be found. These intermediate models together with overlapping discretization solvers simulate switching events with high accuracy by approximating between values obtained at each sample time to produce the correct voltage and current waveform [82]. In this way the ideal switching process of semiconductors is combined with the higher sample times needed for grid studies.

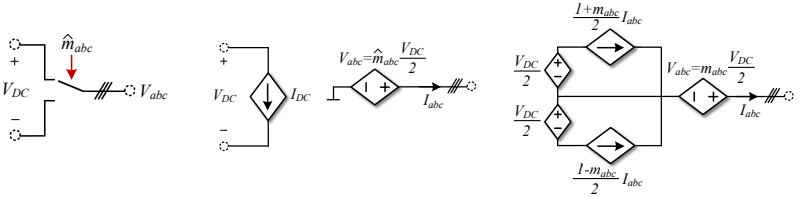

(a) switching (b) intermediate [83], [84] (c) average [54]

Fig. 3.42: Modeling variants of 3-phase inverters

In Fig. 3.42 the modeling variants of an inverter are depicted, where m_{abc} and $\hat{m}_{abc}$ is the input and output of PWM respectively. That means that m_{abc} are the sinusoidal control signals that are led to the modulator and $\hat{m}_{abc}$ the generated

pulses respectively. The DC-link current in the intermediate inverter model can be calculated from the power balance equation [85]:

$$I_{DC} = \frac{(V_a - V_b)I_a - (V_b - V_c)I_c}{V_{DC}} \tag{3.72}$$

where V_i, I_i with $i = a, b, c$ are the phase voltage and current respectively at the output of the inverter. In that model, the halfbridge of the inverter is replaced by an ideal voltage source that directly amplifies the output of the modulator. The voltage at the output of the inverter remains pulsed. On the other hand, in the average model no switching takes place and the semiconductors are neglected, producing an ideal sinusoidal voltage at the output of the inverter.

4 Black start and synchronisation techniques

After preparing the models of the main microgrid components, the next step is to form various microgrid configurations and investigate the problems that rise during their operation. Our investigations are targeted solely to standalone microgrids that have no interconnection with a stiff grid. That could be the case of remote islands which should rely only on autonomous power solutions. Once the microgrid topology is selected, a start-up process as well as consequently individual synchronisation processes for each generator should take place. To verify the proposed synchronisation techniques the system stability is supervised. When we are referring to stable operation of paralleled generators, it means that all generators are in synchronism, or colloquially in step [10]. The focus of our investigations are the grid forming units, such as the diesel generator and the grid forming inverter in parallel mode. These units carry the main duty of stabilizing the microgrid despite transient effects.

4.1 Black start of hybrid microgrid

One crucial operational issue is booting up a microgrid, the black start as this start-up process is also called [86]. At least one grid forming unit is needed during all operational modes of any grid. In conventional stiff grid structures, black start is defined as the ability to boot up the system without importing external power. In this way, also in microgrids, black start means that the microgrid has the ability to start operating on its own, without external support. Communication between generators is essential during the black start process: not only if more than one generators are involved to generate the connecting sequence, as well as to control the loads to be connected [87]. Sequencing algorithms based on multi-agent deployment can be implemented, which receive and evaluate load demands and generator's operation status to coordinate the start-up procedure [88]. The black start of a microgrid can be divided in two different cases: One is the first time start-up process of a microgrid for its operational 'debut'. Secondly, re-energizing the grid after the occurrence of a fault. Although the goal is the same, different principles gain importance for each case. The grid forming unit that receives the first order to start its booting process is called

master generator [89]. The generic criteria for the appointment of a grid unit as the master unit in a black start process can be summarized as following [90]:

- Short start-up time for fast restoration of microgrid.
- Self starting with self powered auxiliary systems.
- Should be able to handle the heavy inrush load current at the starting of re-energizing process due to prior de-energized conditions of the loads.

Whereas the second and third criteria are applicable for both black start cases, a short start-up time and fast restoration is only valid in case a fault has previously occured. In case of hybrid microgrids a diesel generator is present, which is characterized by its slower turning-on process compared to inverter-interfaced distributed generators. It is common for the diesel generator to overtake the black start process as a master generator and the inverters to follow [89]. Battery based distributed generators can also be employed as master generators [91] to re-energize the microgrid faster in case of a fault. A renewable energy source can be also theoretically appointed as the first component of the black start process. The control mode of its grid inverter should switch to grid forming mode and this operational mode can remain so as long as the input energy source is enough to stabilize the intermediate DC-link [90]. The appointment of the master generator depends mainly on its rated power, so that a significant number of loads can be connected to the grid as soon as possible. In the case of re-energizing, all loads should be initially disconnected and remain so until steady state is reached, and all inverters could switch to grid forming mode to accelerate the connection of all microgrid loads [92].
The benefits of the existence of robust grid forming units in a microgrid can be also utilized for the re-energization of an interconnected mainland grid. The volatile microgrid can be first booted up to support sensitive and emergency loads, with the interconnection of a stiffer grid to follow [93], [94]. The restoration of a more complex grid is typically performed through booting-up several sub-systems working in parallel to minimize the re-energizing process [95]. In that case, provided that storage systems are available in the grid structure, their grid forming mode of operation can significantly reduce the required black start time of a sub-system. Despite the obvious advantages of fast-tracking grid forming units, the coordination of only the generators is not sufficient for a smooth re-energizing process. A restoration chain of command between generators and loads is also crucial for the black-start process but exceeds the focus of this work.

Black start test scenario

In the following section the test scenario of an exemplary black start of a medium voltage hybrid microgrid is carried out, with the microgrid topology depicted in Fig. 4.1. The diesel generator is first appointed as master generator and secondly the grid forming inverter overtakes the start- up process. This test

scenario should document the time constants difference of rotating and non-rotating distributed generators. The parameters for the diesel generator that are used in this test scenario can be found in [37], with a few indicating parameters already given in Table A.3. The grid forming inverter is sized equally to the diesel generator ($S_n = 6.75\ MVA$) to ease drawing conclusions on their behavior. The detailed inverter parameters are given in Table A.6. From that table, it is evident that the filter losses for this power level are no longer viable and a more reasonable solution would be to split the power to several inverters in parallel. However, in this scenario, the focus is on the fundamental difference in the transient response of the grid forming units, which is independent of the LC(L) filter output of the inverter. Therefore, the unrealistic filter losses of the inverter are neglected. The current limitation for the inverter is selected at $I_{lim} = 1.1\ pu$. The droop gains for active and reactive power are within limits, as given in chapter 2. They are however selected lower than their upper limits, to enable a smooth parallel operation of the distributed generators. The higher the droop gains, the lower the stability margin of the system, causing oscillations during transient states. The DC-link of the inverter is modeled as an ideal DC voltage source, since in this time range of a few hundred milliseconds up to a few seconds, the modeling focus lies on the grid part and the interactions between generators. The test scenario proceeds as following: The master generator is

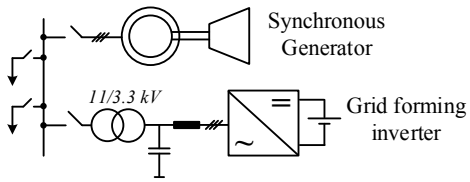

Fig. 4.1: Microgrid configuration for black start scenario

initially booted to reach its steady state voltage and frequency values. Then, once an equilibrium is reached, a step load change that equals 50 % of the nominal load of the generator takes place. Once the system reaches its new steady state point, a second step load change occurs, so that in the end of the test scenario the generator's current reaches its nominal value. At this point it should be once more noted that both mechanical parts and excitation system of the synchronous generator are considered in the model ideal and their significant start-up times are not further considered. The test scenario considers an ideal operation of them without supporting elements typically present for gas turbine units and large diesel aggregates, such as start-up frequency converters for the excitation systems. If the start-up times of these components were also considered, the start-up process would exceed the range of a few minutes. In Fig. 4.2 the results of both test scenarios are shown. The first significant observation

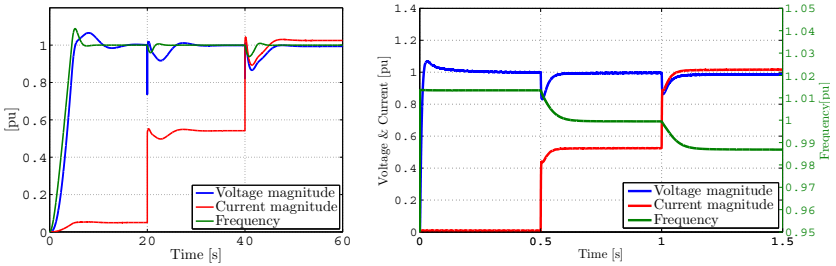

(a) with diesel generator (b) with grid forming inverter

Fig. 4.2: Black start test scenario

is the time scale in both processes. Starting from Fig. 4.2a, it is apparent that the synchronous generator reaches its equilibrium after each transient process after more than fifteen seconds. This is to be expected, since the generator's inertia is responsible for the suppression of any instantaneous speed variation. Observing Fig. 4.2b on the other hand, it is evident that, since the inverter does not poses any mechanical inertia, it can follow any transient change in a matter of tens of milliseconds. The transient response of the inverter is mainly affected from the time constants of the low pass filters used in for active and reactive power measurement in droop control. Comparing also both figures, the difference in the frequency drop can be documented, where the inverter can control the output frequency in a quite narrow range around the nominal frequency. The steady state frequency drop is due to the implementation of the droop characteristic. Lastly, in Fig. 4.2a, during the initial start-up process, the generator is not left open-circuited, but has a small output load. This is due to the modeling interconnection technique used (3.5), which contains a current source as main component that cannot be left open-circuited.
In the following sections the synchronisation of grid forming units is analyzed, once the black start process is successfully completed. The synchronisation process of a grid feeding inverter is omitted, since it is well developed in the state of the art. The typical method includes charging the DC-link of the inverter with resistors and bypassing them after the DC-link has reached its reference value [13].

4.2 Synchronisation of grid forming inverter

The synchronisation technique for the grid forming inverter is similar to the one that modern synchronous generators employ to connect to the grid. More specifically, the following measures should be taken prior to synchronisation [96], [97]:

- The produced electrical frequency of the generator is equal to the one of the grid. That means that the generator's rotating speed should be adjusted to match the grid frequency.
- Synchronous generator and grid have the same phase sequence. That could arise a problem right after the generator's installation and during the first grid synchronisation attempt.
- Output voltage magnitude of the generator matches the grid voltage. If the magnitudes don't match, the generator will be connected and work in over-excited or under-excited mode, depending on which voltage is higher.
- Not only the magnitude but also the voltage phase angle should match, this can be supervised by observing the zero crossing points of both voltages.

If not all four synchronizing conditions are met, equal load sharing cannot be achieved and a transient process will occur that will lead to a massive reactive power circulation between generator and grid. In the past light bulbs were employed to observe the phase difference between connecting points. They were later replaced by synchroscopes, and in modern power systems by controllers that overtake and perform the synchronisation process automatically.

4.2.1 Control structure modification

The control structure proposed in this work is based on the synchronisation criteria that apply for synchronous generators and were listed above [98] & [99]. Alternatives can be found, where a grid forming inverter is connected in grid feeding mode and its control structure is changed afterwards to grid forming mode [100]. The control structure of the grid forming inverter working in parallel with other grid forming units (as depicted in Fig.3.30 & 3.31) is modified for the synchronisation. In Fig. 3.30 it is shown that the inverter control's objective is to control the voltage across the filter capacitor. That could work ideally if the grid forming inverter works in standalone mode, or is the master generator in parallel mode. Once however it is required to connect to an already up-and-running microgrid, the grid voltage is required. Therefore, a phase-locked-loop (PLL) is employed to facilitate the synchronisation. As shown in Fig. 4.3 the grid voltage V_g is measured for the synchronisation. The objective is to control the output voltage of the inverter right after the transformer V_i to match the grid voltage, so that a smooth synchronisation can take place. Prior to the connection of the inverter to the grid, the output current i_2 is zero and the output voltage is equal to the capacitor voltage, $V_i = V_C$. Therefore, controlling the capacitor voltage to match the grid voltage results in a synchronization process without transient phenomena.

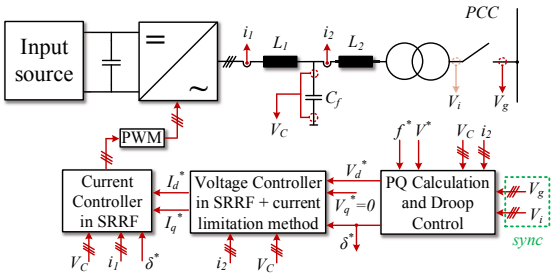

Fig. 4.3: Modifications for synchronisation

The sequence criteria are followed. Frequency, voltage and angle should be synchronized as shown in Fig. 4.4 with the use of a PLL for the frequency and two PI controllers for the voltage amplitude and angle. Then, the restoration

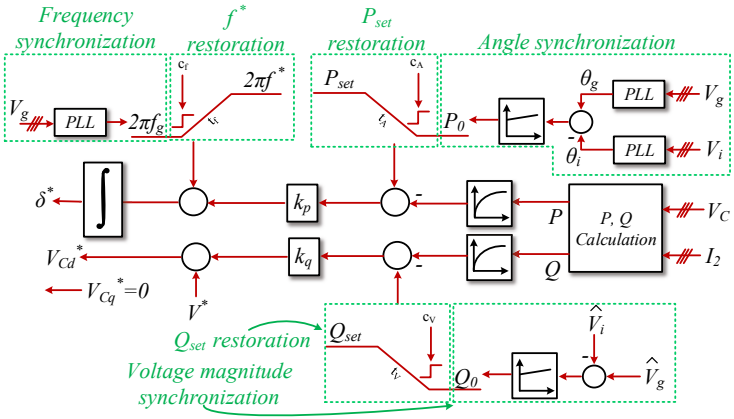

Fig. 4.4: Controller modification

process for the desired frequency, active and reactive power setpoints is smoothly initiated with ramps that have t_f, t_A and t_v duration respectively. The ramp duration depends on the desired synchronization duration and varies in the test scenarios that follow. The reactive power and frequency desired setpoints are initiated with the same firing pulses c_f and c_v. Then, the setpoint for the active power is initiated with the pulse c_A so that the system can reach its steady state point and both generators can share the load. The objectives of this control scheme is to avoid frequency and voltage drops during the synchronisation, and circulating reactive current between the grid forming units.

4.2.2 Implementation

The control sequence explained in the previous section is implemented in a real time simulation test scenario of the exemplary microgrid of Fig. 4.1. The distributed generators are once more designed with the same rated power, $S_i = 6.75$ MVA with the rest model parameters given in Table A.10. In this configuration the grid forming inverter is directly coupled at the same voltage bus bar with the synchronous generator to demonstrate a worst case scenario, where the connecting impedance between both generators is practically negligible. The active and reactive power output of each distributed generator in the following figures are scaled with their rated power, S_i. From Fig. 4.5a the goal of the synchronisation process can be observed. Before connecting the inverter at $t = 40$ seconds the diesel generator has been booted and it delivers active power close to its nominal one. Once the synchronisation of the grid forming inverter is completed, after $t = 90$ seconds, the load is effectively shared between both generators and the microgrid has reached a new steady state point. At Fig. 4.5b

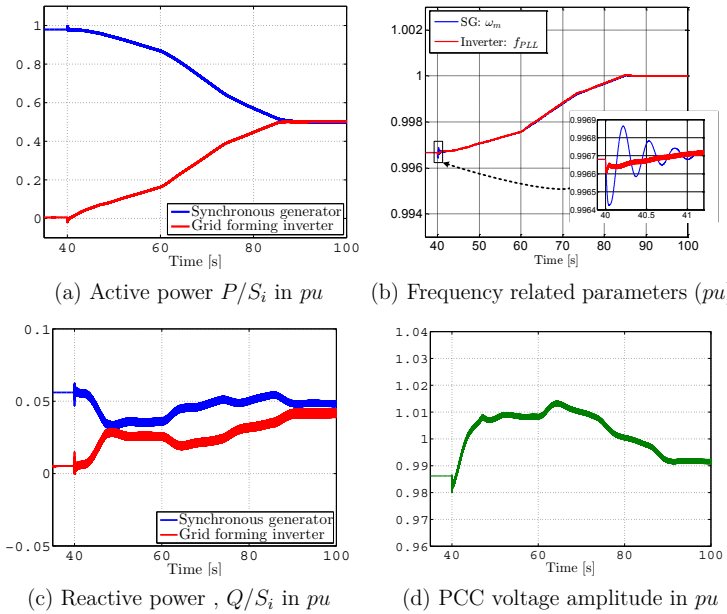

(a) Active power P/S_i in pu

(b) Frequency related parameters (pu)

(c) Reactive power , Q/S_i in pu

(d) PCC voltage amplitude in pu

Fig. 4.5: Grid forming inverter synchronisation

the rotational speed of the synchronous generator and the frequency measured by the PLL at the output of the grid forming inverter are depicted. The droop gains are selected relative small, therefore the frequency deviations are also minimal. Despite that, the ramps shown in Fig. 4.4 can be vividly observed in the

frequency curve. During $t = 40$ and $t = 60$ seconds the frequency and reactive power setpoints ramps are active. Then, during $t = 60$ and $t = 80$ seconds the ramp for the active power setpoint is active. From Fig. 4.5d the stiffness of the microgrid can be evaluated.
It has been briefly explained in section 2.1 that in weak grids the generators are strongly interconnected. In this case, the coupling can be explained by the voltage response of the microgrid. Since the two generators are connected in the same voltage bus, the grid impedance from each generator to the load, as well as between both generators is minimal, and an over-voltage of almost 0.02 pu is demonstrated. Despite the fact that the distributed generators are connected in the same voltage bus, the reactive power flowing into the microgrid is not fully shared by the two generators. This is due to the impedance of the transformer of the grid forming inverter, that produces a deviation of almost 0.01 pu. In Fig. 4.5c the impact of harmonics on the microgrid can also be observed. Before the connection of the inverter the measured reactive power of the synchronous generator does not show an harmonic content, and as soon as the inverter is connected, a small ($\sim 1\%$) ripple is evident. This harmonic content for both generators is to be expected and lies in an acceptable region. Regarding the new steady state point, a few interesting points can be observed from Fig. 4.5b & 4.5d. The frequency is close to 1, since the nominal setpoint for both generators is $P_{set} = 0.5\ pu$ and the voltage drops lower than 1 pu since a reactive power/voltage droop characteristic with $Q_{set} = 0$ is employed.

Synchronization at low loading conditions

To generalize the real time simulation results of the previous section, a second test scenario is prepared, where the central load is halved. Furthermore, the impact of selecting a higher gain for the P/f droop characteristic is also demonstrated with a faded line in the frequency response (see Fig. 4.6b). The active power output of each generator is in this case also halved, and the results of the synchronisation process are similar to the previous case of nominal load. The inverter is once more connected at $t = 40$ sec and the setpoints ramps are activated subsequently. A difference that can be noticed is that in this case the active power output is not strongly affected from the activation of the frequency and reactive power setpoint restoration ramps. Due to the presence of lower load, the frequency deviation in this point is also minimal and therefore the active power sharing is not altered during the setpoint restoration. Observing the zoomed frequency in the synchronisation moment, it is also shown that the oscillation of the rotational speed of the generator is not affected from the different loading conditions and its amplitude remains in an acceptably low region (< 0.001 pu). Increasing the P/f droop gain by 50% the amplitude of the oscillation is almost doubled, but remain in safe operating regions (≈ 0.001 pu). Once the synchronisation is completed, the steady state frequency deviation follows the selected droop characteristic with an increased droop gain. An interesting

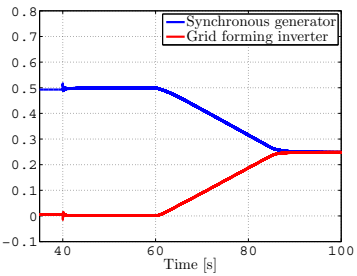

(a) Active power P/S_i in pu

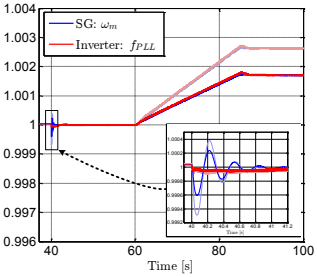

(b) Frequency related parameters (pu)

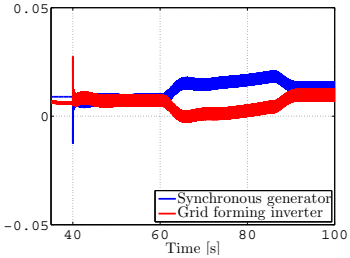

(c) Reactive power , Q/S_i in pu

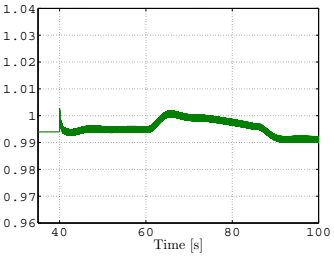

(d) PCC voltage amplitude in pu

Fig. 4.6: Grid forming inverter synchronisation at lower loading conditions

point regarding the reactive power sharing is the synchronisation moment, upon which a peak is documented. The observed peak however (< 0.02 pu) does not pose a threat for the stability of the system. The over-voltage at the common voltage bus is also in this case minimized, since a lower power flow shift takes place.

4.2.3 Synchronisation of a 2nd grid forming inverter

A point worth to be documented is also the synchronisation of a second grid forming inverter in such a hybrid microgrid. The same control structure shown in Fig. 4.4 is once more applied for an additional inverter connected to the microgrid of Fig. 4.1. This test scenario follows the synchronisation process of the 1st inverter, and the second inverter is synchronized as soon as the first two generators reach their steady state, at $t = 100$ seconds. The duration of the synchronisation ramps t_f, t_A and t_v are chosen in this case smaller, to accelerate the inverter connection. This could be quite useful in case of grid restoration after a fault, where the faster response capabilities of an inverter should be fully exploited. The rated power of the 2nd grid forming inverter is selected equal to the other distributed generators, namely $S_n = 6.75\ MVA$ and the rest of the

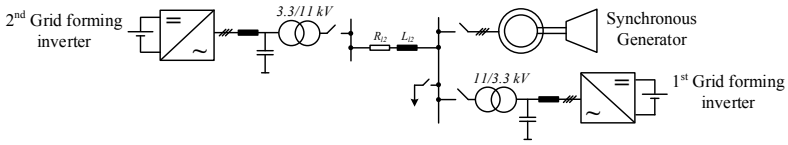

Fig. 4.7: Connection of a 2nd inverter to the microgrid of Fig. 4.1

model parameters are given in Table A.10. As it can be observed from Fig.

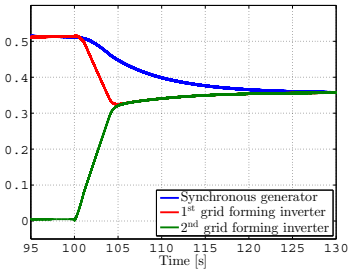

(a) Active power P/S_i in pu

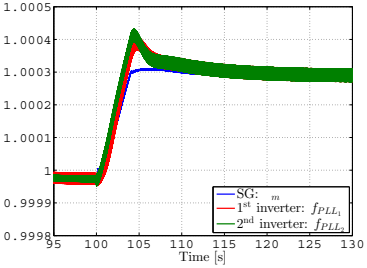

(b) Frequency related parameters (pu)

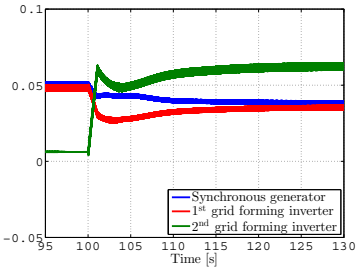

(c) Reactive power Q/S_i in pu

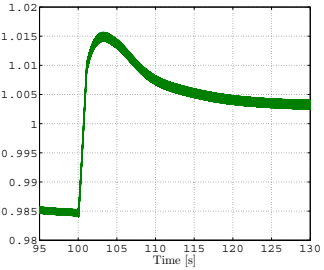

(d) PCC voltage amplitude in pu

Fig. 4.8: 2nd grid forming inverter synchronisation

4.8a, the second inverter connects faster to the microgrid, compared to the first one. The diesel generator reacts also in this case quite slowly, depending on its mechanical inertia, and takes a certain amount of time to reach the new steady state point. The inverters however are able to synchronize faster, without producing any unwanted transient effects. That could be quite useful in the case of re-energizing a grid after a black out, where all available generators should stabilize the grid as soon as possible. The duration of the restoration ramps in this test scenario is significantly shortened, and that can be also first confirmed from Fig. 4.8c. The reactive power setpoint ramp produces the linear increase in the

output power of the 2nd grid forming inverter. The voltage, depicted in Fig. 4.8d is directly affected from this restoration method. A voltage amplitude increase is documented, measured at the PCC of the first two distributed generators. This is to be expected, since both initial generators reduce their reactive power output and a new steady state point in the reactive power sharing is achieved. Observing this steady state point for the reactive power sharing, the inherent disadvantage of the Q/V droop characteristic is demonstrated. The three distributed generators are not connected to the same voltage bus and the voltage amplitude deviations measured at the output of each generator depend on the load location and the length of the distribution lines of the grid. Since these deviations are unequal, the reactive power flowing through the microgrid is not fully shared among the generators, and the 2^{nd} grid forming inverter provides the grid with excessive reactive power. The reactive power sharing problem is not further investigated in this work. Communication based methods have been proposed that utilize measurements from all distributed generators, to facilitate accurate reactive power sharing. These communication methods can be integrated in the primary [101] or in the secondary [102] control scheme of each distributed generator. An alternative to communication based methods would be the traditional local compensation method that prevails in modern power systems. In Fig. 4.8b the parameters related with the transient frequency response of the microgrid are shown. In this figure it is evident that the 2nd grid forming inverter, through its frequency reference successfully pulls up the two other generators. It is also shown that the frequency reference of the 1st grid forming inverter manages to follow faster the frequency reference of the 2nd grid forming inverter. The synchronous generator, with its behavior documented through its rotational speed, synchronizes with the other two generators shortly after the 2nd synchronisation process takes place.

4.3 Conclusions of black start and synchronisation techniques

In this chapter the first practical issues that rise with the deployment of microgrids are addressed. First, the black start sequence, as far as the generators are concerned, is explained. Then, the benefit of assigning a grid forming inverter as a master generator is demonstrated by comparing its fast booting up process to the equivalent of a synchronous generator. Furthermore, a synchronisation method for grid forming inverters is introduced that achieves smooth and fully controlled grid connection. Reactive power exchange between generators during the synchronisation is avoided and frequency and voltage show a stable transition with minimal deviations from their steady state points. The flexibility of grid forming inverters during their grid connection is verified with the synchronisation of an additional grid forming inverter. Through real time simulation results it is demonstrated that the grid forming inverters can not only re-energize faster a microgrid after a fault, but also speed up the response of conventional synchronous generators working in parallel.

5 Load sharing considerations

A decisive issue to any modern power system is controlling the power flow between the grid components that generate and consume electrical energy. Similar to stiff grids, also in microgrids it is crucial to supervise this power flow and it could be more problematic since the available energy is strictly limited due to the decreased number of generators. To facilitate the power flow from the generation points to the consumption points, load sharing between the distributed generators should be achieved. The approach selected in this work to realize load sharing is based on droop control, as theoretically explained in chapter 2. This chapter is focused on the problems that arise during the parallel operation of grid forming units, as far as load sharing is concerned.

5.1 Modular implementation of droop control

Typical droop curves for conventional synchronous generators are shown in Fig. 5.1a. As explained in chapter 2, the active power is 'drooped' from the frequency, so that all generators can respond equally upon load changes, building up 'artificial' means of communication. The droop curve is characterized through three parameters, such as the active power setpoint P_{set}, the nominal frequency f_0 and the maximum allowed frequency drop Δf. A similar curve is also built up for the reactive power/voltage coupling. Despite the fact that medium voltage microgrids with a complex and not purely inductive impedance path are considered, this Q/V droop characteristic is also implemented to improve reactive power sharing between generators.
The main difference between the two generic droop characteristics is that, since conventional generators and not bidirectional generators are still considered, the P/f droop curve lies only at the first operational quadrant, since power cannot be absorbed. The Q/V droop curve on the other hand reaches also to the second quadrant, since reactive power can be absorbed and produced from conventional synchronous generators. It is obvious that if two or more generators are working in parallel and have the same power rating, they will share equally the load if identical droop curves are applied. Once the power rating becomes unequal, the droop curves should be modified so that the generators can share the load proportionally to their rated power. Proportional power sharing is desired in order to ensure stable operation. Larger, stiffer generators should overtake a

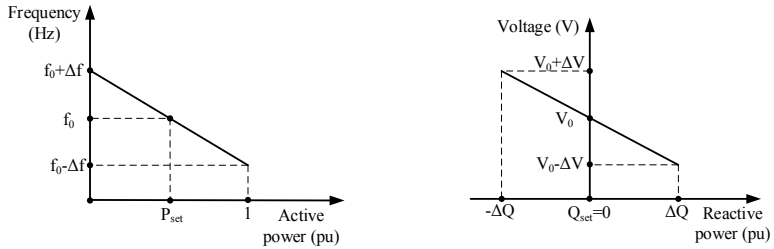

(a) P/f (b) Q/V

Fig. 5.1: Generic droop characteristics

bigger portion of the load compared to smaller weaker generators, which are more prone to disturbances.

The droop gains k_P, k_Q are defined through the maximum frequency & power or voltage & reactive power deviation, as given in Eq. 5.1 and graphically depicted in Fig. 5.1.

$$k_{P_i} = \frac{2\pi \cdot \Delta f}{\Delta P} \quad , \quad k_{Q_i} = \frac{\Delta V}{\Delta Q} \tag{5.1}$$

The maximum values for the droop gains that ensure stable operation in generic medium voltage microgrids with short distribution lines have been given in Fig. 2.10 & 2.11. As already seen in chapter 4, the droop gains are selected at least 10 times smaller than the actual limitations derived in chapter 2. The reason is twofold:

- First, since the grid forming units in this work have different attributes and characteristics, smooth transient response is always desired. Larger droop gains would force the generators to synchronize faster, producing frequency and voltage transients.
- In parallel, it is also demonstrated that, since droop gains are relatively small, the steady state frequency and voltage deviation of such a microgrid is minimal. If there are no directly-coupled rotating machines as loads connected to the microgrid, the need for secondary control can be questioned. In this direction leads also the development of the SoC-Adaptive droop control, introduced in section 5.3, which aims at grid autonomy and as much as possible communication-free operation. In other words, the secondary control could be implemented not with the focus of frequency restoration, but only for optimizing the power flow in the microgrid in a wider time scale.

Introducing microgrids as abstract elements of power systems that will change radically the way the grid is structured is not a leading guideline in this work.

The priority is set to the practical problems that occur when incorporating microgrids in the philosophy of the modern grid principles. Therefore, also in the case of droop control, it was selected to design droop control of inverters similar to the one of synchronous generators and not modify the droop control implementation of synchronous generators for microgrid applications. A step in the opposite direction would be to generate the setpoint for the speed governor through power calculation, similar to the case of the grid forming inverter [103]. The generator speed governor of Fig. 3.8 remains intact and the droop gains and setpoints of inverters as firstly shown in the general droop characteristics of Fig. 2.5 are calculated.
An additional feature of the strategies proposed in this work is modularity. The implementation of droop control should be flexible, so that the integration of components with different rated power, voltage level and characteristics in the microgrid could be accelerated. In equation 5.2 the desired droop gains and setpoints are given so that two distributed generators working in parallel can share any load proportionally to their rated power, S_i.

$$\frac{k_{P_1}}{k_{P_2}} = \frac{S_2}{S_1} \quad , \quad \frac{P_{set_1}}{P_{set_2}} = \frac{S_1}{S_2} \tag{5.2}$$

The proportionality that connects droop gains and setpoints with the rated power can be derived from the nature of droop characteristics. In a typical droop curve provided in Fig. 5.1, to obtain proportional power distribution a proportional frequency deviation among the generators should be built. This deviation is directly dependent on the droop gains and setpoints selected. The desired frequency deviation is calculated as shown in Eq. 5.3:

$$\frac{\Delta P_1}{S_1} = \frac{\Delta P_2}{S_2} \quad \& \quad \Delta f_1 = \Delta f_2 \tag{5.3}$$

Combining Eq. 5.1 & 5.3 the reverse proportionality that governs the droop gains in the first part of Eq. 5.2 can be explained. Similar equations apply also for the reactive power/voltage characteristic.

Different droop characteristics

Different droop characteristics can be applied depending on the nature of the distributed generator that supplies the grid forming inverter. Such an example is the case of batteries as prime energy source of the grid inverter. In this case, the distributed generator could absorb or deliver active power to the grid, and the droop curve can vary for battery- or diesel-based generators, as shown in Fig. 5.2a.

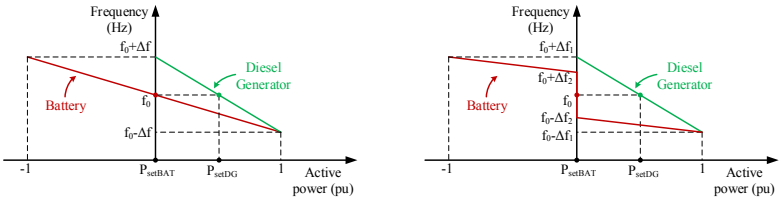

(a) Typical droop curve

(b) Droop curve with dead zone

Fig. 5.2: Droop characteristics for different generators

Batteries are prone to reduced life cycles if not charged and discharged optimally. Therefore, the implementation of a droop characteristic as in Fig. 5.2a would lead to constant change in the power output of the battery depending on the actual grid load. In Fig. 5.2b an alternative droop curve is shown. In this case, the droop control is implemented with a frequency supervision unit. If the frequency is close to its nominal value, the battery should not provide or absorb active power to the grid. This alternative droop curve is highly recommendable for hybrid microgrids, since it should be avoided to charge the battery from the diesel generator and the battery should be active only in near the limits operation [104], [105], [106]. The frequency supervision should take place in steady state mode and not during transient processes, to ensure stable operation and not constant switching between control modes. Waiting for the system to reach a frequency equilibrium is highly important since non-stiff grids with few or none inertia-based generators can experience rapid frequency changes. Since operational planning in a wider time scale is not the focus of this work, the alternative droop curves are not further considered in the following test scenarios.

Observing Fig. 5.2b one can reach the conclusion that this mode of operation is similar to grid feeding mode with P/f droop characteristic, as depicted in Fig. 3.23. The difference however lies on the primary response of the inverter in these two control modes. In grid forming mode the inverter has an active part in load sharing and reacts in a robust way to any grid disturbance. In grid feeding mode the inverter supports the grid in case of over- or under-frequencies in a similar way. However, this support is inherently slower than grid forming control, since it relies on the primary response of the grid forming units. Therefore, it is not to be doubted that a grid forming unit, even with a dead zone, is more grid-friendly than grid feeding operation with grid supporting functions.

5.2 Transient load sharing

A real time simulation test scenario is formulated to demonstrate the implementation of droop control in hybrid microgrids, with generators working in parallel with different rated power. The hybrid microgrid of Fig. 4.1 is once more considered. Since all grid components connected at the same bus bar, a minimal change in the state of any component of the common bus will rapidly affect all grid participants. Identical P/f droop curves are applied in both generators to demonstrate successful load sharing after the step load change. The rated power of the grid forming inverter in this case is selected at $S_{GFo} = 2MVA$ and the rest model parameters for this test scenario are given in Table A.11. The rated power of the grid forming inverter is selected quite lower than the one of the diesel generator to demonstrate:

- The implementation of droop control for generators with different rated power, where upon a load change, the generators should overtake a portion of the load depending on their power capacity.
- The impact that this lower rated power has on the transient stability of the two-generators weak microgrid.

In Fig. 5.3 & 5.4 the transient response of the two-generators system of Fig. 4.1 upon the load step change at $t = 80$ sec is depicted. Previous to the load change the system has been successfully booted-up and reached a steady state where both generators share equally the initial load.

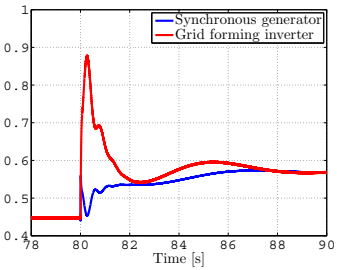

(a) Active power P/S_i in pu

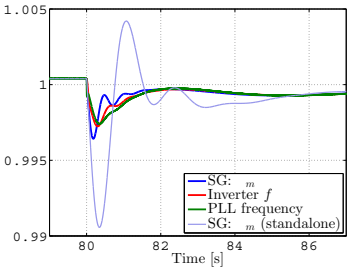

(b) Frequency related parameters in pu

Fig. 5.3: Load sharing upon a step load change (i)

The active power output of each generator is scaled to each generator's rated power, as shown in Fig. 5.3a. In this way, the proportionality of load sharing can be easily observed, since in steady state each generator should provide equal amount of active power in proportion to its rated power. The first observation is that once the system reaches its new steady state, at $t = 90$ seconds both generators provide the same amount of active power. The proportionality of load

sharing is therefore demonstrated. The focus lies in-between the two steady state points. In $t = 80 - 90$ seconds the grid forming inverter overtakes almost the whole amount of the newly introduced load. The duration of this transient period is determined mainly from the inertia of the synchronous generator, as shown in Fig. 5.3b. An inverter based generator, as long as the power input source can provide the required amount of power, can in a matter of milliseconds set its output current and frequency to the desired values. The diesel generator on the other hand, due to its inertia experiences a significant drop in its rotating speed, which in turn influences the output frequency. Until the synchronous generator can set the new desired frequency, the parallel inverter overtakes the whole amount of load. This transient state will be further on called *'transient load sharing'* [103]. In the test scenario depicted in this section, since the introduced load is comparable to the rated power of the grid forming inverter, right after the step change, the inverter provides almost its full capacity, until the diesel generator slowly provides the active power assigned to its rated power.
The test scenario is once more repeated without the presence of the grid forming inverter. The synchronous generator is working in standalone mode and the step change is decreased so that the generator receives equal load in both cases. The response of the mechanical speed of the generator is shown in Fig. 5.3b and the voltage response in Fig. 5.4b. In this way it is compared if the microgrid shows a better frequency and voltage response with the presence of the grid forming inverter. To verify that the step load change is proportional in both cases, it can be observed that the mechanical speed of the generator before and after the step load change is identical. The voltage steady state point is not identical in both cases because the inverter introduces a further voltage drop due to the leakange inductance of its transformer.

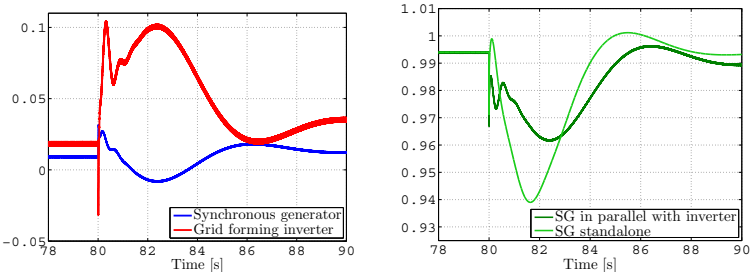

(a) Reactive power Q/S_i in *pu*

(b) Voltage amplitude in *pu*

Fig. 5.4: Load sharing upon a step load change (ii)

The reactive power sharing, seen in Fig. 5.4a, is not proportional to the rated power, since the connecting impedance of each generator is not equal. The inverter has the additional leakage inductance of its transformer, that requires the injection of reactive power. The diesel generator however does not contribute to

this reactive power demand providing less than 0.02 pu of its rated power. As already mentioned, the focus of this work is only primary grid control without implementing secondary control as it would be normally the case. Therefore both voltage and frequency in steady state have deviations from their nominal references. The amplitude of the common PCC voltage is depicted in Fig. 5.4b. A voltage drop is observed which reaches almost 0.04 pu. From this minimal voltage drop the direct advantage of the selected control algorithm for the grid forming inverter is demonstrated. Although the step load change power is almost 0.15 pu of the installed generators power capacity, the voltage drop is even lower than 0.05 pu. This is due to the robust reaction of the grid forming inverter, that supports the grid with its fast characteristics.
The observation of the frequency and voltage response with and without the grid forming inverter leads to significant conclusions. The frequency and voltage drop in the case of the standalone synchronous generator are almost 3 and 2 times respectively higher than the parallel mode. Therefore, although transient load sharing results in unequal transient load sharing between grid forming units, it achieves better transient response upon a disturbance.
This optimal response is the reason why none other alternatives have been investigated for the control structure of the grid forming inverter. The most common alternative is 'emulating' the behavior of a synchronous generator with the inverter's control. Popular concepts in this direction are the VIrtual Synchronous MAchine (VISMA) [107], the Synchronverter concept [108] and the principle of integral droop control [109] with the main objective of creating virtual inertia for the grid forming inverter. It is highly accepted that inertia has played a significant role over the past century in the stability of any power system. However, with the evolution of state of the art and the introduction of new components, the character of power systems can be altered and improved, by utilizing the benefits of each component. Therefore, it is our objective to take advantage of the rapid response of a grid forming inverter in case of step load changes, or short circuits and not artificially turn it to a slower and less vigorous component. Moreover, the lack of short circuit current provision of the inverter, its inherent disadvantage compared to a synchronous generator, cannot be solved with these concepts. It is also demonstrated in [110] that when in parallel with synchronous generators, the grid forming control concept presented in chapter 3 results in a **better frequency & voltage response** in case of a step load change, compared with the synchronverter control concept. Therefore, the guideline for this work is to fully utilize the benefits of employing such a grid forming inverter to a hybrid microgrid, while ensuring grid voltage and frequency stability.

Impact of droop gains on transient load sharing

Transient load sharing is dependent on the different time constants of grid forming units. It is also dependent on the P/f droop characteristic selected. This impact is demonstrated in this section by repeating the previous test scenario

with a modified k_p value, the P/f droop gain. Since the focus of transient load sharing is not reactive power sharing, the Q/V droop gain k_q is kept constant throughout this test. The value of the parameter k_p in the previous test scenario was 0.05 Hz/MW (as given in Table A.11) and is modified from a minimum of $k_p = 0.012$ Hz/MW to a maximum of $k_p = 0.12$ Hz/MW for the synchronous generator, with the droop gain for the grid forming inverter being altered respectively to maintain proportional power sharing. The initial k_p was selected as an optimum value to achieve transient load sharing of short duration and no subsynchronous oscillations. The limits for this parameter regarding system stability are further explained in this section.
By drastically decreasing the droop gain it is expected that the transient load sharing will deteriorate. Decreasing a droop gain inherently leads to the 'relaxation' of the interconnection between generators. Therefore, after a disturbance the transient response will be prolonged and in our case the unequal power sharing between the two generators will be extended. This is verified from Fig. 5.5a, where the new steady state is not reached within 10 seconds after the load step change. Furthermore, oscillations rise up right after the disturbance. The droop gain has been decreased beyond realistic limits and the generators coupling is no longer viable for stable operation. On the other hand, one would expect

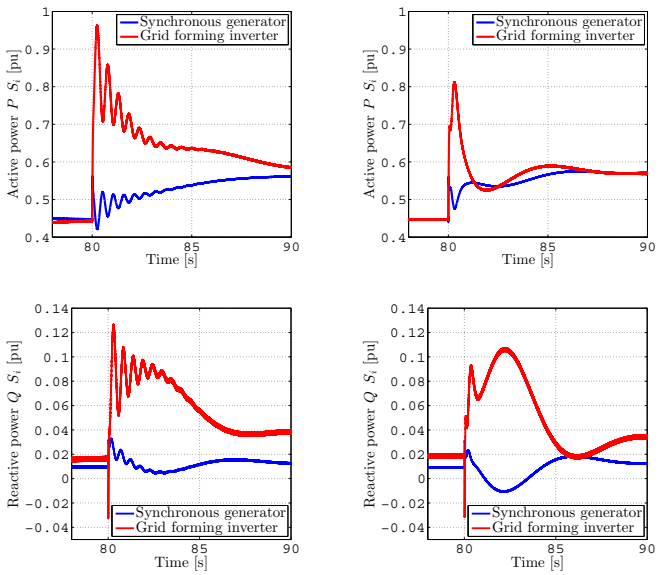

(a) with $k_p = 0.012$ Hz/MW (b) with $k_p = 0.12$ Hz/MW

Fig. 5.5: Impact of droop gain selection on transient load sharing

that increasing the droop gain might lead to transient load sharing of reduced duration. The peak active power is indeed reduced, compared to Fig. 5.3a, but the duration of the transient phenomenon is not reduced. Furthermore, during transient load sharing, at $t = 82$ seconds, the output active power of the grid forming inverter drops lower than the synchronous generator's output. A further low frequency oscillation is therefore introduced, which is not a desired phenomenon for the system. Increasing the droop gain beyond that point would only lead to increased low frequency oscillations and not to optimized transient response.
In summary, it has been demonstrated that droop gains influence the intensity of transient load sharing. Severe oscillations occur if the droop gains are strongly reduced and on the other hand further increasing them can deteriorate the transient response of the grid forming units.

Non-linear transient load sharing

The first scenario is repeated to examine the robustness of droop controlled distributed generators in the presence of non-linear loads. The passive load is replaced by an ohmic load connected through a 3-phase diode bridge to the common bus bar of the two generators, as shown in Fig. 5.6. The power of the non-linear load is selected close to the initial step load change, to ease the comparison between both cases. In Fig. 5.7 the transient response of the two-

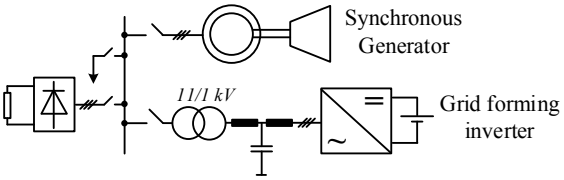

Fig. 5.6: Hybrid microgrid with non linear load

generators system of Fig. 5.6 is depicted. The step change of the non-linear load introduces a significal amount of harmonics, as it can be observed in Fig. 5.7c & 5.7d. It is also evident from Fig. 5.7a that the synchronous generator is loaded with more harmonics than the grid forming inverter which has a faster current control loop that can minimize the influence of the harmonics close to the grid frequency induced from the diode bridge. In Fig. 5.7b the frequency characteristic of each generator is depicted, with both of them remaining unaffected from the non-linearities, opposite to the PLL frequency, which appears with a ripple. The PCC voltage along with the current that the non-linear load absorbs are shown in Fig. 5.7e & 5.7f. The PCC voltage is distorted, since there

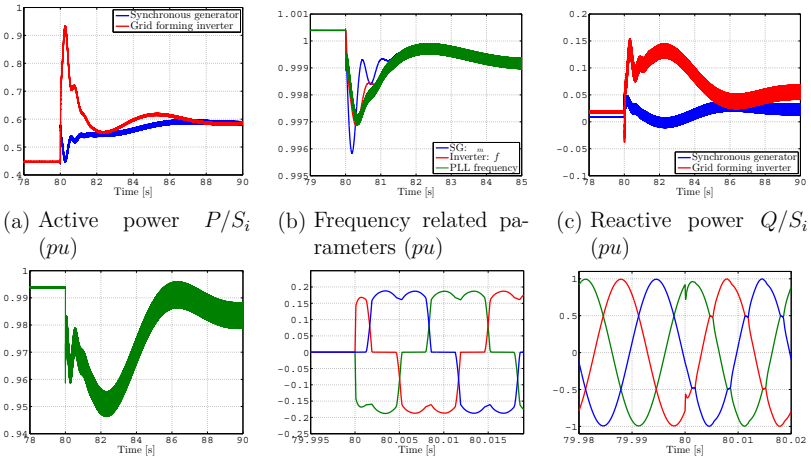

(a) Active power P/S_i (pu)

(b) Frequency related parameters (pu)

(c) Reactive power Q/S_i (pu)

(d) Voltage amplitude (pu)

(e) Non-linear load current (pu)

(f) 3phase bus voltage (pu)

Fig. 5.7: Load sharing upon a step change of a non linear load

is no filter connecting the non-linear load to the rest of the microgrid. The base unit for the load current shown in Fig. 5.7e is chosen to be the base current of the synchronous generator.

Transient load sharing induced by a grid feeding unit

In all previous test scenarios the load has been modeled as a passive impedance connected directly to the microgrid, or through a three phase diode bridge. To demonstrate that transient load sharing occurs independent of the type of load, a grid feeding inverter is connected to the microgrid, as shown in Fig. 5.8. The

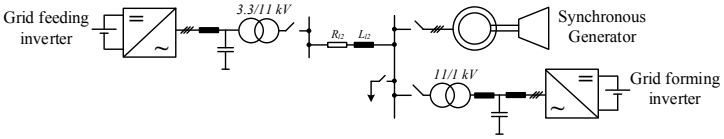

Fig. 5.8: Hybrid microgrid with grid forming and feeding inverter

grid feeding inverter is operated in PQ mode with an ideal DC voltage source at its input. Its rated power is selected at $S_{GFe} = 5MVA$ and at $t = 80$ seconds a step change occurs in its active power reference, from 0 to 0.24 pu [3]. All

[3]The positive setpoint corresponds to power injection from the grid feeding inverter to the microgrid.

further parameters are given in Table A.12. The step change is selected in that

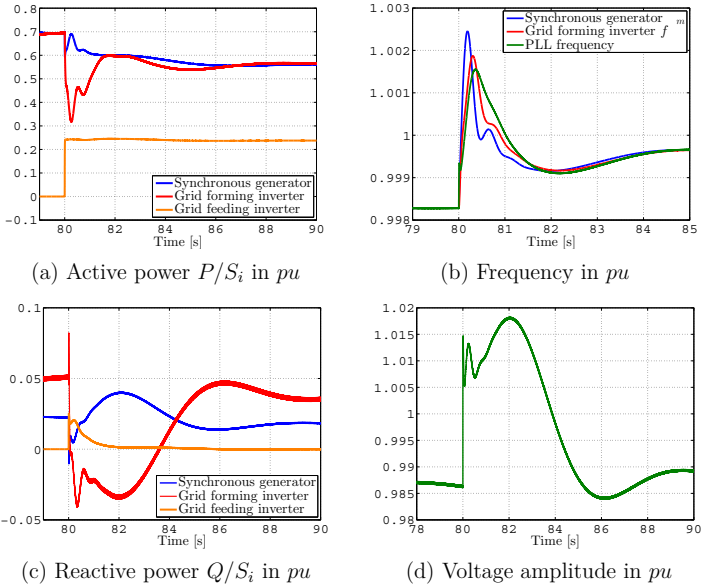

(a) Active power P/S_i in *pu*

(b) Frequency in *pu*

(c) Reactive power Q/S_i in *pu*

(d) Voltage amplitude in *pu*

Fig. 5.9: Transient load sharing caused by grid feeding inverter

range to induce a disturbance similar to the step load change of the previous sections. As soon as the step change occurs, both grid forming units should reduce their output, since the grid feeding inverter is injecting power to the grid and overtakes a part of the load. The grid feeding inverter can be also considered as a 'negative' load. The grid forming inverter reacts once more faster than the synchronous generator, reducing rapidly its output active power. A reverse transient load sharing is observed in Fig. 5.9a with the synchronous generator following the step change with a delay of a few seconds. The frequency of the microgrid is rising, since the load that corresponds to each generator is reduced. The power shift that the grid feeding inverter induces results in two negative effects, namely voltage rise of the common bus and reactive power exchange between the grid forming units. For almost 4 seconds (80-84 seconds) the two grid forming units exchange reactive power, which is an unwanted transient phenomenon. However, this is expected in case of severe transient disturbances such as step load changes. This reactive power exchange could be further reduced by increasing the gain for the reactive power/voltage droop characteristic on the expense of higher voltage sensitivity during transients. The consequences of altering the droop gain to the system has already been demonstrated for the active power/frequency droop characteristic and are not further investigated for the complementary droop curve.

Comparing the results of this subsection (Figs. 5.9a, 5.9b and 5.9d) with the results of the first step load change (Figs. 5.3a, 5.3b and 5.4b) the characterization of the grid feeding inverter as a negative load can be justified. It is demonstrated that active power, frequency and voltage show an almost reverse transient response, identical to load disconnection.

5.2.1 Influence of grid impedance on transient load sharing

In the case of more than one grid forming inverters working in parallel with a synchronous generator the question rises: which unit experiences the most severe transient loading conditions. A hybrid microgrid is once more formed to investigate the effect that the inverter's rated power has on the transient load sharing. The microgrid is depicted in Fig. 5.11a. Three distributed generators are present, all connected to the same voltage bus. The inverters are connected as in the previous scenarios through a step-up transformer to the rest of the microgrid. The DC-link of each inverter is once more modeled with an ideal voltage source, since its dynamics do not influence the inverter's response after a step load change. The rated power for the first grid forming inverter ($GFoI_1$)

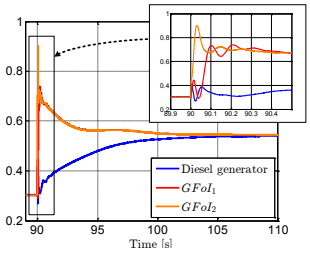

(a) Active power P/S_i in pu

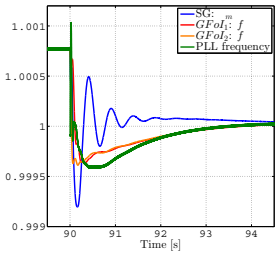

(b) Frequency related parameters in pu

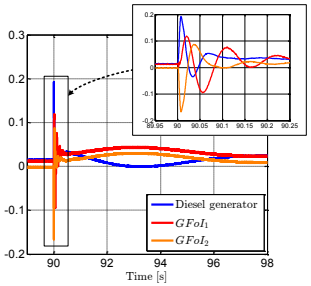

(c) Reactive power Q/S_i in pu

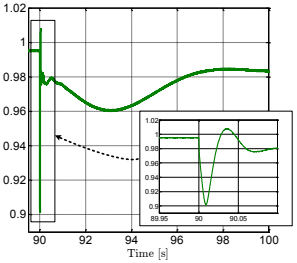

(d) Voltage amplitude in pu

Fig. 5.10: Transient load sharing results

and the second grid forming inverter ($GFoI_2$) are selected at $S_{GFo1} = 2MVA$ and $S_{GFo2} = 6.75MVA$ respectively. The droop gains for all three distributed generators are given in Tables A.10 & A.11 and the power of the load step change is equal to $P_{load} = 5$ MW. It would be expected that the inverter with the lower rated power experiences the most severe transient load sharing. However, this is not the case as seen in Fig. 5.10a. The inverter with the higher rated power, $GFoI_2$, namely 6.75 MVA, overtakes the majority of the load for the first grid periods (~ 80 ms) after the load change. The two grid forming inverters synchronize faster than the diesel generator that follows afterwards. The frequency drop is minimal (less than 0.0015 pu) and the mechanical speed of the synchronous generator recovers within 15 seconds after the step load change. Reactive power exchange between generators with a duration of almost two grid periods is observed in Fig. 5.10c. As mentioned in the previous test scenario, this short-time power exchange cannot be avoided in such cases of severe transient disturbances. Although the step load change equals to almost 30 % of the installed generators capacity, the induced voltage drop is less than 10 %, as shown in Fig. 5.10d. The influence that the grid forming inverters have on the stiffness of the microgrid can be validated through this minimal voltage decline.
Due to the absence of inertia, the inverters compared to the synchronous generator are working as ideal droop-controlled voltage sources and their models could be simplified and idealized as in Fig. 5.11b. The most influencing factor for the load sharing between ideal sources is their grid connecting impedance. The grid impedance in our case is mainly inductive, since it includes leakage inductance of transformers, and an additional inductance as part of an LCL filter, if present. The ohmic part of the impedances can be neglected, since it amounts to less than 2% of the inductive part.
Choosing as base quantities the parameters of the synchronous generator, it can be calculated that the connecting impedances of the grid forming inverters have a ratio of $Z_1/Z_2 \approx 8.9$. It has been shown in Fig. 2.10 & 2.11 that by increas-

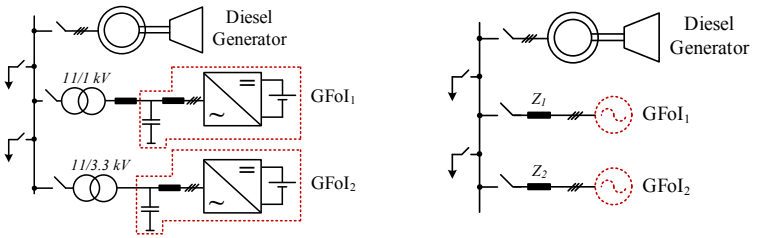

(a) Full scale microgrid (b) Idealized depiction of microgrid

Fig. 5.11: Hybrid microgrids for transient load sharing considerations

ing the length of a distribution line connecting two droop-controlled generators, the stability margin for the droop gains increases. In other words, paralleled

generators working 'closer' to each other have an increased coupling and require lower droop gains. The line length can be interpreted as the grid connecting impedance of each generator: The smaller the grid impedance, the bigger the interconnection between grid components. That is also valid for the case of transient load sharing. The second grid forming inverter has the shortest electrical connection (grid connecting impedance) to the central load and experiences the most severe transient load sharing.
An option to solve this unequal transient load sharing among inverters would be to design a virtual impedance that creates artificial voltage drops and matches the grid impedances. However, in this way not only the reactive power sharing is deteriorated, as well as equal impedances can never be obtained due to the fact that the loads are also distributed and not central, as in the real time simulation test scenario above. The guideline should be to make sure that the grid impedances of such grid forming inverters working in parallel do not have great deviations that could shortly overload one of the distributed generators. Designing components depending on other grid participants should be avoided. It is an important reliability factor of any power system the ability to design each grid component independent of the co-existence of other grid components.

5.2.2 Oscillations due to transient load sharing

Analyzing the results from the previous sections, a rational questions rises: can the transient load sharing be problematic for inverter-based distributed generators? In case of severe step load changes, the inverter cannot provide all the necessary power due to the activation of the current limitation component. It should be further investigated if the current limiting component during transient load sharing results in system instability.

5.2.2.1 Activation of current limitation

In the following section, three severe step load changes in the system of Fig. 4.1 occur to activate the current limitation of the grid forming inverter. The current limiting method selected for this test scenario is the amplitude limitation and will be further analyzed and compared with other current limiting methods in chapter 6. The rated power of the grid forming inverter is selected at $S_{inv} = 2MVA$. The step load changes are $P = 2,\ 2.25$ and 2.5 MW. In the following figures with increased load power the line fading increases.

The first observation is that the inverter's current is in all three cases limited to the pre-selected value of 1.1 pu and the inverter's components are effectively protected from over-currents. As the power of the step load change increases, the inverter remains in its limited value longer, as shown in Fig. 5.12b and the intensity of the oscillations increases, as seen in Fig. 5.12a. The active power, depicted in 5.12a, appears as 'clipped' since the current is shortly limited and

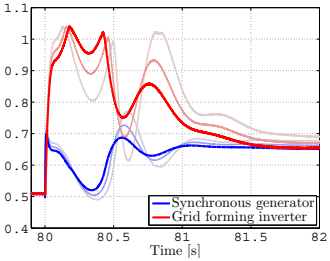

(a) Active power P/S_i in pu

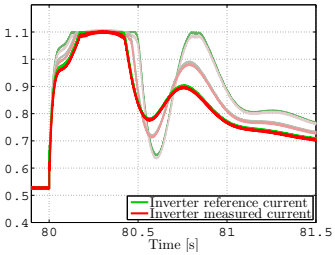

(b) Inverter-side current in pu

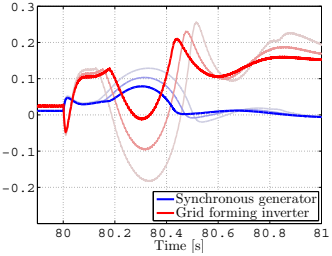

(c) Reactive power Q/S_i in pu

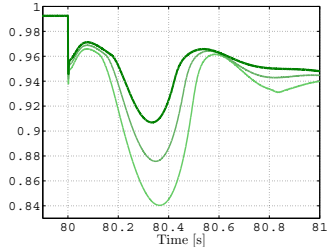

(d) PCC voltage amplitude in pu

Fig. 5.12: Transient load sharing with current limiting

the active power cannot be further increased. Since the current amplitude is limited to 1.1 pu, and the reactive power that the grid forming inverter delivers to the grid is close to 0.15 pu, the active power does not reach the maximum value of 1.1 pu. The reactive power exchange between generators deteriorates with increased load change, as shown in Fig. 5.12c. The synchronous generator is forced to compensate the inability of the inverter to provide excess reactive power. A similar deterioration can be observed in the voltage response of the system. Although right after the step load change the inverter manages to deliver a minimal voltage drop, when the current limitation is activated the voltage drop icreases, as shown in Fig. 5.12d.
In this test scenario, if the step load change exceeds the value of $P = 4\ MW$, the system becomes unstable.

5.2.2.2 Frequency reference switching

A control method is proposed in this work to minimize the instabilities that occur during severe step load changes. When the current limitation of the inverter is activated, the grid frequency instead of the frequency setpoint from droop control is used as a reference. The implementation concept is shown in Fig. 5.13. As soon as the current crosses over a designated threshold value, I_{th},

the frequency reference calculated changes to the one measured from the PLL. This modification is applied only for the parallel operation of the grid forming

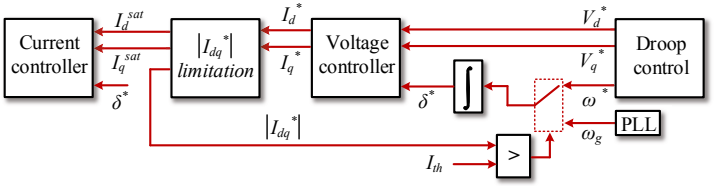

Fig. 5.13: Frequency reference switching concept

inverter with a synchronous generator. In standalone mode, the transient load sharing does not appear, since the inverter is the only grid forming unit of the microgrid.

In this way the two generators are eased to synchronize faster, since the frequency reference for the inverter is decoupled from the inactive voltage controller and tries to follow the grid frequency imposed from the diesel generator. Fig. 5.14 shows the results of the implementation, compared to the operation without the proposed control method. The threshold value I_{th} in this test scenario is selected equal to 1 pu. The step load change is $P = 3$ MW and with faded lines are shown the results without frequency reference switching. It has to be mentioned that such a severe load change of almost 40% of the power capacity of all grid generators is rare and resembles an unrealistic case scenario. It is shown that with the implementation of frequency reference switching for the same step change the current remains for a shorter period of time in the limited value, and the oscillations significantly decrease in amplitude and duration. Observing Fig. 5.14c, the effect that the oscillations have on the frequency measured by the inverter's PLL can be analyzed. The PLL frequency is not directly coupled with the inverter's voltage controller behavior, and linking the frequency reference to it minimizes the inability of the inverter to control its output voltage during active current limitation. It can be seen however that the oscillations remain even with the implementation of frequency reference switching. Instabilities during severe load changes can in a similar manner occur during the parallel operation of synchronous generators, according to the voltage angle-active power stability curve [10].

An alternative to the proposed frequency switching method could be the implementation of a mixed virtual impedance to improve transient load sharing, as in [103]. However, the maximum current amplitude is in that case equal to 1.5 pu and not close to the rated value and, since the virtual impedance is rated for the worst case scenario, an increased voltage drop is produced. In the case the limit is close to the rated current, e.g. 1.1 pu, the activation of a transient impedance could lead to instabilities, since the gap between limiter's activation

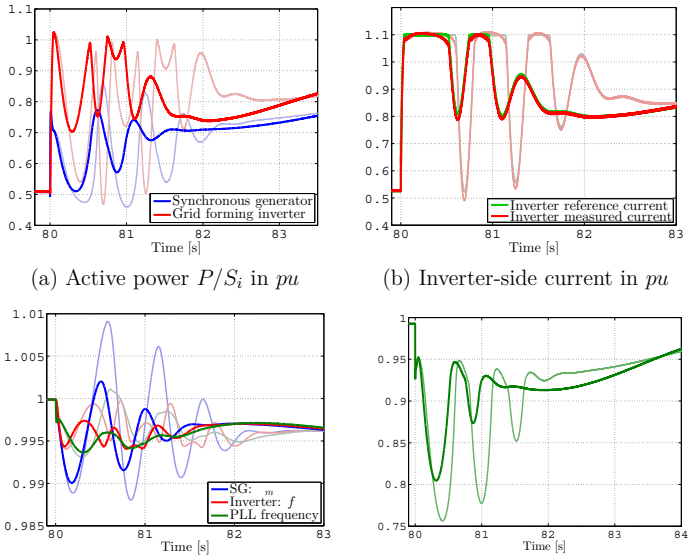

(a) Active power P/S_i in pu

(b) Inverter-side current in pu

(c) Frequency (pu)

(d) PCC voltage amplitude in pu

Fig. 5.14: Improving transient load sharing

and maximum allowed current is minimal. Therefore, the only possible alternative is the current amplitude limitation equipped with a frequency switching control concept. The aforementioned transient virtual impedance is further compared with the current amplitude limitation in the case of severe faults cases in chapter 6.

5.3 SoC-Adaptive droop control

The focus in the previous sections was the transient response of different hybrid microgrid configurations after a disturbance. That could be the synchronisation of a generator, or a load change, realized in its worst possible form, as a step change. It has been demonstrated in all above cases that both voltage and frequency show a stable response. All previous investigations have been dealing only with each generator's individual control structure and the identical primary control structure which was realized through droop characteristics. Looking however one step further in the time axis, the secondary control [111] is responsible for restoring the microgrid voltage and frequency to their nominal values in a time span of 10-15 minutes [44], so that there are no large deviations for the consumers. For the voltage the boundaries are typically ± 10% [112] and

for the frequency is for islanded grids normally lower than ± 1% [113]. The secondary control requires communication means between generators, since it alters the individual droop control of each generator, to influence the steady state load sharing according to energy market or cost requirements. Communication requirements can easily expand the affordable and technical feasible region when considering complex grid configurations, with dispersed generation units that also depend on weather prognosis and do not possess the characteristics of large power plants. The overall hierarchical control structure of power systems with primary, secondary, and tertiary control is based on the characteristics of 'outdated' large power plants.
As far as communication is concerned, approaches exist that integrate rapid communication between generators for the implementation of not only secondary control, as well as primary control [114]. The grid integration of battery systems is linked with generators communication and short-term balancing of energy consumption and generation. In microgrids, communication agents could be utilized to rapidly enhance the power distribution exploiting storage availability [115]. The overall concept of smart grids is, if one may say, based on the evolution of communication means, and the rapid information interchange between generators. These concepts however do tend to deviate from realistic approaches that are also economically affordable. In this work the focus lies on providing reliable and as far as possible **autonomous** solutions for practically implementable hybrid microgrids. In this section more specifically, the communication means within a hybrid microgrid are minimized, incorporating secondary within primary control, only based on local measurements of each generator. This could be a very useful approach in case communication fails, comparable to designing the distribution lines of a power system taking into consideration the 'N-1 criterion' [116]: any type of grid should be fully operable in case one of its distribution lines displays a fault in its functionality.

5.3.1 Concept presentation and implementation

The concept of SoC-Adaptive droop control is to manipulate the active power/frequency (P/f) droop setpoints depending on the state of charge (SoC) of the battery pack connected at the input of the grid forming inverter [117]. Optimizing droop control on the basis of the information of the SoC batteries has been presented in [118]. A comparable approach has been introduced for a multi terminal DC-grid coupled system in [119] but cannot be applied for an islanded AC-microgrid with frequency supervision. In [120] the battery SoC is also used to modify droop control, but this modification is limited to the optimization of frequency regulation and the assessment of its stability.
The idea is quite straight forward: The grid forming inverter that connects the battery, or the battery with a renewable energy source, to the grid adjusts its setpoints based on the SoC of the battery connected to the DC-link, as shown in Fig. 5.15a. In other words, the droop setpoints of any distributed generator are

'adapted' based on the state of charge of its battery pack. The second idea of this algorithm, shown in Fig. 5.15b, is to switch to a variation of PQ grid feeding mode, when grid conditions and SoC level favor it. By grid conditions the grid frequency is implied. The limit Δf is selected arbitrarily at $\pm 0.015 Hz$. When both frequency and SoC is within limits, a controller is activated, that allows the active power setpoint to be brought to 1 or -1, depending on the conditions. The power output is still altered through droop control and grid forming mode.

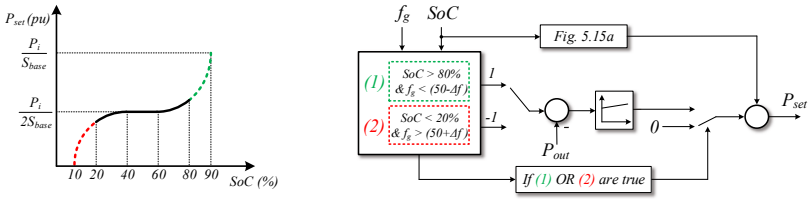

(a) P_{set} coupled with SoC (b) Implementation

Fig. 5.15: SoC-adaptive droop control concept

An alternative would be to switch the whole control mode in PQ grid feeding mode, with $P_{out} = 1/-1$ and $Q_{out} = 0$. In this way however, in case of a fault the inverter should switch back to grid forming mode to support the grid with non-fixed PQ setpoints. Therefore, the variation of PQ-grid feeding mode through P/f droop setpoint modification is introduced.

5.3.2 Case studies

Test scenarios are conducted to analyze the performance of the proposed SoC-Adaptive droop control. The main parameters of the test scenarios are given in Fig. 5.16 & 5.20 and the models presented in chapter 3 are utilized. The individual parameters of the synchronous generator as well as the grid inverters are given in Table A.3 & A.6 respectively. One full day profile for the renewable energy based generators is scaled to 240 seconds of real time simulation, and the battery capacity is also scaled respectively. As previously already mentioned, cost considerations are not included in this work, so minimizing the battery capacity is not the focus of this algorithm. The microgrid is considered in a steady state point when the test scenarios start. The load is selected at a different level for the microgrids with central or local storage in order to activate all operating regions of the proposed algorithm. The battery capacity is not the focus of this investigation and differentiates between the two scenarios so that the operating regions of the algorithm could be activated. Two different scenarios are performed for two microgrid topologies, based on local and central storage

respectively. In the first microgrid, shown in Fig. 5.16 the battery packs are distributed and located in the DC-link of each renewable energy source. The aim of this selection is not to compare the microgrid topologies as far as storage position is concerned, but to evaluate the performance of the proposed control algorithm in various grid topologies. Furthermore, as mentioned in chapter 1, the time focus exceeds the time constants of power electronic components as well as the DC-link voltage dynamics of inverter-interfaced generators. The input sources that resemble renewable energy sources are modeled as ideal current sources following a generation profile. Average value based models for the power electronic converters can be utilized in these scenarios.

5.3.2.1 Decentralized storage

The evaluation of the proposed strategy starts from a grid topology based on decentralized storage means. The meshed grid of Fig. 5.16 includes battery packs in the DC-link of each distributed generator with a renewable energy source as input. That would be the ideal grid-friendly structure, where each generator is working in a grid forming mode, actively supporting the grid upon each load change. It has been demonstrated in the first load sharing test scenario (subsection 5.2), that grid forming inverters are grid-friendly generators that control their output voltage and frequency and react faster and more efficient that synchronous generators. Therefore, it is reasonable to consider that both grid inverters of Fig. 5.16 are working in grid forming mode. The initial P/f droop setpoints and gains are selected as explained in Section 5.1, so that the distributed generators share the grid load according to their rated power. The droop gains remain unaffected during the implementation of SoC-Adaptive droop control.

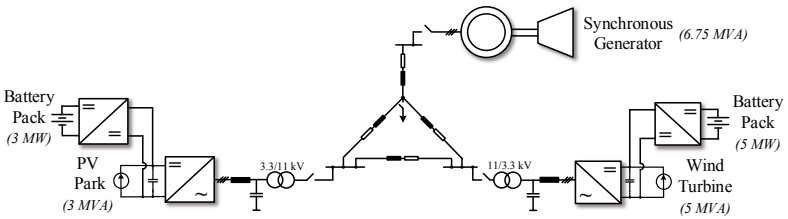

Fig. 5.16: Hybrid microgrid with decentralized storage

Arbitrary profiles for the renewable energy sources are selected for this scenario, as shown in Fig. 5.17. The wind turbine (WT) profile is different for each scenario to activate charging and discharging control modes of the battery pack connected in parallel to its DC-link. The PV profile remains constant and the capacity of the battery connected in parallel is over-sized. In this way, the

performance of only one generator applying SoC-adaptive droop control can be evaluated. In a more realistic test scenario the combination of control responses of multiple generators applying SoC-Adaptive droop control could be further investigated. In Fig. 5.18 the operation of the algorithm is shown for a case where

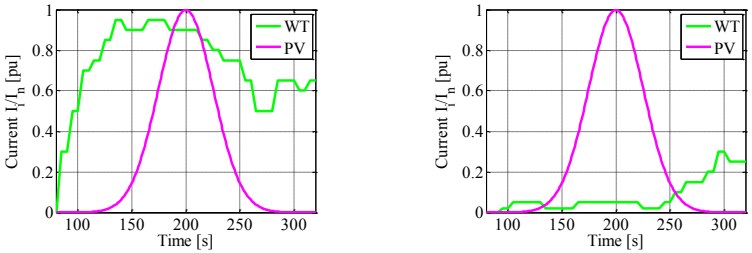

(a) For activation of deep discharging (b) For activation of deep charging

Fig. 5.17: RES profiles used for algorithm evaluation

the battery of the WT is almost empty. Despite the fact that the PV provides almost its rated power, as it can be seen from Fig. 5.18c, the SoC of its battery pack remains within the boundaries $40-60\%$ because its capacity is oversized. The fact that SoC-Adaptive droop control is not activated for the PV park can be deduced also from Fig. 5.18a, where the diesel generator shares during the whole real time simulation scenario the load proportionally with the PV park. The significant points for the algorithm are highlighted in Fig. 5.18c with vertical dashed lines, to better comprehend the algorithm steps. At point (1) the SoC

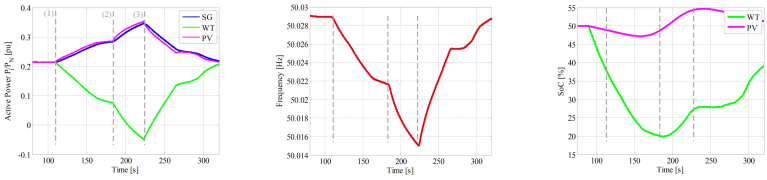

(a) Active power in pu (b) Frequency in Hz (c) SoC in %

Fig. 5.18: Microgrid with local storage: Charging scenario

of the wind turbine battery goes below 40 %, forcing the wind-battery-system to feed the grid with less active power. That is the case of minimal incoming energy from the wind turbine to the DC-link of its grid forming inverter. The droop setpoint is reduced and, as seen in Fig. 5.18a, the wind turbine is no longer sharing the load with the other distributed generators. At point (2) the SoC reaches a value below 20% with an output active power of less than 0.1 pu. At that point, the modified grid forming mode starts, where the battery tries

to be charged from the grid, if the grid frequency is in an allowed region. That continues until point (3), when the frequency reaches its upper limit ($50+0.015$ Hz). Within the region between operation points (2) & (3), the grid forming inverter connecting the wind-turbine-battery system starts to absorb energy from the rest of the microgrid to charge its battery pack. That implies that, because the load is relatively small and the frequency is in the allowed region, the diesel generator and the photovoltaic park increase their output power to feed the battery of the wind turbine. In this way, power is shifted from one battery pack to another, since the grid conditions allow it. That could prove as a useful tool against load and energy shedding, since the batteries of the grid are always self-balancing their SoC. Moreover, the practice of increasing the output power of the diesel generator in lower loads could significantly improve its fuel efficiency [121], therefore reducing the total costs.
In Fig. 5.19c the reverse case is examined, where due to the excess of wind energy, the distributed generator based on the wind-turbine-battery system increases its output power to the microgrid. Once more, all generators start from identical setpoints and share the load equally, depending on their rated power, and deviations can only be seen in the wind turbine based system, which experiences the radical change in its battery SoC. The wind-turbine-battery system is allowed to increase its output power only because, as seen from Fig. 5.19b, the frequency is within the permissible region ($50-0.015$ Hz). As soon as the frequency reaches its lower limit for the deactivation of the SoC-Adaptive droop control, around $t=210$ seconds, the P/f droop control setpoint begins its decreasing course, so that the load can in the end be again equally shared by all generators.

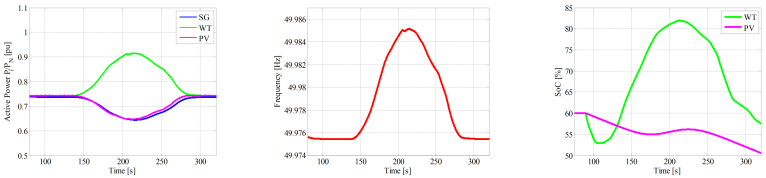

(a) Active power in pu (b) Frequency in Hz (c) SoC in %

Fig. 5.19: Microgrid with local storage: Discharging scenario

An interesting observation from Fig. 5.18a & Fig. 5.19a is that, once the wind turbine changes rapidly its delivered power, the photovoltaic park follows faster than the synchronous generator. This is due to time scaling necessary for the test scenarios. The inertia of the diesel generator remains quite high, therefore it cannot follow precisely the changes in the frequency and active power in a few seconds.

5.3.2.2 Central storage

The hybrid microgrid of Fig. 5.20 is based on a central battery storage system. The grid topology is once more meshed, and the battery-based distributed generator is connected to the same voltage bus as the diesel generator. This selection is defined by the state of the art of modern power systems, where the batteries are typically placed close to other generators to enable easy communication and enhance system controllability. The RES-based distributed generators are connected to the rest of the microgrid through grid feeding inverters. The generation profiles in this scenario are not separately shown, since they can be indirectly read from the active power output of the inverters.

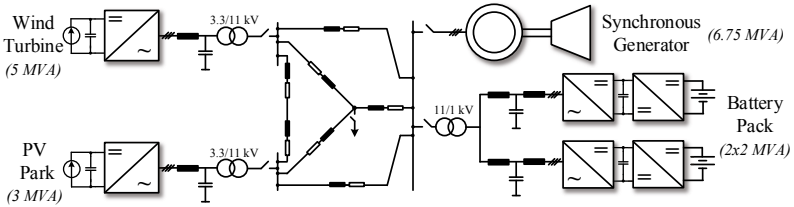

Fig. 5.20: Hybrid microgrid with central storage

In Fig. 5.21c the charging scenario is shown. The central battery pack is almost empty (SoC<20%) and the grid frequency is in the allowed region, $f_g > 50 + 0.015$ Hz. Therefore, the battery pack is charged faster from the microgrid. The operation only with the $SoC - P_{set}$ look-up table, without the extra feeding mode controller is also shown with a more transparent color. In this way the effect that the additional controller has can be seen in the real time simulation results. In Fig. 5.22 the reverse test scenario is once more shown. The SoC of the central

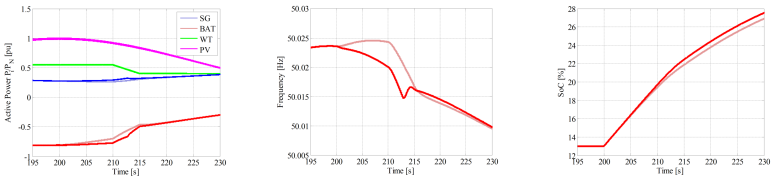

(a) Active power in pu (b) Frequency in Hz (c) SoC in %

Fig. 5.21: Microgrid with central storage: Charging scenario

battery pack is above 80 % in combination with the frequency being in the allowed area, and the battery is discharging faster for a short period of time. The peaks that are observed in both cases in the frequency are due to time scaling

and would not appear if the test scenario would be conducted in real time basis. The impact of this algorithm on the frequency can be observed in Fig. 5.22b.

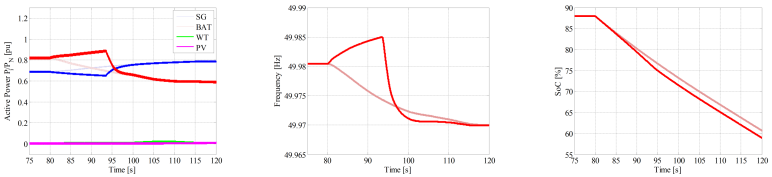

(a) Active power in pu (b) Frequency in Hz (c) SoC in %

Fig. 5.22: Microgrid with central storage: Discharging scenario

At $t = 80$ seconds, the proposed algorithm starts to discharge the battery faster, bringing the frequency closer to its tolerance band of 50 ± 0.015 Hz. That is a further advantage of the proposed algorithm. In case of over- (or under-) frequency, provided that there is also a need (or excess) of energy from the batteries, the frequency is brought back closer to its nominal value. In other words, the frequency state is exploited as a communication means for more reliable power distribution.

5.3.3 Evaluation and further development of proposed algorithm

The structure of nowadays grids moves towards increased used of communication. Secondary and tertiary control are prevailing and electrical energy market defines the long-term power flow. However, with the penetration of renewable energy sources storage is needed and should be integrated to the existing grid. With the increased penetration of storage means the market characteristics should evolve and secondary control becomes more and more complicated. To overcome this problem, a basic algorithm is proposed which does not rely on communication. With the use of SoC-Adaptive droop control the autonomy of the grid is increased, since each distributed generator is supporting the grid and self-adjusting its power flow. The inherent drawbacks of the algorithm are evident:

- Dimensioning the capacity of battery systems: The guideline for the design should be grid reliability. Therefore, each battery pack should be designed according to all other storage means present in the grid, so that the load can be efficiently distributed.
- Long-term planning of power distribution: Constraints should be further introduced to facilitate the long-term successful implementation of the algorithm in a well-defined microgrid concerning load forecast and generation capacity.

- The proposed algorithm cannot be combined with a secondary grid control. This strategy is based on droop setpoints planning according also to grid frequency deviations. As soon as these deviations disappear, or the identical setpoints for all generators are altered, the algorithm can no longer serve its purpose.

Furthermore, the algorithm should be further investigated in combination with efficient battery charging and discharging methods. The strategy proposed in this section can be characterized as a grid-friendly control algorithm. For cost reduction, the factors that reduce battery lifetime and durability should also be taken into consideration.

5.4 Load sharing conclusions

In this chapter different aspects of load sharing in microgrids with various type of distributed generators are analyzed. The fundamentals of implementing droop control for grid forming units with various rated powers in parallel are presented. The problematic of transient load sharing between synchronous generators and grid forming inverters is further introduced. The influence that droop gains, load type and grid impedance have on the severity of transient load sharing is investigated. To overcome the instabilities that may occur during severe transient load sharing cases the concept of frequency switching is proposed. In this way, the grid forming inverter follows the transient response of the synchronous generator when its current is limited. Finally, a grid-friendly algorithm for grid forming units that connect battery packs is proposed to support the autonomy of distribution generation. Through this algorithm, each distributed generator self-adjusts the power exchange with the microgrid, based on the measured frequency deviation and the state of charge of its battery pack.

6 Short circuit strategy

In the previous chapters the focus was on synchronization concepts and load sharing considerations which are all not classified as severe transient phenomena. The most challenging point for the smooth operation of any electrical grid is dealing with faults. The goal of this chapter is twofold:

- to document the transient response of medium voltage microgrids during and after faults.
- to introduce the necessary control modifications for each distributed generator to support the microgrid during these severe transients.

These control modifications are classified as a short circuit strategy. The attributes and objectives of this strategy follow these guidelines:

- It has become evident in this work that the focus is the inverter-based generators, as main components of (hybrid) microgrids. We have seen that the inverters in grid-forming or grid-feeding mode can follow the control references and adapt the behavior that any grid operator demands, which is a basic advantage in their employment in any power systems. Their major disadvantage however is their inherent disability to produce overcurrent needed for fault detection and isolation. A basic attribute of the developed short circuit strategy is that it is based on the traditional over-current protection scheme. Therefore, the short circuit current should be maximized and inverter's oversizing is investigated.
- Autonomy: In this work no solutions are considered based on communication. As in chapter 2 explained, there are several industry products that are based on central controllers. This is unavoidable for optimal energy planning and operational management, since different parameters and states of generators are needed. In this work, similar to chapter 5, the worst-case scenario is considered, when communication is not available or possible. Moreover, to react upon a fault, a robust solution should be independent of communication delays that could be up to a few grid periods.
- Modularity: Since the strategy is not based on a central controller, the grid topology can be expanded or reduced and that should not alter the individual controller of each inverter-interfaced distributed generator.

6.1 Protection means

Before looking into details the control structure of each distributed generator, a short presentation of the protection means that prevail in modern power systems should be performed. The protection means are based on the detection of over-current and isolating the distribution lines involved in the fault. Typical overcurrent-tripping time characteristics for line circuit breakers, are shown in Fig. 6.1 ([122]). The four different types (A,B,C,D) depend on the application conditions of the breaker and overloading demands. The different characteristics also aid in the realization of selective protection and assisting a rapid fault detection [122]. The form of the characteristic remains the same, independent

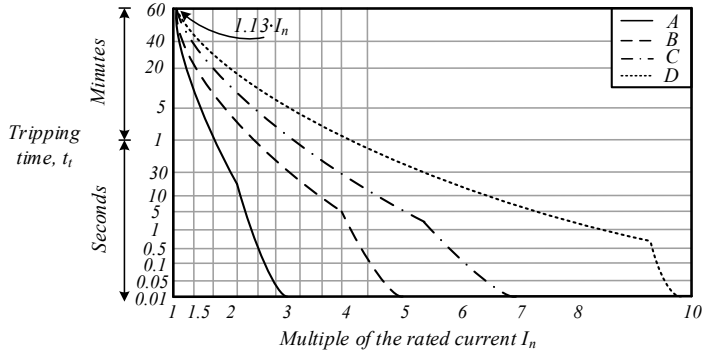

Fig. 6.1: Typical tripping characteristics of circuit breakers

of whether the protection device is based on a fuse, a circuit breaker or relay. These characteristics do always include also a tolerance band, that eases the implementation and tuning of each protection means based on the electrical installation that needs to be protected. The limits of these tolerance bands are the case of e.g. conventional tripping and non-tripping current for line circuit breakers. Observing Fig. 6.1, it is obvious that difficulties rise in the installation of protection means if inverter-based distributed generators dominate a grid. It is common practice to up-rate the inverter in order to provide maximum support in fault cases, but the uprating is far from enough to cover the values shown in Fig. 6.1. For grid feeding inverters it is standard to oversize up to 1.5 to 2 pu [123], [16], [124] and for grid forming units up to 3-5 pu [16] [125]. Other approaches refer to uprating the inverter to 2 pu independent of the application [126], [127], [128]. Therefore, it is evident that the protection means should get more intelligent, to successfully deal with faults in inverter-dominated grids. Such an intelligent approach would be rapid communication schemes that des-

ignate relays hierarchy for selective protection, to optimize the time needed to identify fault location [129]. Another approach for inverter-dominated grids is to integrate an extra storage system that could provide, for a short period of time, over-currents needed for the fault detection [124], [130]. Selecting and designing a ultra-capacitor based storage system designated for providing fault current in isolated microgrids can be found in [131].
The problematic of developing a short circuit strategy for islanded grids that cannot supply the necessary over-currents has existed before the development of grid inverters. A typical example is isolated on-board grids of ships. In that case, the problem of distinguishing between overloading conditions and faults has appeared, since the diesel generators forming the grid might not provide in all cases sufficient short circuit current. A solution towards utilizing the measured grid admittance during the fault instead of over-currents has been proposed in [132]. However, this approach has limited applicability in inverter-dominated grids, since the measurement is prone to disturbances, and moreover it also requires a specific amount of over-currents from the generators to facilitate the admittance measurement.
The focus of this short circuit strategy is the control structure of the inverter-based distributed generator and how should they react upon the appearance of a fault. As previously mentioned, no approaches are investigated which are based in communication. That could be the case of a master-slave principle, where grid forming inverters working in parallel are properly synchronized and build up a frequency-dependent fraction of the fault current [133]. Since the over-current provision of inverter-based distributed generators is limited, the limits between overloading conditions and fault conditions tend to disappear. Therefore, in such inverter-dominated microgrids, overloading conditions should be avoided. That would be the case of higher inrush currents of transformers or directly-coupled motors with no power electronic interface. The control modifications introduced in this chapter focus only on the generators of the microgrid. A necessary expansion of the proposed strategy is to design the tolerances for protection means and loads accordingly.

6.2 Grid forming inverter

The focus of the short circuit strategy for the grid forming inverter is the current limiting method implemented to protect all inverter's components. The widely implemented cascaded control structure in SRRF presented in chapter 3 is the only control structure implemented in this work. The cascaded multi-loop control structure offers the inherent possibility to insert a current reference limitation between voltage and current control level. This is the main advantage of the grid forming control based on the multi-loop method, opposed to a simple single-loop voltage control. In single loop grid forming structures, the voltage reference should be rapidly reduced to effectively limit the current. That could

be the case of a current supervision concept where the current is decreased proportionally to the over-current [13], [134], or the case of a virtual impedance, a concept that is further analyzed in this work. Alternatives to the SRRF would be to use controllers based on the stationary reference frame or the natural reference frame which rely on proportional-resonant controllers [41]. However, as already mentioned in chapter 3, applying symmetrical components analysis in the SRRF can also deal with unsymmetrical fault conditions. A theoretical explanation of current limiting methods follows, accompanied with real time simulation results that aid on the selection of the most appropriate limiting method [135].

6.2.1 Current limiting methods

There are various methods for current limiting for grid forming inverters. The limitation goal is always to respect the current rating of all inverter components and avoid over-currents during transient phenomena.

6.2.1.1 Current reference saturation

The significant advantage that the control structure of Fig. 3.29 offers is the possibility to directly limit the output current reference of the inverter. The DQ-current components of the currents, since they are DC quantities can be limited through a saturation block. After the saturation of the current reference, the controller ensures that the current will not exceed this maximum value.

Separate saturation of current components The most straight-forward limitation method is the separate saturation of the d- and q-component of the current as shown in Fig. 6.2a. The maximum current components $I_{d_{max}}$ & $I_{q_{max}}$ must be selected in a way so that the maximum current amplitude I_{max} should be at all times lower than the designer's choice. The three parameters are connected according to the following equation:

$$I_{max} = \sqrt{(I_{d_{max}})^2 + (I_{q_{max}})^2} \tag{6.1}$$

It is evident that, in case that only one of the components reaches its maximum value, that does not imply that the current can reach its maximum value. Furthermore, in that case the current references are also shifted to a different angle prior to the saturation. This leads to a mismatch of the desired power factor that the current references impose to the inverter. Both issues of this method are graphically depicted in Fig. 6.2b, where the current reference reaches its maximum value $I_{d_{max}}$ and is saturated.

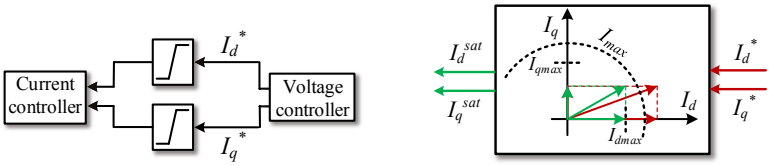

(a) Separate saturation (b) Saturation mismatch

Fig. 6.2: Current components separate limitation

Current amplitude saturation To fully exploit the current rating of the inverter's components, it is desired to develop a method that can limit the current amplitude to the designer's choice. In this way, the two negative aspects explained in the previous paragraph can be tackled. The current reference amplitude $|\bar{I}_{dq}^*|$ and the vector angle δ_{dq} that results from the DQ-components is required for this method:

$$|\bar{I}_{dq}^*| = \sqrt{(I_d^*)^2 + (I_q^*)^2} \tag{6.2}$$

$$\delta_{dq} = \tan^{-1}\left(\frac{I_q^*}{I_d^*}\right) \tag{6.3}$$

The amplitude is then directly limited and the angle is needed for the calculation of the saturated values of each current component, as shown in Fig. 6.3a.

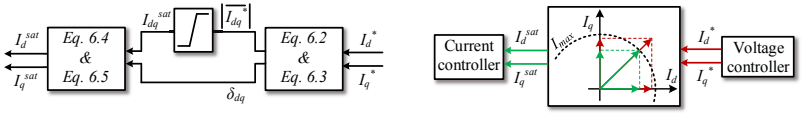

(a) Implementation (b) Vector amplitude saturation

Fig. 6.3: Current amplitude saturation

where:

$$I_d^{sat} = \cos(\delta_{dq}) \cdot I_{dq}^{sat} \tag{6.4}$$

$$I_q^{sat} = \sin(\delta_{dq}) \cdot I_{dq}^{sat} \tag{6.5}$$

An alternative approach for the implementation of Fig. 6.3a is setting a saturated value once the limitation is activated. The current amplitude is calculated and compared with its maximum value. As soon as the limitation is reached, the reference switches to fixed values. The saturated values for each component

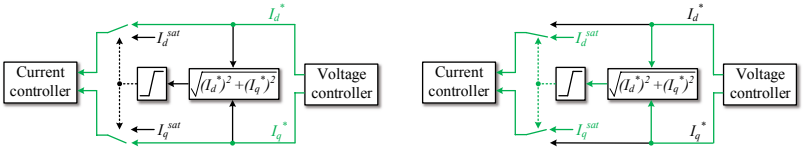

(a) Under normal operation (b) with current limitation activated

Fig. 6.4: Current limitation through saturated values

are given in Eq. 6.6.

$$I_d^{sat} = \frac{I_d^*}{\sqrt{(I_d^*)^2 + (I_q^*)^2}} I_{max} \quad , \quad I_q^{sat} = \frac{I_q^*}{\sqrt{(I_d^*)^2 + (I_q^*)^2}} I_{max} \tag{6.6}$$

This approach of setting saturated values as soon as a limit is reached is common for controllers in the stationary reference frame or the natural reference frame [136], [137] and [127]. In that case the current reference is not a DC quantity and the standard saturation method cannot be implemented. The disadvantage of this method is that switching between signals can lead to instabilities when operating near the boundaries. That means that it is possible to switch back and forth between values during the transient state, that could lead to system instability. This can be identified as controller state 'latching' and could be dealt with trip and reset logic signals that supervise the transition [41]. Since in this work all control structures are implemented in the synchronous rotating reference frame, the direct amplitude saturation of Fig. 6.3 is preferred.

6.2.1.2 Transient virtual impedance

A substitute to the saturation of the current reference would be the implementation of a transient virtual impedance. The concept of virtual impedance is a method of creating an artificial impedance at the output of an inverter through its controller. In other words, it is a way of forcing the inverter's controller to adjust its references as if an additional impedance was present in the circuit. The manipulation of the measured current and (or) voltage is required to built up this virtual impedance.
The virtual impedance principle is well known for optimizing the grid connecting impedance of an inverter, to ease reactive power sharing, or facilitate droop control in ohmic low voltage grids [138], [139]. This fixed virtual impedance implementation will be further named steady state virtual impedance, since it is independent of the grid load. Virtual impedance can however be exploited to achieve current limitation in case of overloads, named in this case transient virtual impedance. The transient virtual impedance is mostly implemented as

a series element in the circuit [140], [141], [142], alternatives however do exist that implement the impedance in parallel with the LCL filter capacitor [143]. In this work the virtual impedance in series is only considered, as it will be shown that it provides the faster response to a fault. A simplified form of virtual impedance principle is found also in [144]. There, in case an over-current is detected, the actual current is multiplied with a scalable gain, in order to limit its value in the safe operational region and the inverter does not sense the presence of overload or fault. In case of steady state virtual impedance selecting a proper impedance ratio is carefully performed, depending on the grid topology and the desired load sharing. Most of the steady state virtual impedances are inductive, due to the derivation of droop control which is based on high voltage inductive grids. In the case of transient virtual impedance however, it is a complicated matter on how to properly design the impedance ratio. One way of selecting the impedance ratio is by evaluating the system stability around an equilibrium point. Instability can be produced due to the digital implementation of virtual impedances, for example through the sampling delay of the inverter's processing unit. It has been demonstrated that, if all practical implementations of a mixed virtual impedance are taken into consideration, increasing the inductive part of the impedance decreases the stability margin near the equilibrium point [145]. In this work the focus lies on implementing a pure resistive transient virtual impedance.

The goal of the current limitation is to limit the inverter's current, i_1 as shown in Fig. 6.6a. It would therefore be expected to place the transient virtual impedance in the loop between inverter and filter capacitor. It can be however shown that it is more reasonable to select the grid current i_2 and to place the virtual impedance after the capacitor. The reason is twofold. First, the inverter current is not sinusoidal and has a high frequency ripple which can be filtered out, introducing however a time-delay due to the filtering method. Secondly, for the transient virtual impedance it is of high importance to act rapidly and limit the current as soon as possible. It can be shown that the transfer function $G_{cu} = \dfrac{I_2}{I_1}$ shows a low pass filter behavior, and the outer current reacts to the transient effect faster. The transfer function output to input current, G_{cu} is calculated in Eq. 6.7, treating the grid part as a disturbance to the behavior of the filter, and incorporating also R_d, the resistor used for passive damping of the LC filter resonance. All variables can be identified in Fig. 6.6a, similar to the theoretical model of the grid interface of an inverter with LCL filter, as previously shown in Fig. 3.17.

$$G_{cu} = \frac{I_2(s)}{I_1(s)} = \frac{R_d C_f s + 1}{L_2 C_f s^2 + (R_2 + R_d) C_f s + 1} \tag{6.7}$$

It can be seen from Fig. 6.5 that the behavior of G_{cu} is similar to a low pass filter. Therefore the output current i_2 is chosen to build up the virtual impedance. Instabilities when selecting the inner inverter current for the realization of tran-

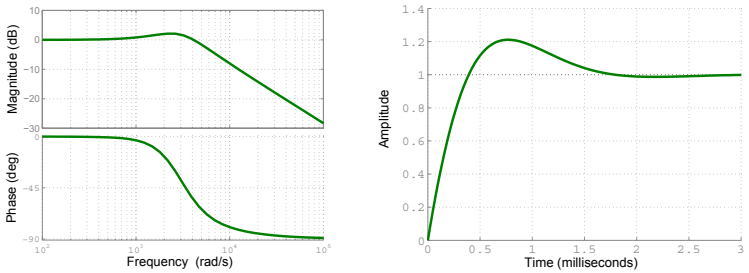

(a) Bode plot (b) Step response

Fig. 6.5: Steady state and dynamic response of G_{cu}

sient virtual impedances have also been documented in [103]. The transient virtual impedance can be calculated as shown in Fig. 6.6b.

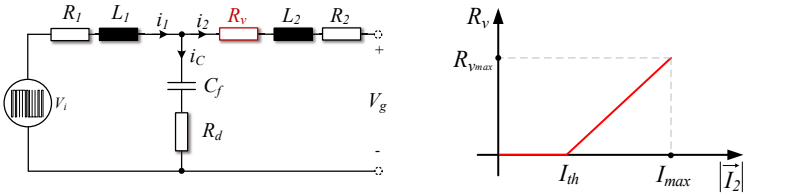

(a) Circuit integration (b) Non-linearity of virtual impedance

Fig. 6.6: Representation of transient virtual impedance

The implementation of the virtual impedance is depicted in Fig. 6.7. The imple-

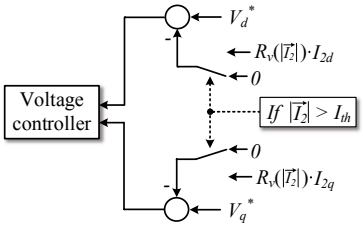

Fig. 6.7: Implementation of transient virtual impedance

mentation reveals the main disadvantage of the transient virtual impedance, the switching between states. Since it is not desired to have a virtual impedance ac-

tive during normal operation, a non-linear transient impedance is formed, which is activated as soon as the current exceeds the limit I_{th}, as shown in Fig. 6.6b. The linear increase of the virtual resistor depending on the current amplitude has a further impact on the voltage and current coupling. Following Ohm's law, in the case of a resistor there is a linear relation between voltage and current. Introducing such a non-linearity alters this relation, as explained in the following equations:

$$R_v = \frac{V_{R_v}}{I_2} \qquad R_v = \alpha I_2 \tag{6.8}$$

where V_{R_v} is the amplitude of the virtual voltage drop across the virtual resistor, I_2 the amplitude of the outer current and α is the linear relation of the virtual resistor and the current amplitude, when the current exceeds its threshold value. Combining both equations shown in Eq. 6.8, the following equation is obtained:

$$V_{R_v} = aI_2^2 \tag{6.9}$$

It is therefore concluded that introducing the non-linear virtual resistor with linear dependence on the current a quadratic relation between voltage and current is formed. This calculation does not take into consideration the delays that are introduced through the voltage and current controller of the inverter that realize the transient non-linear virtual resistor.
For the calculation of $R_{v_{max}}$ the worst case scenario is needed. This is chosen as the case where the fault occurs directly at the output of the grid forming inverter, at its PCC. In this way the grid impedance is minimum and the maximum current should be provided from the inverter.

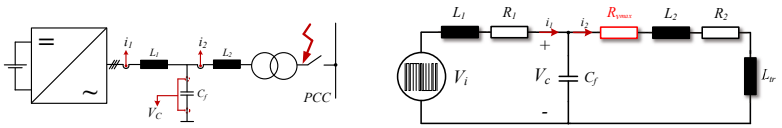

(a) Fault location for worst-case (b) Single-phase equivalent

Fig. 6.8: Circuits for calculating $R_{v_{max}}$

The damping resistor R_d is omitted for the calculation as shown in Fig. 6.8 since its value is insignificant compared to the rest of the circuit elements. The maximum virtual resistor, $R_{v_{max}}$ is then given by the following equation.

$$R_{v_{max}} = \sqrt{\frac{\Delta V^2}{I_{max}^2} - (\omega(L_2 + L_{tr}))^2} - R_2 \tag{6.10}$$

where ΔV is the voltage drop that should be artificially built to resemble the virtual resistor. In this work it is selected equal to 0.95 pu, leaving an operational margin for the voltage during fault.

6.2.2 Theoretical fault models

To better understand the transient behavior of the grid forming inverter, theoretical fault models are derived. These models can be used to conduct stability analysis of more complex grid structures. From the single-phase control representation of the grid forming inverter depicted in Fig. 6.9, simplified fault models can be calculated [137]. The dotted lines in Fig. 6.9 indicate the cur-

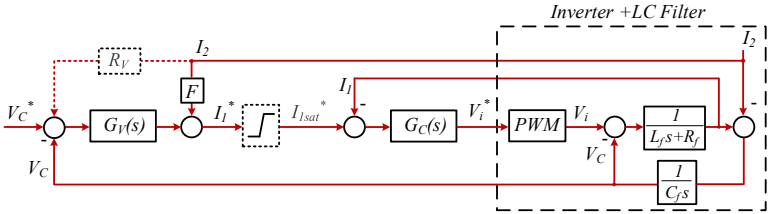

Fig. 6.9: Single-phase control representation with current limiting

rent limiting methods of current reference saturation or virtual impedance. The transfer functions of the voltage and current PI controllers are $G_V(s)$ & $G_C(s)$ respectively and F is the feed-forward factor for the output current. Analyzing the control structure of Fig. 6.9 the following equivalent structures can be obtained. During normal operation, the grid forming inverter can be represented as

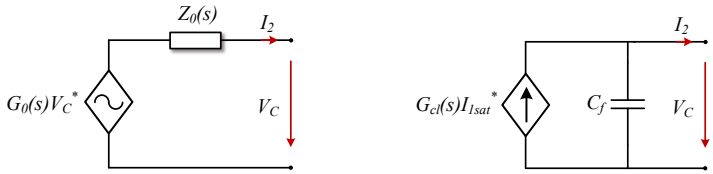

(a) with virtual impedance (b) with current reference saturation

Fig. 6.10: Inverter simplified fault model

a controlled voltage source behind an impedance, quite similar to the representation of a synchronous generator in power system stability studies [10]. However, when the current limitation is active, the grid forming inverter can no longer control the output voltage and behaves like a controlled current source behind the filter capacitor. Fig. 6.10 shows the respective equivalent circuits. Equations 6.11-6.13 provide the necessary calculations to reach these simplifications.

$$G_0(s) = \frac{G_V(s)G_C(s)}{sC_f[G_C(s) - (R_f + sL_f)] + G_V(s)G_C(s)} \tag{6.11}$$

$$G_{cl}(s) = \frac{G_C(s)}{G_C(s) - (R_f + sL_f)} \tag{6.12}$$

$$Z_0(s) = \frac{G_C(s)[F - R_v G_V(s) - 1] + (R_f + sL_f)}{sC_f[G_C(s) - (R_f + sL_f)] + G_V(s)G_C(s)} \tag{6.13}$$

It is shown that the inverter transforms into a current source when the current reference saturation is activated. In the case of virtual impedance however, the inverter is able to control its output voltage similar to normal operation. In other words, the voltage controller remains active during the fault. The inverter still operates as a voltage source with a modified grid-interfacing impedance. This could be a great advantage as far as stability investigations are concerned, since:

- the grid voltage is maintaned under control even in fault case.
- non-linearities introduced due to the current limiting method and the transformation to current source can be eliminated.
- systems based on more than one inverters can be easier analyzed, since each converter operates still as a voltage source with a defined output voltage and impedance, opposed to current source operation.

The equations 6.11-6.13 and therefore the theoretical fault models derived from them do not include the practical implementation issues coupled with the virtual resistor. First, the transient nature that includes a switching event is not taken into consideration. Secondly, the non-linear relation between transient virtual impedance and output current, $R_v(I_2)$ could not be included in the calculations, since it would complicate the simplified equivalent circuits. The impact of these two important implementation elements of the virtual resistor on the system response is discussed in the following sections.

6.2.3 Evaluation of current limiting methods

The previously described control methods are compared in real time simulation scenarios. The two main scenarios needed for the performance evaluation include fault response in standalone and parallel operation. The fault is simulated as a three phase symmetrical fault that lasts 10 grid periods. The fault detection and clearance is not part of these investigations, however the selected fault duration represents a worst-case scenario of the time needed from typical protection means to isolate a distribution line fault. In standalone operation, the grid forming inverter is the only grid forming unit in the microgrid. Therefore, the dynamic and stable response of the inverter to a fault is the main comparison criterion. Parallel operation means that more than one grid forming units

are working in parallel. In our investigations, the parallel operation of a grid forming inverter with a synchronous generator is chosen as a realistic scenario. The transient response of the microgrid, as far as voltage and frequency stability are concerned, is the main investigation aspect.
For the real time simulation scenarios that follow the vector amplitude saturation (limitation) is compared with the introduced transient virtual impedance. The alternative current reference saturation methods are not further considered since:

- The separate saturation does not fully utilize the current rating of the inverter.
- Setting saturated values requires further implementation complexity and introduces switching between different references that can cause unwanted transient effects.

6.2.3.1 Standalone operation

The current limiting methods are compared based on their transient robustness, with the following criteria:

- fast provision of over-current
- stable current limitation during fault
- exiting limitation state with minimum transient effect

In standalone operation the frequency response could also be a tool to evaluate the current limiting methods. However, the frequency control is realized through the transformation angle for the SRRF and it is not directly affected from the saturation of the PI controllers. Therefore, the controllability of the frequency cannot really be exploited as a comparison criterion.
The rated power for the grid forming inverter for both standalone and parallel operation is selected at $S_{inv} = 2MVA$. However, the current rating of the inverter is selected in this case equal to $I_{max} = 3$ pu. In this way, an overcurrent provision can be ensured to aid in fault detection and isolation. In the following figures (VAL) stands for vector amplitude limitation and (VI) for virtual impedance. In Fig. 6.11a the amplitude of the converter current, I_1 is shown for standalone operation since this is the current that should be limited. Despite the fact that the vector amplitude limiting method appears to react faster than the virtual impedance method, the latter produces smoother transitions, especially while exiting the current limitation. The results for both limiting methods seem quite similar as far as the converter current amplitude and hence the protection of inverter components is concerned. To obtain a more detailed insight, the amplitude of the voltage across the filter capacitor is depicted in Fig. 6.11b. It can be observed that the virtual impedance method, since it provides a smoother and slower response than the vector amplitude limitation shows no over-voltages while exiting the fault, but produces a higher voltage

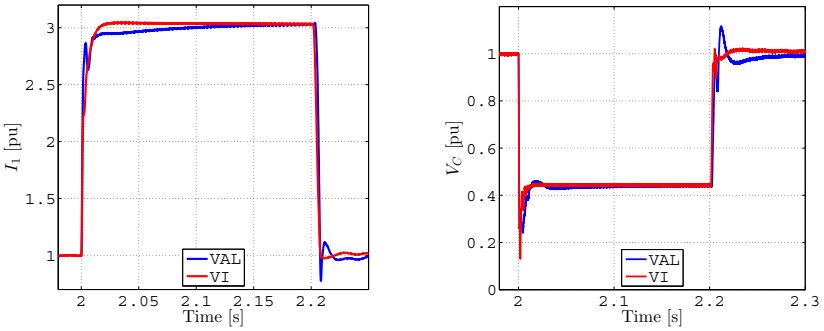

(a) Converter current amplitude

(b) Capacitor voltage amplitude

Fig. 6.11: Fault response of grid forming inverter in standalone operation

drop upon the fault activation. The conclusion from the standalone operation is that both methods can achieve satisfactory results with the virtual impedance method producing a more stable current response with the expense of excessive voltage drop compared to vector amplitude limitation.

6.2.3.2 Parallel operation with synchronous generator

Since the focus of this work are hybrid microgrids, the parallel operation of the grid forming inverter with the synchronous generator is also a fundamental test scenario for performance evaluation. The circuit shown in Fig. 6.12 and the parameters for the synchronous generator given in Table A.3 are used for this test scenario. This topology represents a worst-case scenario, since the grid impedance connecting the two grid forming units is minimal. We have seen in chapter 2 that the stability margins, as far as system eigenvalues are considered, increase with increasing lengths of the distribution lines between grid forming units. The worst case scenario for the fault location which minimizes the grid impedance is also in this case considered. The fault is located at the common voltage bus of the two generators. The fault duration and impedance are identical to the test-scenarios for the standalone operation. In the following figures, G_{Form} stands for grid forming inverter and SG stands for synchronous generator. The current depicted, I_{Gen} denotes the synchronous generator output current and the converter current. The test scenario of the parallel operation is performed once for the case of vector amplitude limitation (VAL) and is repeated for the case of virtual impedance limitation (VI).

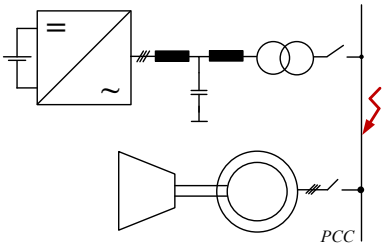

Fig. 6.12: Topology for parallel operation

The first observation from Fig. 6.13 is that the current limitation is in both cases successful and the inverter provides the selected maximum 3 pu overcurrent. The synchronous generator on the other hand is able to provide a significantly higher amount of overcurrent reaching almost 6.5 pu. Oscillations occur, which is to be expected due to the rotational speed swings of the generator. The transient phenomenon after the fault is cleared lasts in both cases almost 2 seconds. Comparing Fig. 6.13a & Fig. 6.13b it is observed that with the virtual impedance method the current reaches faster its maximum limit. This behavior deviates from the results obtained for the standalone operation. Since the inverter in this scenario is not the only grid forming unit in the microgrid, the transient response is affected by the oscillating response of the synchronous generator. The deviation from the maximum value of the current in the case

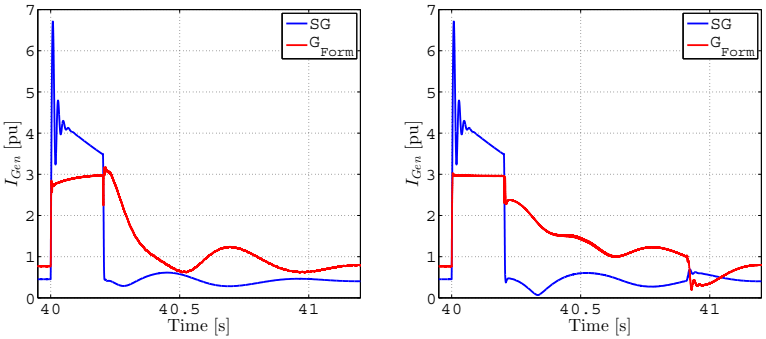

(a) with vector amplitude limitation (b) with virtual impedance

Fig. 6.13: Generator current amplitude during parallel operation

of vector amplitude limitation is less than 0.1 pu and it is elliminated after a few grid periods. Therefore, this deviation is not considered as a significant comparison criterion. The main difference however between both methods occurs when the virtual impedance is deactivated. At about $t = 40.9$ seconds the current

reaches the selected threshold value, $I_{th} = 1.1$ pu, and the virtual impedance is switched off. To further examine the impact of this transient effect, the voltage of each distributed generator V_{Gen} is shown in Fig. 6.14.

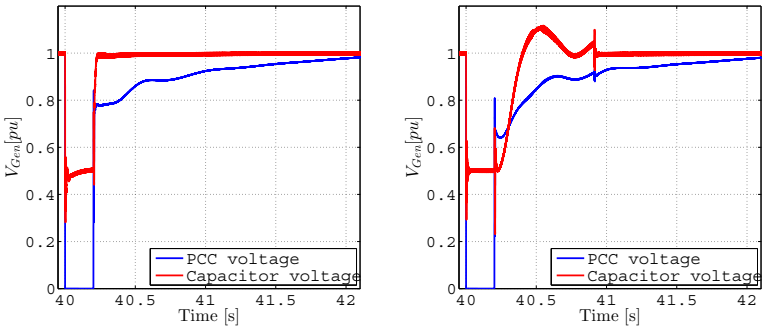

(a) with vector amplitude limitation (b) with virtual impedance

Fig. 6.14: Generator voltage amplitude during parallel operation

The output voltage of the synchronous generator is the PCC voltage, whereas the filter capacitor voltage is chosen for the inverter, to directly show the influence of the voltage control loop. There are no overvoltages present applying the vector amplitude limitation method and a steady state point is reached smoothly. On the other hand, an over-voltage is visible for the transient virtual impedance method. The reason is two-fold:

- First, the non-linearity of the virtual resistor. The linear dependence of the virtual resistor on the output current, does not consider the existence of other generators working in parallel. The interactions of the inverter with other generators cause a deviation on the interconnection of the actual inverter current I_2 with the non-linear virtual resistor as shown in Fig. 6.15. It is to be expected that in the region of the current between I_{th}

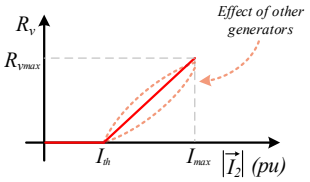

Fig. 6.15: Mismatch of virtual impedance calculation

- I_{max} the grid impedance, which is in series with the virtual resistor, has a non-negligible value and causes deviations from the pre-calculated

linear dependence of current amplitude and transient non-linear virtual resistor. Since calculating the actual grid impedance as well as the load sharing between generators in real time and adjusting the non-linearity of the virtual resistor upon them poses severe difficulties, only the linear dependence is considered in this work. Upon fault clearance, the inverter's controller does not cooperate ideally with the virtual resistor since the oscillations of the synchronous generator directly affect the load that the inverter should take over and over-voltages are produced.

- The deactivation of the virtual impedance. Since the virtual resistance depends on the current amplitude and not on each d- or q- component of the current, the deactivation of the voltage drop of the q-component produces this jump of the voltage. An optimization to eliminate this jump would be to transform the virtual resistor from current amplitude to current component dependent, but that would lead to not utilizing the full capability of the inverter, which is based on the current amplitude.

To complete the comparison, the frequency-related parameters of the hybrid microgrid are depicted in Fig. 6.16. The mechanical rotational speed of the synchronous generator is shown, along with the droop control reference for the grid forming inverter. The grid frequency at the common voltage bus detected with a PLL is also included in the figure to validate that the system starts and returns to the same steady state point. The measured PLL frequency during the fault is to be discarded, since the voltage is less than 0.01 pu and the measurement is therefore unreliable.

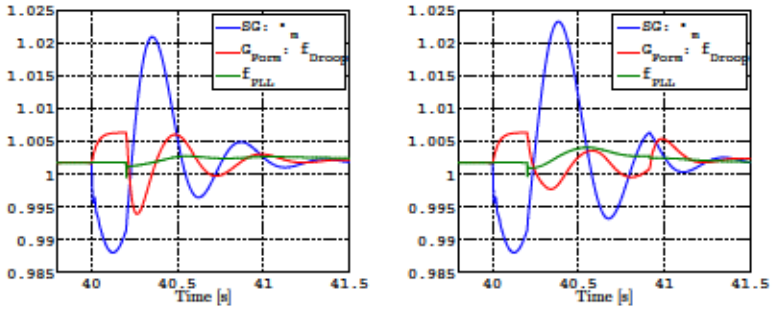

(a) with vector amplitude limitation (b) with virtual impedance

Fig. 6.16: Frequency-related parameters during parallel operation

As previously stated, frequency swings occur which are due to the inertia of the rotor of the diesel generator. On the other hand, the frequency reference of the grid forming inverter tries to pull up the frequency to a reference close to 1 pu. Since the voltage drops and the current increases, the output power remains within normal operation limits and therefore the frequency reference is close to its nominal value. In this operation the droop curves are selected identical for

both diesel generator and grid forming inverter with $P_{set} = 0.5$ pu. It is shown in Fig. 6.16a that the frequency reference during the fault is higher than the nominal frequency. That means that the inverter, despite the fact that it delivers $I_{max} = 3$ pu, the active power output is less than 0.5 pu. This is due to the grid impedance that the inverter 'sees' as a load. This impedance is mainly inductive, since the filter and transformer inductive impedance are a few orders higher than the fault resistance chosen to be $R_{fault} = 1\text{m}\Omega$. The frequency response of the grid forming inverter during the fault is in both limiting methods almost identical. Comparing closely Fig. 6.16a & 6.16b it is observed that the over-speed of the generator after the fault is slightly higher, and also at $t = 40.9$ seconds, the deactivation of the virtual impedance is once more evident.
Therefore, in parallel operation with the synchronous generator the vector amplitude limiting method achieves better performance than the virtual impedance limiting method. The virtual impedance is introduced as an intelligent solution to overcome the non-linearities that are introduced with the limiting methods based on current reference saturation. However, the practical problems that arise with its implementation, and the effect that the unpredictable grid impedance has on the system behavior lead to the selection of the vector amplitude limiting method as the method that performs quite well in both test-scenarios documented in this section.

6.2.3.3 Parallel operation with no current over-rating

The last test scenario to evaluate current limiting methods for grid forming inverters is the case when the inverter is not over-sized and the current limitation is close to its nominal value, $I_{max} = 1.1pu$. In this case the synchronous generator is the dominant grid forming unit in the microgrid, with the grid forming inverter playing a secondary role in the over-current provision. The implementation of the transient non-linear virtual impedance is practically not feasible, since I_{max} and I_{th} have the same value. If the virtual resistor was implemented, upon its activation a significant jump on the voltage would appear, since the virtual impedance would not be non-linear, but fixed to its maximum value, $R_{v_{max}}$. The performance of the current vector amplitude limitation is shown in the following figures, to demonstrate stable parallel operation with the sychronous generator, even in the case of no over-current provision from the inverter. It can be seen from Fig. 6.17a that the transient effect of the short-circuit forces the inverter to remain longer with its current limitation activated. This is due to the fact that the synchronous generator cannot instantly return to its prior fault loading conditions and during that period the inverter takes over the excess load. This effect can be clearly observed in the output voltage, see Fig. 6.17b. As long as the current limitation of the inverter is active, the voltage is lower than the nominal value. Comparing Fig. 6.14a with Fig. 6.17b, it can be seen that without over-current provision from the inverter, the voltage restoration shows worse transient behavior. Similar to the output voltage, the decisive parameters

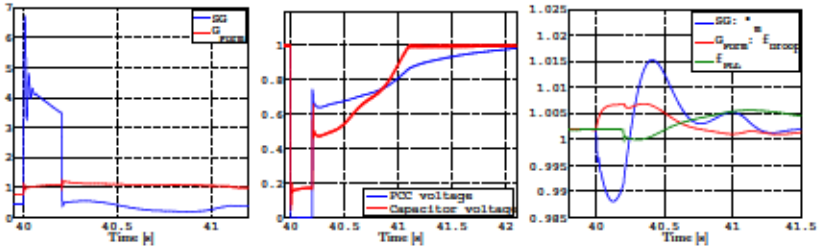

(a) Current I_{Gen} in pu (b) Voltage V_{Gen} in pu (c) Frequency in pu

Fig. 6.17: Parallel operation with no over-rating

for the frequency response in Fig. 6.17c is compared with the corresponding results in Fig. 6.16a. As a main difference, in Fig. 6.17c a lower over-speed for the synchronous generator can be identified. Here, the influence of the inverter on the grid frequency, namely trying to 'pull it up' close to its nominal value is smaller, since it contributes with a quite smaller fault current. Therefore, the synchronous generator is not influenced by the presence of the inverter and its over-speed is reduced. This however does not lead to faster frequency restoration, since in both cases the fault recovery, as far as the frequency is concerned, lasts up to 1.5 seconds. The PLL response seems to be slower in the case of no overrating, but this depends also on the voltage being measured, which has not reached its steady state yet and can have a negative impact on the frequency measurement. Concluding these investigations, it can be seen from the results that the vector amplitude limitation method can achieve promising results in all cases, whereas the virtual impedance method has weak points that arise from its practical implementation.

6.2.4 DC and AC components rating

The rating of the components of each distributed generator is a significant element of the proposed short circuit strategy. Therefore, it is proposed to distinguish between inverter and AC part rating, and DC part and input energy source rating. The current limiting method for the inverter was explained in the previous section. To proceed with the rating selection the DC power source should be defined. In this chapter a battery pack is considered, using the model proposed in chapter 3. In Fig. 6.18 the distributed generator based on the battery pack is shown.
Two new components are introduced in addition to Fig. 3.39 and Fig. 3.30 to ensure the stable operation with different rating for the DC and AC parts of the distributed generator. First, the saturation of the current reference for the D-component. The grid forming inverter cannot demand in this way more active power than what the DC-part can deliver. Secondly, a further current limita-

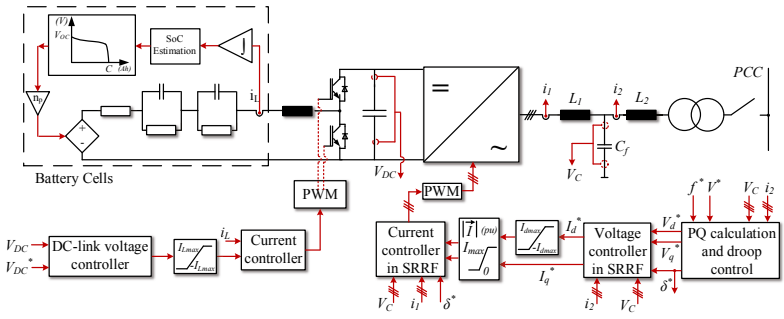

Fig. 6.18: Distributed generator based on a battery pack

tion is introduced for the current reference for the DC/DC converter to limit the output current of the battery. The two limits, I_{dmax}, I_{Lmax} are selected equal (in pu) so that the power flow to/from the DC-link can remain intact. It will be demonstrated in the next section that for the case of grid feeding inverters these limits are different, depending on the grid voltage. For the grid forming inverter however that is not the case, since the inverter is considered a load for the input source and the input DC current is adjusted dynamically based on the inverter output current. Since the battery pack, or any other energy power source that could be the input of the grid forming inverter, typically costs significantly more than the AC-part of the distributed generator, it is reasonable to select $I_{max} > I_{dmax}$. This selection is performed not only for cost reduction, as well as for technical considerations and advantages. First of all, there should be a protection margin between the two values to overcome transient effects that might occur. Second, since the goal of the short circuit strategy is to maximize the fault current, oversizing only the grid forming inverter could lead to increasing the available reactive power to be provided. This is further investigated in the next sections, where the grid feeding inverter is also considered to contribute to the fault current.

6.3 Grid feeding inverter

The control objective for the grid feeding inverter during fault is quite more straight-forward than the grid forming inverter. That is because grid feeding inverters prevail in mainland 'stiff' grids (see Fig. 2.1a) and grid codes and guidelines have been introduced that govern their behavior. In the case of grid forming inverters however, which are not thought to operate in parallel with the stiff grid but to build a weak microgrid (see Fig. 2.1b), the operational guidelines are currently developed. In this work, as explained in the previous section, the

grid forming inverter is able to provide a certain amount of over-current. That is however insufficient for building-up the over-currents that are needed for typical protection means, as seen in Fig. 6.1. Therefore, also the grid feeding inverters should aid in this direction, stay connected during faults and provide up to their rated current in all cases. In this section, starting from the traditional grid code requirements for grid feeding inverters, their suitability is investigated in the case of hybrid microgrids and guidelines are also in this case derived.

6.3.1 Grid code requirements

The grid code requirements for static grid support from grid feeding inverters were shortly mentioned in chapter 3. The reactive current injection more specifically was shown in Fig. 3.22. The case of grid over-voltages and consequently reactive current absorption is not considered in this work, since the focus is fault cases which cause significant voltage drops. Analyzing once more Fig. 3.22, it is evident that the grid feeding inverter should remain grid-connected and inject 1 pu reactive current. The questions that rise are time-related: how long should the inverter remain grid connected and how fast should the reactive current injection be realized.

Fault duration For the maximum fault duration fault-ride-through characteristics have been included in the grid codes [61] and a typical curve is shown below in Fig. 6.19. Analyzing Fig. 6.19, the guideline is that the inverter

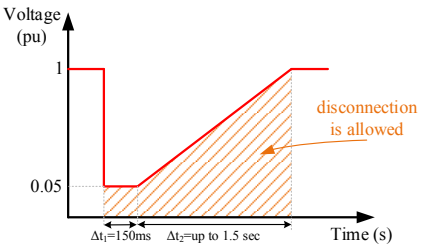

Fig. 6.19: Fault-ride-through characteristic

should stay connected at least for 150 ms as soon as the fault occurs with a maximum voltage drop of 95%. In other cases the maximum voltage drop can reach up to 1 pu. The voltage restoration follows, and if the restoration lasts more than 1.5 seconds the inverter is allowed to disconnect. This characteristic was mainly developed for stiff grids. In our case, since the microgrid stiffness is quite lower, the voltage restoration time limit should be eliminated and the inverter should remain at all times connected.

Robustness of reactive current injection Robustness is defined in this paragraph as how fast and accurate should the reactive current injection (RCI) take place. In Fig. 6.20 & Table 6.1 the tolerance bands as defined in the grid code [146] are depicted.

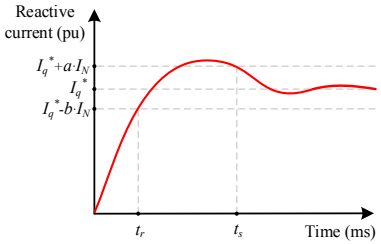

Fig. 6.20: RCI tolerance bands

Tolerance band characteristics	Value
Upper limit, α (pu)	0.2
Lower limit, β (pu)	0.1
Maximum response time, t_r (ms)	30
Maximum settling time, t_s (ms)	60

Table 6.1: RCI parameters

It is worth to be noted that a transient period for the reactive current injection is tolerated both in duration and settling time, as well as amplitude mismatches. The settling time is defined as the time period from when the reactive current inserts until it stays within the pre-determined amplitude tolerance band. An alternative grid code, [61] suggest a faster maximum settling time t_s of 40 ms.

6.3.2 Realization of reactive current injection

To fulfill the grid code requirements of injecting up to 1 pu reactive power, several methods can be utilized [147]:

- Curtailment of the DC power injected to the DC-link.
- A means of flexible active transmission system (FACTS) like the static compensator (STATCOM) can be connected in parallel with the grid feeding inverter. The topology of STATCOM is identical to the grid feeding inverter, with the difference that there is not input power source on the DC-side. In this way, the inverter can freely generate or absorb reactive power up to 1 pu.
- The grid feeding inverter can be oversized to meet the grid requirements.
- Energy storage systems (ESS) can be deployed to store the incoming DC power. In this way the grid feeding inverter can operate as a STATCOM, providing (or absorbing) reactive power to (or from) the grid.

In this work providing additional equipment to overcome a fault is not considered a realistic option. Either oversizing the grid feeding inverter, or reducing the input power can achieve similar results with significantly lower costs. The realization of the active power curtailment depends on the topology and characteristics of the energy source of the grid feeding inverter. For grid feeding inverter in PQ mode, a simple change in the PQ setpoints that are fed into the inverter's controllers, see Fig. 3.26, can rapidly change the active power fed to the DC-link and inject the required 1 pu reactive current. For grid feeding inverters connecting renewable energy sources (RES), the realization is more complicated.
For wind turbines, taking advantage of the inertia of the wind turbine can help disposing the excess active power. The unnecessary active power can produce an accelerating torque for the turbine, removing the incoming current to the DC-link [148]. It was demonstrated in [149] that this process for a back-to-back frequency converter connecting a permanent magnet synchronous machine to the grid can be realized within up to 10 switching periods of the stator side converter. The over-speeding control method was selected to realize the acceleration of the wind turbine, rapidly modifying the speed control of the converter. It has been also demonstrated in [150] that this method of accelerating the wind turbine during a fault can be also applied in doubly fed induction generator (DFIG) based wind turbines where the frequency converter is in the rotor circuit, with the stator being directly coupled with the grid.
For photovoltaic plants, a similar strategy can be deployed in the component that performs maximum power point tracking (MPPT). In a two-stage system, where a DC/DC converter is in charge of MPPT, a voltage close to the open-circuit voltage should be rapidly set, so that the active power output can be curtailed. In one-stage systems, where the grid feeding inverter controlling the DC-link voltage automatically sets the solar module voltage, the system can be considered as self-protected. As soon as a reactive current reference is set, the DC-link voltage starts to increase, and in turn reduces the power the modules generate [151].
Therefore, the worst case for grid feeding inverters is the case of wind turbines where a delay of up to 10 switching periods of the stator-side converter is required to realize the active power curtailment. The vector amplitude limiting method is selected for the cascaded control structure, since it has shown promising results in the case of grid forming inverters. The RES-emulator shown in Fig. 6.21 generates the reference for the current that reaches the DC-link and, in case a voltage drop is detected, minimizes this DC-current with a delay of ten switching periods of the stator-side converter of a wind turbine e.g. 5ms. In this way, the dynamics of the DC-link are realistically modeled during fault. An alternative would be to include a detailed model of the RES-side converter, but that would increase the model complexity without providing any additional information about the behavior of the system. The reactive current reference, I_q^* is chosen according to the ENTSOE-E draft network code (Fig. 3.22).

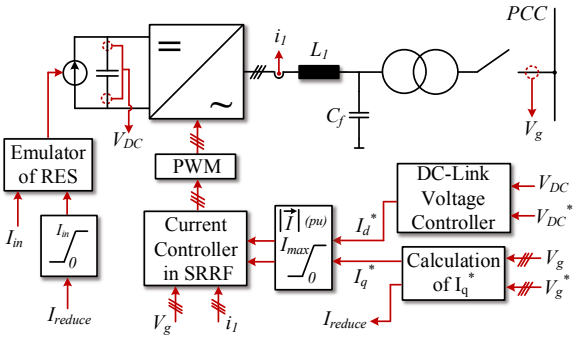

Fig. 6.21: Grid feeding inverter modeling for fault investigations

6.3.3 Evaluation of reactive current injection

The choice of reactive current as means of grid support by renewable-energy based distributed generators is twofold:

- The main disadvantage of renewable energy is its stochastic energy provision. Therefore it is a safe option to set only reactive current as injection reference in case of a fault, since a grid inverter can provide at any time any amount of reactive power as long as its DC-link voltage is properly managed. Special care should be given for unsymmetrical faults where the current reference for the current injection should be included in positive and negative sequence components [152]. The protection means work with current amplitude, therefore it is irrelevant if this current is reactive or active, the priority is to have the maximum amplitude.
- High voltage grids are mainly inductive. In this case, the fault impedance consists of the distribution line and transformer inductive impedance which requires reactive power.

In case of medium voltage grids however, the impedance ratio is variable. As already shown in chapter 2 and more specifically in Fig. 2.7, the impedance has a $\frac{X}{R}$ ratio of ~1 - 4. That means that both active and reactive power are needed during fault. In order to further evaluate the impact of the reactive current injection principle in medium voltage microgrids, the active and reactive power flow in the microgrid should be thoroughly analyzed for various fault impedances. The circuit shown in Fig. 6.22 is formed for this purpose. This topology depicts the steady state representation of inverter-based generators working in parallel as soon as a fault occurs. Although the focus of this work is hybrid microgrids, the synchronous generator is considered in this scenario disconnected to demonstrate a worst-case scenario. It is to be compared, if the amplitude of the fault current

is higher with or without the presence of the grid feeding units realizing reactive current injection. Steady state conditions are considered, since the power flow between generators is the focus, and not the transition during and after the fault. In Fig. 6.22 R_i, L_i are resistance and inductance of the distribution lines and

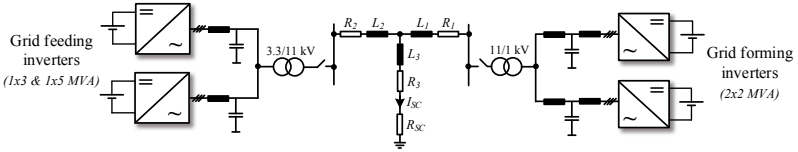

Fig. 6.22: Topology for RCI evaluation

R_{sc}, I_{sc} fault resistance and current. The parameters used for the simulation of this microgrid are found in Table A.13. The rated power of the grid feeding units is selected double from the grid forming units. It is reasonable to proceed in this way, since (i) the challenge of integrating renewable energy sources is to minimize the energy storage requirements and (ii) the cost of storage systems is reasonably higher than renewable energy sources [3]. The energy storage means in our case, a battery pack, is connected through the grid forming inverters. The DC-link dynamics are neglected in this scenario, since only steady state calculations are needed.
The test scenario conditions and guidelines for each distributed generator are summarized once more:

- The grid feeding inverters are supposed to deliver only reactive current according to the RCI principle.
- As soon as the current limitation of the grid forming inverter is activated, the outer voltage controller is effectively deactivated, converting the generator into a current source, as shown in Fig. 6.10b. This modeling approach is valid as long as the grid load is larger than the inverter rating, which is always the case in a fault scenario.

The current limitation for the grid forming inverter maximum current, the D-component of the current and the battery output current are selected $I_{max} = 3$ pu and $I_{dmax} = I_{Lmax} = 1.1$ pu respectively. The *pu* representation is based on the parameters of Table A.13. The DC-part of the grid forming inverter-based distributed generator is therefore rated for only the nominal current, and only the inverter is over-sized. The grid feeding inverter is providing its rated reactive current, equal to 1 pu according to the grid codes requirements. The fault impedance is modeled as a pure resistance with a parameter sweep from 1 mΩ to 1 Ω. The length of the distribution line in series supplying the fault is kept constant, $L_3 = 1$ km. In Fig. 6.23, with dashed lines the corresponding results are shown also for the case that the grid feeding inverter (G_{Feed}) is disconnected.

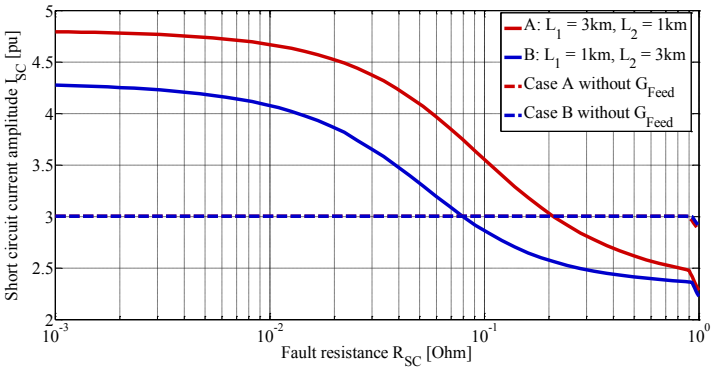

Fig. 6.23: Fault resistance sweep

The short circuit current amplitude is normalized to the sum of the rated current of the grid forming inverters, to ease reading the figure. For lower impedances, the excessive current from the grid feeding inverters is absorbed through the grid, whereas when the impedance gets more ohmic the short circuit current drops. After the value of $R_{SC} = 80\text{m}\Omega$ and $200\text{m}\Omega$ for case A and B respectively, it is no longer useful to keep the grid feeding inverters connected, since it mainly overloads the grid forming inverters. It is evident that a reactive power exchange takes place between the inverter-interfaced distributed generators. When the grid impedance becomes ohmic, most of the reactive power injected from the grid feeding inverters is absorbed through the grid forming inverters. Close to $R_{SC} = 1\Omega$ the grid forming inverter exits the current limitation since the excessive reactive current is no longer needed. It can be further deduced that if the fault is located closer to the grid feeding inverters the fault current increases. This is due to the fact that when L_2 increases, the grid forming inverters has to provide active power towards the grid feeding inverters to compensate the line losses, not contributing to the fault. Based on these results, to increase the short circuit current capability of any system comprised of grid forming and grid feeding inverters for a variety of fault impedances, I_{dmax} & I_{Lmax} are increased from 1.1 to 2 pu.

6.3.4 Mixed current injection (MCI) principle

As shown in the previous section, the implementation of the reactive current principle does not maximize in all cases the fault current. Due to the non-inductive characteristic of the distribution lines, even in fault impedances as low as $R_{SC} = 80\text{m}\Omega$ reactive power exchange between the distributed generators takes place. This reactive power exchange leads to excessive losses, and most

importantly reduces the fault current. With reduced current, fault detection and isolation could become impossible for the grid protection mechanism.

6.3.4.1 Interpretation of measured grid voltage

The main guideline for the development of the short circuit strategy is its dependence only on local measurements and no means of communication. To identify the severity of the fault, the measured grid voltage at the point of common coupling of the grid feeding inverter is used. Similar to the reactive current injection principle of Fig. 3.22, depending on the grid voltage the grid feeding inverter should inject a certain amount of current to support the fault. In Fig. 6.24 the distributed energy resource (DER) depicts the distributed generator that is connected through the grid feeding inverter, R_l & L_l the distribution line impedance, and R_{SC} the fault resistance. A controlled voltage source is also de-

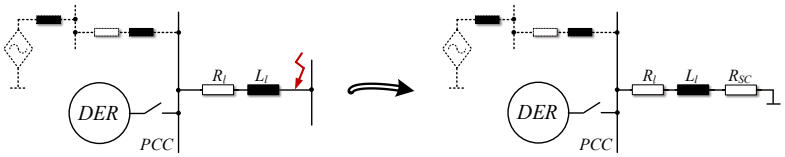

Fig. 6.24: Formulation of fault impedance

picted in the figure, to represent the grid forming units (synchronous generator or grid forming inverter) that are connected through the fault and also supply a fraction of the short circuit current. It is drawn with a dashed line, since its position and grid connection cannot be exactly known. Their fault contribution cannot be measured or estimated, therefore the grid voltage at the PCC of the grid feeding inverter can vary depending on the overall short circuit current. Observing Fig. 6.24, the coupling between grid voltage of the grid feeding inverter (voltage at PCC) and the fault impedance can be derived:

- Independent of the short circuit impedance, the fault impedance will always have an ohmic characteristic due to the medium voltage distribution line attributes.
- If the fault impedance is relatively small or the fault is located closer to the PCC the resulting voltage drop will be lower. On the other hand, if the fault impedance is relatively large, or the fault is located away from the PCC, the voltage drop becomes higher.

Therefore, measuring the voltage at the point of common coupling of the grid feeding inverter can give a useful insight on the grid current requirements during the fault. At this point it should be noted that the voltage also depends on the grid topology and the short circuit current provision of other generators, but the concept remains the same.

6.3.4.2 Calculation of MCI limits

The last subsection explained that the injected current should be directly linked to the measured PCC voltage. To develop such a fault current-grid voltage diagram, the maximum DC input current to the DC-link of the inverter depending on the output voltage should be first calculated. The cause of this limitation for the DC current is that the DC-link voltage is constant but the inverter's output voltage strongly depends on the grid voltage. If this is not taken into consideration, the power balance equation of the DC link, Eq. 3.35 will lead to a voltage increase, since the input current cannot be absorbed from the inverter. The input DC current can be regulated from the DC-link chopper or directly from the renewable energy source side converter. To calculate the input DC current limits of the grid feeding inverter the single phase representation of Fig. 6.26 is formed.

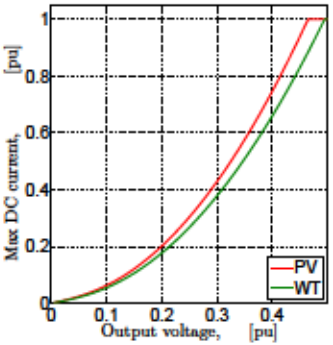

Fig. 6.25: Maximum DC current

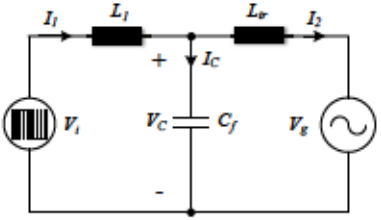

Fig. 6.26: Circuit for $I_{in_{max}}$ calculation

The calculation is performed in two main steps: First the maximum permissible voltage amplitude at the inverter output is calculated from the following equations:

$$\begin{aligned} \bar{V}_i &= j\omega L_1 \bar{I}_1 + \bar{V}_C \\ \bar{V}_C &= j\omega L_2 \bar{I}_2 + \bar{V}_g \\ \bar{I}_1 &= \bar{I}_C + \bar{I}_2 \\ \bar{I}_C &= j\omega C_f \bar{V}_C \end{aligned} \tag{6.14}$$

The equations of 6.14 are almost identical with Eq. 3.13 - 3.15. The losses of the parasitic resistors of the inductors, as well as the damping resistor are neglected. The current in Eq. 6.14 is set to the maximum inverter current, in the case of grid feeding inverters to $I_{2_{max}} = 1\ pu$. Furthermore, it is considered that the output current is in phase with the grid voltage, namely that the inverter is feeding

the grid only with active power. For this calculation the principles of mixed or reactive current injection is discarded, and normal steady state operation with lower grid voltage is considered. Since all elements of Eq. 6.14 are known, the inverter's output voltage can be found, and subsequently the maximum input DC current from Eq. 6.15:

$$I_{in_{max}} = \frac{3V_{i_{rms}}I_{1_{rms}}}{V_{DC}} \tag{6.15}$$

Implementing these equations for both grid feeding inverters of Fig. 6.29 the curve of Fig. 6.25 can be calculated. In this curve the maximum permissible input current for the inverter is formed in dependence of its output voltage. No big differences are observed during the two grid feeding inverters with the different rated power. This is due to the fact that the filter characteristics are also adjusted depending on the rated power of the inverter. This maximum current can now be utilized to form the MCI curve that should govern the behavior of the grid feeding inverters during the fault.

6.3.4.3 Development of MCI diagram

After identifying the current limits due to inverter's rating, the MCI curve can be developed as shown in Fig. 6.27. This current should be 'mixed', composed of both active and reactive component. As previously mentioned, the grid voltage is utilized to identify the severity of the fault. Pure reactive current injection is deployed only in severe faults and by decreasing voltage drop active current is also injected. The limit after which the inverter should further provide only active current is selected at $V_g = 0.2\ pu$ where, as it can be read from Fig. 6.25, the inverter can provide $I_{in_{max}} = 0.2\ pu$ maximum DC input current. This operation point is selected identical for both photovoltaic park and wind turbine, since their difference in Fig. 6.25 is negligible. As previously mentioned, MCI is a current injection principle that follows the mixed impedance of distribution lines. In Fig. 6.27, I_{in} refers to the input current to the DC-link, as depicted in Fig. 6.21. Fig. 6.27 can be classified as a modified PQ diagram for grid feeding inverters in fault cases. The drawbacks of this method is twofold:

- the RES-based generator can provide mixed current only when their input source allows them to. In case of insufficient DC current, an inner line of the diagram of Fig. 6.27 should be followed. This is however not a severe drawback, since the amount of I_n required is minimal by severe faults, as proven in the last subsection, see Fig. 6.25.
- As previously mentioned in Section 6.1, overloading conditions should not be allowed in inverter-based microgrids. Introducing the principle of mixed current injection, highly inductive loads that cause grid voltage drops might pose a threat for the stability of the system. When connecting such loads, or in the case of higher inrush or motor magnetizing currents a grid voltage

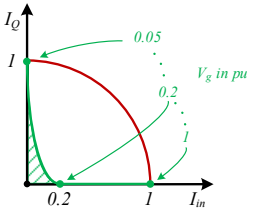

Fig. 6.27: MCI principle

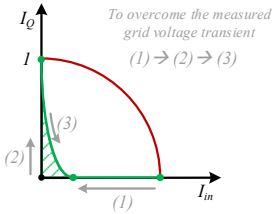

Fig. 6.28: MCI step-by-step process

drop would appear. If this voltage drop is not severe enough, the grid feeding inverters continue to provide the active power previous to the fault, as shown in Fig. 6.27. In that case the grid forming units overtake the provision of excess reactive power. To overcome this problem, grid guidelines for the allowed inrush currents should be formulated for all grid loads.

- The MCI principle could be quite sensitive to the transients of the measured grid voltage. Therefore the process of reaching the setpoint of the MCI-diagram is explained in Fig. 6.28. Depending on the grid voltage drop, first the DC-link incoming current is reduced. Reactive current injection is then activated, followed by the final adjustment of the setpoint as soon as the grid voltage reaches a stable, with tolerances, value.

The MCI process should be quantified depending on the rated power of the grid feeding inverter and the microgrid topology. The priorities are the maximization of the fault current as well as the protection of the power electronic components of the grid feeding inverter. An implementation example of the method as well as a comparison between both injection principles (RCI & MCI) follows.

6.4 Validation of proposed strategy

Real time simulation test scenarios are formulated to validate the performance of the proposed control modifications for the inverter-based distributed generators. The assumptions for the development and evaluation of the proposed strategy are once more here summarized:

- Symmetrical faults are only considered. It is well known that the faults majority are unsymmetrical. In this work an effort is made so that the basics of a short circuit strategy are formulated, which can be further expanded to successfully face any type of fault.

- Loads are disconnected as soon as the voltage drop appears. The reality is quite more complicated: Households and other types of loads, such as street lights, are not inverter-interfaced to the grid and would remain connected in case of not so severe voltage drops. Another case would be industrial loads with power electronic interface that could sense the grid voltage, and as soon as a drop appears, the loads can be disconnected. In our investigations severe faults are considered, where the voltage drop is significant, and even if the loads remained connected, the majority of the current would flow to the fault location and not the loads, since the fault impedance is significantly lower.
- Fault detection and isolation are not the focus of this work. Therefore selectivity and setting the protection means accordingly is not included.

The proposed control strategy is validated in the hybrid microgrid of Fig. 6.29. Four distributed generators are present with a meshed structure interconnecting them. As previously mentioned, a meshed structure is not typical for medium voltage grids, but it could represent a grid structure of a real island, where for reliability reasons a meshed structure is proposed. The voltage and rated power level of each generator is also shown in Fig. 6.29.

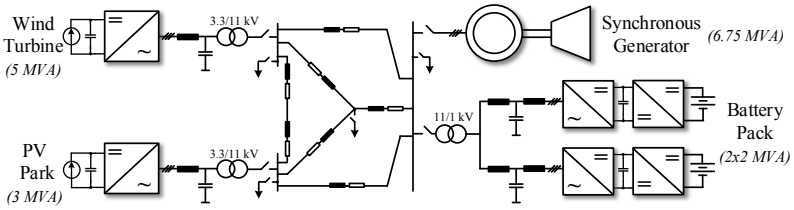

Fig. 6.29: Hybrid microgrid for validation of short circuit strategy

Similar to the previous chapters, the generators parameters can be found in Tables A.3 & A.6. Test scenarios with and without the synchronous generator are performed to investigate respectively: The co-existence of rotational and non-rotational distributed generators in fault conditions and the capability of inverter-based generators to overcome the fault and supply over-current. The response of the synchronous generator in the first few periods right after the fault, the so called sub-transient period is the focus of this work. The control structure shown in Section 3.1.2 is not altered for the development of the short circuit strategy. The fault location is selected in the middle of the distribution line that connects the two RES-based distributed generators. Other alternatives would be directly at the output of the grid feeding inverters or the common voltage bus of the grid forming units. However, these alternatives would not provide any useful insights for the evaluation of the short circuit strategy. If the fault was located directly at the output of a grid feeding unit, the MCI principle

would produce a pure reactive current setpoint since the grid voltage would be minimal. On the other hand, if the fault was located at the common voltage bus of the grid forming units, the MCI principle would be strongly favored, since the fault impedance for the grid feeding units would be mainly ohmic. Furthermore, the results of such a test scenario, concerning voltage and frequency stability, were also documented in the evaluation of current limiting methods between grid forming units in parallel in the previous section. Therefore, the fault location is kept constant and resembles also a worst case scenario with a realistic varying fault impedance.

6.4.1 Operation with synchronous generator

The first test scenario includes the diesel generator to document what occurs when two different grid forming units are involved in the fault. In this case, the fault current is scaled with the nominal current of the diesel generator and the fault resistance is $R_{SC} = 1$ mΩ. Since the fault resistance in this scenario is minimal, a comparison between the injection principles is not necessary, since the grid voltage is lower than 0.05 pu and the grid feeding inverters inject only reactive power. As shown in Fig. 6.30a, in less than two grid periods the

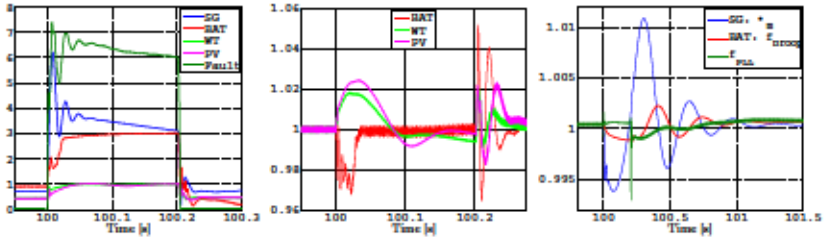

(a) Current in *pu* (b) Voltage in *pu* (c) Frequency *pu*

Fig. 6.30: Real time simulation results with diesel generator

inverter-based generators provide their maximum current, supporting the fault. The I_{dmax} saturation component causes the additional transient effect observed in the current of the grid forming inverter just a few ms after the fault occurs. The absolute value of the fault current is almost equally supplied by the diesel generator and the inverter-based generators. The RES manage to deliver the reactive current reference almost within 30 milliseconds, fully meeting the grid requirements explained in Fig. 6.20 with no over-currents and unwanted transients. The DC-link voltage of all three inverters (only the behavior of one grid forming inverter is shown since their operation is identical) is shown in Fig. 6.30b. The apparent control difference can be deduced from the response of the DC-link voltage: The grid forming inverter experiences a voltage drop due to the excess load. Previously to the fault, due to the presence of the synchronous

generator and the current provision of the grid feeding inverters the battery pack is charged. The fault is therefore 'sensed' as an excessive load for the grid forming inverter. The grid feeding inverters on the other hand show a voltage increase due to the implementation of the mixed current injection strategy. As previously mentioned, the delay of four switching periods of the input converter is responsible for the small voltage increase, but it remains within the allowed boundaries.
The frequency response in Fig. 6.30c is formed by the different characteristics of each grid forming unit. A drop occurs in the rotational speed of the synchronous generator, whereas the frequency reference for the inverter sets a value close to its nominal one. The measured PLL frequency is shown, but cannot be fully reliable, since in faulty conditions the voltage to be measured is under 0.05 pu. Despite the overshoot of the rotational speed of the diesel generator, both grid forming units manage to synchronize afterwards, reaching a steady state. It is worth to be mentioned that if the fault duration is increased beyond realistic limits, frequency instabilities can occur. However, the 10 grid periods duration selected in this work is considered a realistic worst-case scenario.

6.4.2 Operation without synchronous generator

On a more demanding scenario, the synchronous generator is disconnected, and the inverter-based generators are responsible for providing over-current. The fault resistance is once more sweeped to investigate the performance of the MCI principle.

$\boldsymbol{R_{SC} = 1\text{m}\Omega}$ Same conditions with previous test scenario are applied, and also in this test scenario the grid voltage is under the limit of 0.05 pu, and only reactive current is injected from the grid feeding inverters. Fig. 6.31a depicts the amount of current that each generator provides to the fault. The fault current is scaled once more to the nominal current of the diesel generator to compare it with the first test scenario. All three inverters manage to effectively control their output current. An important remark should be pointed out at this point. Observing the beginning of the fault, it can be clearly seen that the fault current is not the sum of the other three distributed generators. This is due to the fact that the current of each inverter-based generator is measured before the LC filter, directly at the output of the inverter. This location is selected to demonstrate that the current is effectively limited and the power electronics components are at all times protected. The impact of each LC(L) filter is the reason for the mismatch of the currents shown in Fig. 6.31a. The DC-link voltage shown in Fig. 6.31b verifies the previous analysis. First, the DC-link voltage of the grid forming inverter experiences in this case an increase instead of a decrease shown in the previous test scenario. This is due to the fact that since the diesel generator is not present in this scenario but the load is constant,

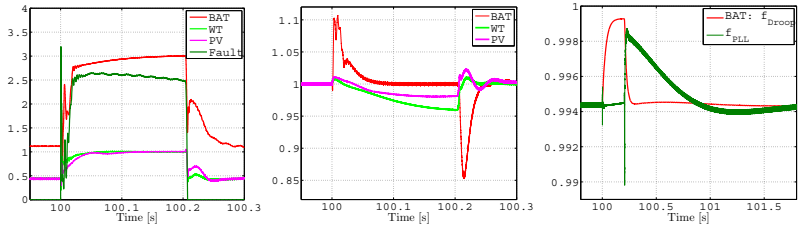

(a) Current in *pu* (b) Voltage in *pu* (c) Frequency in *pu*

Fig. 6.31: Real time simulation results without diesel generator

the battery pack is discharged prior to the fault. As soon as the fault occurs, the grid voltage drops and the excessive DC-current injected to the DC-link is no longer needed. The DC-link voltage of the grid feeding inverter experiences also a small drop right after the initial voltage jump due to the delay of the RES emulator. This voltage drop is minimal and after a few periods the voltage stabilizes. Increasing the fault duration showed that the DC-link voltage returns eventually to the nominal value. The frequency response is quite similar to the previous test scenario and since the oscillations of the diesel generator are not present, a smoother transient phenomenon is documented.

$R_{SC} = 0.5\Omega$ An increased fault resistance is selected in this scenario, to demonstrate the advantages of MCI. Both current injection principles are implemented, to compare their effectiveness. Instead of increasing the fault resistance, the fault location could have been altered and selected further away from the grid feeding inverters. The frequency response is not shown in this test-scenario, as it shows similar behavior to Fig. 6.31c. Comparing figures 6.32a & 6.32b, the first observation is that the fault current in the case of mixed current injection is significantly increased. As previously explained, this is due to the ohmic character of the overall fault impedance that the grid feeding inverter senses. Furthermore, after the fault is isolated, a transient effect causes the inverters currents to exceed their safety limits. In that case, the power electronic components would have been destroyed. On the other hand, in the case of MCI the inverters currents remain within limits. An oscillating behavior is however observed in the currents of the grid feeding inverter. The DC-link voltage should be also examined to justify the existence of both transient phenomena. Figure 6.33 aids in the clarification of the response of the inverter-interfaced distributed generators.

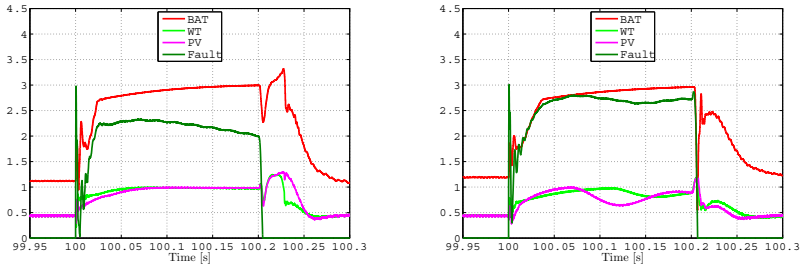

(a) with RCI (b) with MCI

Fig. 6.32: Current amplitude in *pu* with $R_{SC} = 0.5\ \Omega$

In the case of RCI the DC-link voltage collapses. The maximum reactive current cannot be delivered to the grid since the fault impedance is ohmic and the grid forming inverter cannot absorb it. Furthermore, a certain amount of active power should be delivered to compensate for distribution line, transformer and filter losses. This active power cannot be delivered in this case from the grid forming inverter, and the power balance of the DC-link collapses.

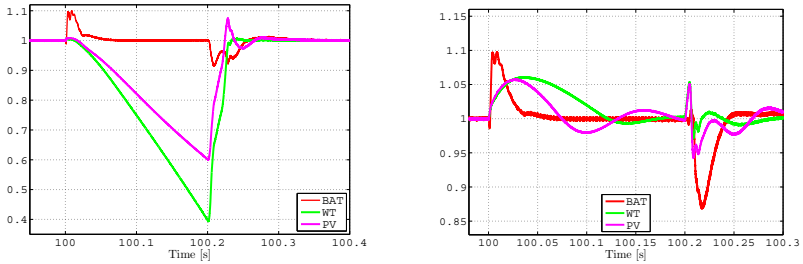

(a) with RCI (b) with MCI

Fig. 6.33: DC-link voltage in *pu* with $R_{SC} = 0.5\ \Omega$

On the other hand, in the case of MCI the DC-link voltage experiences an oscillating behavior. This is due to the DC-link dynamics and partly due to the capacitance selected, which is quite small compared to the rated power of the generator. Increasing the DC-link capacitor could reduce but not fully eliminate the transient. The oscillating behavior is also caused from the setpoint imposing of the MCI principle. This setpoint selection is elaborated thoroughly in Fig. 6.35.

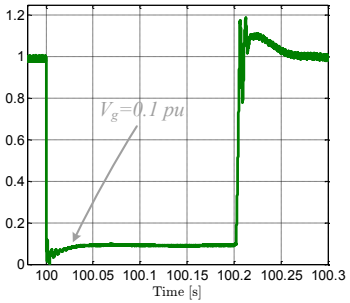

Fig. 6.34: Grid voltage amplitude in *pu*

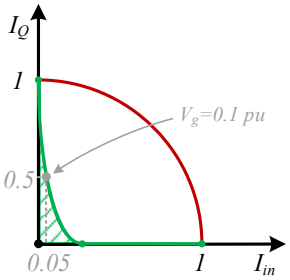

Fig. 6.35: Calculating MCI setpoint

As soon as the fault occurs, the voltage drop appears and the incoming current to the DC-link is reduced, according to Fig. 6.28. As soon as the output voltage stabilizes to $V_g = 0.1$ *pu* as shown in Fig. 6.34 the reactive current injection has started and the setpoint of $I_Q = 0.5$ *pu*, $I_{in} = 0.05$ *pu* is formulated. The grid voltage tolerance band is selected in this case $\pm$ 0.01 *pu* and the MCI setpoint calculation lasts 40 *ms*, which, as previously analyzed, is depending on the grid voltage response. Over-voltages occur upon the isolation of the fault, which is to be expected due to the severity of the fault and the 'short' electrical distances between generators and fault location. The over-voltage reaches up to 1.2 *pu* of the nominal value.

6.5 Short circuit strategy conclusions

In this chapter the fault response of different distributed generators is analyzed and documented. The optimal current limiting method for grid forming inverters for both standalone and parallel operation is proposed. The selection of the limiting method is based on both theoretical fault analysis and real time simulation results. The required modeling depth for grid feeding inverters during fault conditions is further described. The principle of reactive current injection is presented, and its suitability for medium voltage hybrid microgrids is investigated. Based on the theoretical analysis of the parallel operation of inverter-interfaced distributed generators with limited short circuit current capability the RCI principle is optimized. A mixed current injection (MCI) principle is proposed with the clear objective of maximizing the fault current. Real time simulation results validate the effectiveness of the proposed method.

7 Conclusions

In the previous chapters several technical problems of inverter dominated microgrids were analyzed. In order to provide solutions for these problems, modeling techniques in the direction of real time simulation were developed. The focus of the investigations was mainly the inverter-interfaced distributed generators and their interactions after a transient grid disturbance.

7.1 Contributions to state of the art

As a base of this work, the detailed models of various distributed generators have been in depth analyzed. These models were associated with several control strategies for medium voltage microgrids with a wide time focus. The black start process with different grid forming units has been simulated and documented and the synchronization process of a droop-controlled grid forming inverter to a microgrid was thoroughly analyzed. A control algorithm was proposed to enable smooth synchronisation with no transients as far as voltage and frequency are concerned. Furthermore, the problem of transient load sharing was investigated and the concept of frequency reference switching was proposed. The impact of droop gains, load types and grid impedance on the transient load sharing has been demonstrated. The oscillations that microgrids with different grid forming units experience after severe load steps were successfully minimized. Moreover, the principle of SoC-Adaptive droop control was proposed, a means to increase the autonomy of any microgrid, incorporating secondary control within primary control. Real time simulations of hybrid microgrids with central and distributed storage means have verified the suitability of the proposed algorithm. Finally, a short circuit strategy for the inverter-based distributed generators was developed. Objectives of the short circuit strategy were the maximization of the fault current, as well as the stable parallel operation of grid forming units. Two different current limiting methods have been proposed and compared for the grid forming inverter. Their performance has been investigated in standalone scenarios as well as in a parallel operation with the synchronous generator. For the grid feeding units, the principle of mixed current injection has been introduced. The proposed concept is based on the traditional reactive current injection that dominates in the case of stiff grids. The measured output grid voltage is linked with the active and reactive power setpoint that the inverter should inject to the grid in fault case. Various real time simulation scenarios

validate the capability of the grid inverters in fault case to provide over-current as well as preserve the voltage and frequency stability during and after the fault.

7.2 Further research points

Despite that several operational aspects of inverter-dominated microgrids have been in depth analyzed, further research points for the expansion of the proposed control strategies can be identified:

- The parallel operation of grid forming units with different time constants has been thoroughly investigated in this work. However, the control structure of the grid forming inverter should be further expanded with a symmetrical components analysis to face unsymmetrical loads or faults. Furthermore, it remains to be investigated if the problematic of transient load sharing is deteriorated in the presence of severe unsymmetrical load changes.
- Optimizing SoC-Adaptive droop control and combining it with battery-friendly setpoints. That could be charging strategies such as the constant current or constant voltage control methods [153] that increase the lifetime expectancy of battery cells.
- The short circuit strategy proposed in this work should be further expanded to cover also the case of unsymmetrical faults. For grid forming units, the proposed principle of transient virtual impedance could be implemented in a different reference frame and compared with the traditional control structure in SRRF. In that case a symmetrical components analysis is required for grid feeding inverters. In order to maximize its short circuit current contribution, the principle of MCI should be combined with positive or negative sequence current injection, which has been already developed for the case of reactive current injection [154], [155].
- To calculate precisely fault currents and tune respectively the protection measures, not only generators should be in detail modeled. In-depth analysis of further grid components such as loads and transformers should be included in future investigations of transient response of such microgrids. In the case of loads, instead of the typical constant impedance modeling, an alternative would be the ZIP model [156]. In that case each load is modeled with an impedance, a current source and a power source in parallel. As far as transformers are concerned, saturation effects could be also investigated, integrating also iterative processes to directly define the transformer saturation curve, similar to [157].

Bibliography

[1] R. Lasseter, "Microgrids," in *Power Engineering Society Winter Meeting, 2002. IEEE*, vol. 1, pp. 305–308 vol.1, 2002.

[2] C. Colson, M. Nehrir, R. Sharma, and B. Asghari, "Improving sustainability of hybrid energy systems part i: Incorporating battery round-trip efficiency and operational cost factors," *Sustainable Energy, IEEE Transactions on*, vol. 5, pp. 37–45, Jan 2014.

[3] D. Prull, *Design and Integration of an Isolated Microgrid with a High Penetration of Renewable Generation*. PhD thesis, University of California Berkeley, 2008.

[4] K. Schemionnek, *Zur Erzeugung einphasiger sowie dreiphasiger symmetrierbarer Konstantspannungssysteme variabler Frequenz durch selbstgeführte Wechselrichter*. PhD thesis, TU Berlin, 1973. (in German).

[5] J. Rocabert, A. Luna, F. Blaabjerg, and P. Rodriguez, "Control of power converters in ac microgrids," *Power Electronics, IEEE Transactions on*, vol. 27, pp. 4734–4749, Nov 2012.

[6] J. Guerrero, M. Chandorkar, T. Lee, and P. Loh, "Advanced control architectures for intelligent microgrids part i: Decentralized and hierarchical control," *Industrial Electronics, IEEE Transactions on*, vol. 60, pp. 1254–1262, April 2013.

[7] J. Uudrill, "Dynamic stability calculations for an arbitrary number of interconnected synchronous machines," *Power Apparatus and Systems, IEEE Transactions on*, vol. PAS-87, pp. 835–844, March 1968.

[8] H. Li, M. Steurer, K. Shi, S. Woodruff, and D. Zhang, "Development of a unified design, test, and research platform for wind energy systems based on hardware-in-the-loop real-time simulation," *Industrial Electronics, IEEE Transactions on*, vol. 53, pp. 1144–1151, June 2006.

[9] B. Lu, X. Wu, H. Figueroa, and A. Monti, "A low-cost real-time hardware-in-the-loop testing approach of power electronics controls," *Industrial Electronics, IEEE Transactions on*, vol. 54, pp. 919–931, April 2007.

[10] P. Kundur, *Power System Stability and Control*. McGraw-Hill, 1994.

[11] J. Schiffer, *Stability and Power Sharing in Microgrids*. PhD thesis, Technische Universität Berlin, 2015.

[12] J. Büchner, J. Katzfey, O. Flörcken, A. Moser, and M. Uslar, "Abschlussbericht zum forschungsprojekt nr. 44/12 'moderne verteilernetze für deutschland'," tech. rep., Studie im Auftrag des Bundesministeriums für Wirtschaft und Energie (BMWi), 2014. (in German).

[13] T. Völker, *Regelung unsymmetrisch belasteter Inselnetze durch unabhängige Wechselrichter im Parallelbetrieb*. PhD thesis, Universität Bremen, 2009. (in German).

[14] M. Prodanovic, T. Green, and H. Mansir, "A survey of control methods for three-phase inverters in parallel connection," in *Power Electronics and Variable Speed Drives, 2000. Eighth International Conference on (IEE Conf. Publ. No. 475)*, pp. 472–477, 2000.

[15] T. Caldognetto and P. Tenti, "Microgrids operation based on master - slave cooperative control," *Emerging and Selected Topics in Power Electronics, IEEE Journal of*, vol. 2, pp. 1081–1088, Dec 2014.

[16] J. Peas Lopes, C. Moreira, and A. Madureira, "Defining control strategies for microgrids islanded operation," *Power Systems, IEEE Transactions on*, vol. 21, pp. 916–924, May 2006.

[17] Siemens AG, *Product Brochure: Spectrum Power - Advanced Microgrid Management System.*

[18] ABB Power Generation, *Product Brochure: MGC600 - Renewable Microgrid Controller.*

[19] GE - Digital Energy Sector, *Product Brochure: Grid IQ - Microgrid Control System.*

[20] M. Chandorkar, D. Divan, and R. Adapa, "Control of parallel connected inverters in standalone ac supply systems," *Industry Applications, IEEE Transactions on*, vol. 29, pp. 136–143, Jan 1993.

[21] A. Tuladhar, K. Jin, T. Unger, and K. Mauch, "Parallel operation of single phase inverter modules with no control interconnections," in *Applied Power Electronics Conference and Exposition, 1997. APEC '97 Conference Proceedings 1997., Twelfth Annual*, vol. 1, pp. 94–100 vol.1, Feb 1997.

[22] Brugg Cables, *GKN4-LeiterNS-Polymerkabel Datasheet*, 2013. (in German).

[23] Prysmian cables and systems, *VPE-Kabel mit Cu-Leiter N2XS2 Datasheet*, 2007. (in German).

[24] A. Engler and N. Soultanis, "Droop control in lv-grids," in *Future Power Systems, 2005 International Conference on*, pp. 6 pp.–6, Nov 2005.

[25] J. Guerrero, J. Matas, L. G. de Vicuna, M. Castilla, and J. Miret, "Decentralized control for parallel operation of distributed generation inverters using resistive output impedance," *Industrial Electronics, IEEE Transactions on*, vol. 54, pp. 994–1004, April 2007.

[26] K. De Brabandere, B. Bolsens, J. Van den Keybus, A. Woyte, J. Driesen, R. Belmans, and K. Leuven, "A voltage and frequency droop control method for parallel inverters," in *Power Electronics Specialists Conference, 2004. PESC 04. 2004 IEEE 35th Annual*, vol. 4, pp. 2501–2507 Vol.4, 2004.

[27] R. Majumder, B. Chaudhuri, A. Ghosh, R. Majumder, G. Ledwich, and F. Zare, "Improvement of stability and load sharing in an autonomous microgrid using supplementary droop control loop," *Power Systems, IEEE Transactions on*, vol. 25, pp. 796–808, May 2010.

[28] O. Osika, *Stability of Micro-Grids and Inverter-dominated Grids with High Share of Decentralized Sources.* PhD thesis, Universität Kassel, 2005.

[29] E. Coelho, P. Cortizo, and P. Garcia, "Small-signal stability for parallel-connected inverters in stand-alone ac supply systems," *Industry Applications, IEEE Transactions on*, vol. 38, pp. 533–542, Mar 2002.

[30] M. Jostock, *Stabilität wechselrichtergeführter Inselnetze.* PhD thesis, Universität Luxembourg, 2013. (in German).

[31] I. Boldea, *Synchronous Generators*. Taylor & Francis, 2006.

[32] IEEE Power Engineering Society, *IEEE Std. 421.5: Recomended Practice for Excitation System Models for Power System Stability Studies*, 2005.

[33] Basler Electric Company Ltd., *Mathematical per-unit model of the DECS-200 excitation system*, 2001.

[34] A. Godhwani and M. Basler, "A digital excitation control system for use on brushless excited synchronous generators," *Energy Conversion, IEEE Transactions on*, vol. 11, pp. 616–620, Sep 1996.

[35] Z.-L. Gaing, "A particle swarm optimization approach for optimum design of pid controller in avr system," *Energy Conversion, IEEE Transactions on*, vol. 19, pp. 384–391, June 2004.

[36] R. Best, D. Morrow, D. McGowan, and P. Crossley, "Synchronous islanded operation of a diesel generator," *Power Systems, IEEE Transactions on*, vol. 22, pp. 2170–2176, Nov 2007.

[37] Converteam Ltd, *Standard Alpha SGT 100 Datasheet*, 2007.

[38] J. Lunze, *Systemtheoretische Grundlagen, Analyse und Entwurf einschleifiger Regelungen*. Springer-Verlag Berlin Heidelberg, 2008. (in German).

[39] P. Orlowski, *Praktische Regeltechnik*. Springer-Verlag Berlin Heidelberg, 2007. (in German).

[40] W. Duesterhoeft, M. W. Schulz, and E. Clarke, "Determination of instantaneous currents and voltages by means of alpha, beta, and zero components," *American Institute of Electrical Engineers, Transactions of the*, vol. 70, pp. 1248–1255, July 1951.

[41] N. Bottrell and T. Green, "Comparison of current-limiting strategies during fault ride-through of inverters to prevent latch-up and wind-up," *Power Electronics, IEEE Transactions on*, vol. 29, pp. 3786–3797, July 2014.

[42] S. Pokharel, S. Brahma, and S. Ranade, "Modeling and simulation of three phase inverter for fault study of microgrids," in *North American Power Symposium (NAPS), 2012*, pp. 1–6, Sept 2012.

[43] A. Rockhill, M. Liserre, R. Teodorescu, and P. Rodriguez, "Grid-filter design for a multimegawatt medium-voltage voltage-source inverter," *Industrial Electronics, IEEE Transactions on*, vol. 58, pp. 1205–1217, April 2011.

[44] R. Teodorescu, M. Liserre, and P. Rodriguez, *Grid converters for photovoltaic and wind power systems*. Wiley Ltd, 2011.

[45] L. Malesani, L. Rossetto, P. Tenti, and P. Tomasin, "Ac/dc/ac pwm converter with reduced energy storage in the dc link," *Industry Applications, IEEE Transactions on*, vol. 31, pp. 287–292, Mar 1995.

[46] M. Winkelnkemper, *Reduzierung von Zwischenkreiskapazitäten in Frequenzumrichtern für Niederspannungsantriebe*. PhD thesis, FG Leistungselektronik, Technische Universität Berlin, 2005. (in German).

[47] F. Jenni and D. Wüest, *Steuerverfahren für selbstgeführte Stromrichter*. vdf Hochschulverlag an der ETH Zürich, 1995. (in German).

[48] M. Liserre, F. Blaabjerg, and S. Hansen, "Design and control of an lcl-filter-based three-phase active rectifier," *Industry Applications, IEEE Transactions on*, vol. 41, pp. 1281–1291, Sept 2005.

[49] K. Jalili and S. Bernet, "Design of lcl filters of active-front-end two-level voltage-source converters," *Industrial Electronics, IEEE Transactions on*, vol. 56, pp. 1674–1689, May 2009.

[50] R. Meyer and A. Mertens, "Design and optimization of lcl filters for grid-connected converters," in *Power Electronics and Motion Control Conference (EPE/PEMC), 2012 15th International*, pp. LS7a.1–1–LS7a.1–6, Sept 2012.

[51] I. Gabe, V. Montagner, and H. Pinheiro, "Design and implementation of a robust current controller for vsi connected to the grid through an lcl filter," *Power Electronics, IEEE Transactions on*, vol. 24, pp. 1444–1452, June 2009.

[52] R. Ottersten, *On Control of Back-to-Back Converters and Sensorless Induction Machine Drives*. PhD thesis, Chalmers University of Technology, Sweden, 2003.

[53] L. Harnefors and H.-P. Nee, "Model-based current control of ac machines using the internal model control method," *Industry Applications, IEEE Transactions on*, vol. 34, pp. 133–141, Jan 1998.

[54] A. Yazdani and R. Iravani, *Voltage-Source Converters in Power Systems - Modeling, Control, and Applications*. Wiley, 2010.

[55] V. Blasko and V. Kaura, "A new mathematical model and control of a three-phase ac-dc voltage source converter," *Power Electronics, IEEE Transactions on*, vol. 12, pp. 116–123, Jan 1997.

[56] H. Lutz and W. Wendt, *Taschenbuch der Regelungstechnik*. Europa Lehrmittel Verlag, harri deutsch ed., 2014. (in German).

[57] S. Preitl and R.-E. Precup, "Points of view in controller design by means of extended symmetrical optimum method," in *IFAC Control Systems Design, Bratislava*, 2003.

[58] C. Kessler, *Das Symmetrische Optimum*. Zeitschrift Regelungstechnik, 1958. (in German).

[59] T. Sezi, "Fast and accurate measurement of power system frequency," in *Power and Energy Society General Meeting, 2010 IEEE*, pp. 1–7, July 2010.

[60] A. Timbus, M. Liserre, R. Teodorescu, and F. Blaabjerg, "Synchronization methods for three phase distributed power generation systems - an overview and evaluation," in *Power Electronics Specialists Conference, 2005. PESC '05. IEEE 36th*, pp. 2474–2481, June 2005.

[61] ENTSO-E, *Draft Network Code for Requirements for Grid Connection applicable to all Generators*, January 2012.

[62] BDEW, *Technische Richtlinie Erzeugungsanlagen am Mittelspannungsnetz*, Juni 2008. (in German).

[63] B. Weise, "Impact of k-factor and active current reduction during fault-ride-through of generating units connected via voltage-sourced converters on power system stability," *Renewable Power Generation, IET*, vol. 9, no. 1, pp. 25–36, 2015.

[64] N. Pogaku, M. Prodanovic, and T. Green, "Modeling, analysis and testing of autonomous operation of an inverter-based microgrid," *Power Electronics, IEEE Transactions on*, vol. 22, pp. 613–625, March 2007.

[65] E. Bueno, F. Espinosa, F. Rodriguez, J. Urefia, and S. Cobreces, "Current control of voltage source converters connected to the grid through an lcl-filter," in *Power Electronics Specialists Conference, 2004. PESC 04. 2004 IEEE 35th Annual*, vol. 1, pp. 68–73 Vol.1, June 2004.

[66] H.-B. Shin, "New antiwindup pi controller for variable-speed motor drives," *Industrial Electronics, IEEE Transactions on*, vol. 45, pp. 445–450, Jun 1998.

[67] C. Hamann and W. Vielstich, *Elektrochemie, 4. Auflage*. Wiley-VCH Verlag, 2005. (in German).

[68] A. Jossen and W. Weydanz, *Moderne Akkumulatoren richtig einsetzen*. Inge Reichardt Verlag, 2006. (in German).

[69] P. K. P. Ferraz, "Regelung und echtzseitsimulation einer batteriegestuetzen photovoltaikanlage am mittelspannungsnetz," Master's thesis, FG Leistungselektronik, TU Berlin, 2013. (in German).

[70] Saft, *Rechargeable Lithium-ion battery VL 34480 Datasheet*, February 2009.

[71] S. Buller, M. Thele, R. De Doncker, and E. Karden, "Impedance-based simulation models of supercapacitors and li-ion batteries for power electronic applications," *Industry Applications, IEEE Transactions on*, vol. 41, pp. 742–747, May 2005.

[72] D. Vladikova, "The techique of the differential impedance analysis, part i: Basics of the impedance spectroscopy," in *Advanced Techniques for Energy Sources Investigation and Testing, Sofia, Bulgaria*, 2004.

[73] H. Sira-Ramirez and R. Silva-Ortigoza, *Control Design Techniques in Power Electronics Devices*. Springer-Verlag London, 2006.

[74] A. Haruni, A. Gargoom, M. Haque, and M. Negnevitsky, "Dynamic operation and control of a hybrid wind-diesel stand alone power systems," in *Applied Power Electronics Conference and Exposition (APEC), 2010 Twenty-Fifth Annual IEEE*, pp. 162–169, Feb 2010.

[75] Infineon, *FF200R33KF2C IGBT-Module Datasheet*, March 2013.

[76] J. Adamy, *Nichtlineare Regelungen*. Spri, 2009. (in German).

[77] V. Öz, *Modellierung und Echtzeitsimulation eines Batteriesytems für autonome Photovoltaik-Anlagen*. Bachelor's thesis, FG Leistungselektronik TU Berlin, 2013. (in German).

[78] F. Haugen, *Discrete-time signals and systems*. TechTeach, February 2005. freeware document - available from http://techteach.no.

[79] S. Bowes, "New sinusoidal pulsewidth-modulated invertor," *Electrical Engineers, Proceedings of the Institution of*, vol. 122, pp. 1279–1285, November 1975.

[80] S. Bowes and M. Mount, "Microprocessor control of pwm inverters," *Electric Power Applications, IEE Proceedings B*, vol. 128, pp. 293–305, November 1981.

[81] J. Sun and H. Grotstollen, "Optimized space vector modulation and regular-sampled pwm: a reexamination," in *Industry Applications Conference, 1996. Thirty-First IAS Annual Meeting, IAS '96., Conference Record of the 1996 IEEE*, vol. 2, pp. 956–963 vol.2, Oct 1996.

[82] C. Dufour and J. Belanger, "Discrete time compensation of switching events for accurate real-time simulation of power systems," in *Industrial Electronics Society, 2001. IECON '01. The 27th Annual Conference of the IEEE*, vol. 2, pp. 1533–1538 vol.2, 2001.

[83] *Mask of Universal Bridge Model.* Matlab Simulink Simpower Systems Library, Mathworks S.A.

[84] *Mask of 2-level Time-Stamp-Bridge Model.* RT-Lab Library, Opal-RT.

[85] *Help manual of Universal Bridge Model.* Matlab Simulink Simpower Systems Library, Mathworks S.A.

[86] S. Chowdhury, S. P. Chowdhury, and P. Crossley, *Microgrids and active distribution networks.* The Institution of Engineering and Technology, 2009.

[87] S. Chakraborty, M. G. Simoes, and W. E. Kramer., eds., *Power Electronics for Renewable and Distributed Energy Systems.* Springer-Verlag London, 2013.

[88] N. Cai, X. Xu, and J. Mitra, "A hierarchical multi-agent control scheme for a black start-capable microgrid," in *Power and Energy Society General Meeting, 2011 IEEE*, pp. 1–7, July 2011.

[89] J. Dang and R. Harley, "Islanded microgrids black start procedures with wind power integration," in *Power and Energy Society General Meeting (PES), 2013 IEEE*, pp. 1–5, July 2013.

[90] S. Thale and V. Agarwal, "A smart control strategy for the black start of a microgrid based on pv and other auxiliary sources under islanded condition," in *Photovoltaic Specialists Conference (PVSC), 2011 37th IEEE*, pp. 002454–002459, June 2011.

[91] D. Dong, P. Wang, W. Qin, and X. Han, "Investigation of a microgrid with vanadium redox flow battery storages as a black start source for power system restoration," in *Industrial Electronics and Applications (ICIEA), 2014 IEEE 9th Conference on*, pp. 140–145, June 2014.

[92] J. Peas Lopes, C. Moreira, A. Madureira, F. Resende, X. Wu, N. Jayawarna, Y. Zhang, N. Jenkins, F. Kanellos, and N. Hatziargyriou, "Control strategies for microgrids emergency operation," in *Future Power Systems, 2005 International Conference on*, pp. 6 pp.–6, Nov 2005.

[93] C. Moreira, F. Resende, and J. Peas Lopes, "Using low voltage microgrids for service restoration," *Power Systems, IEEE Transactions on*, vol. 22, pp. 395–403, Feb 2007.

[94] J. Li, J. Su, X. Yang, and T. Zhao, "Study on microgrid operation control and black start," in *Electric Utility Deregulation and Restructuring and Power Technologies (DRPT), 2011 4th International Conference on*, pp. 1652–1655, July 2011.

[95] J. Ancona, "A framework for power system restoration following a major power failure," *Power Systems, IEEE Transactions on*, vol. 10, pp. 1480–1485, Aug 1995.

[96] J. Machowski, W. J. Bialek, and R. J. Bumby, *Power System Dynamics: Stability and Control.* John Wiley & Sons, 2008.

[97] T. Croft, P. F. Hartwell, and I. W. Summers, *American Electrician's Handbook.* McGraw-Hill, 2002.

[98] A. Gkountaras, S. Dieckerhoff, and T. Sezi, "Real time simulation and stability evaluation of a medium voltage hybrid microgrid," in *Power Electronics, Machines and Drives (PEMD 2014), 7th IET International Conference on*, pp. 1–6, April 2014.

[99] C.-T. Lee, R.-P. Jiang, and P.-T. Cheng, "A grid synchronization method for droop-controlled distributed energy resource converters," *Industry Applications, IEEE Transactions on*, vol. 49, pp. 954–962, March 2013.

[100] L. Sahoo, N. Thakur, K. Rai, P. Sensarma, R. Jha, P. Mohanty, A. Sharma, A. Srinidhi, and A. Chaurey, "Synchronization and operation of parallel inverters using droop control," in *Power Electronics and ECCE Asia (ICPE ECCE), 2011 IEEE 8th International Conference on*, pp. 2406–2412, May 2011.

[101] P. Zhang, R. Li, J. Shi, and X. He, "An improved reactive power control strategy for inverters in microgrids," in *Industrial Electronics (ISIE), 2013 IEEE International Symposium on*, pp. 1–6, May 2013.

[102] A. Micallef, M. Apap, C. Staines, and J. Guerrero Zapata, "Secondary control for reactive power sharing and voltage amplitude restoration in droop-controlled islanded microgrids," in *Power Electronics for Distributed Generation Systems (PEDG), 2012 3rd IEEE International Symposium on*, pp. 492–498, June 2012.

[103] A. Paquette, *Power Quality and Inverter-Generator Interactions in Microgrids*. PhD thesis, Georgia Institute of Technology, May 2014.

[104] Q. Fu, L. Montoya, A. Solanki, A. Nasiri, V. Bhavaraju, T. Abdallah, and D. Yu, "Microgrid generation capacity design with renewables and energy storage addressing power quality and surety," *Smart Grid, IEEE Transactions on*, vol. 3, pp. 2019–2027, Dec 2012.

[105] L. Guo, X. Fu, X. Li, and C. Wang, "Coordinated control of battery storage system and diesel generators in ac island microgrid," in *Power Electronics and Motion Control Conference (IPEMC), 2012 7th International*, vol. 1, pp. 112–117, June 2012.

[106] J.-H. Jeon, J.-Y. Kim, S.-K. Kim, and J.-M. Kim, "Unified compensation control of a hybrid energy storage system for enhancing power quality and operation efficiency in a diesel and wind-turbine based stand-alone microgrid," in *Power Electronics for Distributed Generation Systems (PEDG), 2012 3rd IEEE International Symposium on*, pp. 264–270, June 2012.

[107] H.-P. Beck and R. Hesse, "Virtual synchronous machine," in *Electrical Power Quality and Utilisation, 2007. EPQU 2007. 9th International Conference on*, pp. 1–6, Oct 2007.

[108] Q.-C. Zhong and G. Weiss, "Synchronverters: Inverters that mimic synchronous generators," *Industrial Electronics, IEEE Transactions on*, vol. 58, pp. 1259–1267, April 2011.

[109] M. Dewadasa, A. Ghosh, and G. Ledwich, "Dynamic response of distributed generators in a hybrid microgrid," in *Power and Energy Society General Meeting, 2011 IEEE*, pp. 1–8, July 2011.

[110] A. Paquette, M. Reno, R. Harley, and D. Divan, "Transient load sharing between inverters and synchronous generators in islanded microgrids," in *Energy Conversion Congress and Exposition (ECCE), 2012 IEEE*, pp. 2735–2742, Sept 2012.

[111] J. Guerrero, J. Vasquez, J. Matas, L. de Vicuna, and M. Castilla, "Hierarchical control of droop-controlled ac and dc microgrids: A general approach toward standardization," *Industrial Electronics, IEEE Transactions on*, vol. 58, pp. 158–172, Jan 2011.

[112] IEEE Power Engineering Society, *IEEE Std. 1547.2: Interconnecting Distributed Resources with Electric Power Systems*, 2008.

[113] IEEE Power Engineering Society, *IEEE Std. 1547.4: Design, Operation and Integration of Distributed Resource Island Systems with Electric Power Systems*, 2011.

[114] J. Liang, T. Green, G. Weiss, and Q.-C. Zhong, "Hybrid control of multiple inverters in an island-mode distribution system," in *Power Electronics Specialist Conference, 2003. PESC '03. 2003 IEEE 34th Annual*, vol. 1, pp. 61–66 vol.1, June 2003.

[115] C. Colson and M. Nehrir, "Comprehensive real-time microgrid power management and control with distributed agents," *Smart Grid, IEEE Transactions on*, vol. 4, pp. 617–627, March 2013.

[116] H. Ren, I. Dobson, and B. Carreras, "Long-term effect of the n-1 criterion on cascading line outages in an evolving power transmission grid," *Power Systems, IEEE Transactions on*, vol. 23, pp. 1217–1225, Aug 2008.

[117] A. Gkountaras, S. Dieckerhoff, and T. Sezi, "Performance analysis of hybrid microgrids applying soc-adaptive droop control," in *Power Electronics and Applications (EPE'14-ECCE Europe), 2014 16th European Conference on*, pp. 1–10, Aug 2014.

[118] T. Dragicevic, J. Guerrero, J. Vasquez, and D. Skrlec, "Supervisory control of an adaptive-droop regulated dc microgrid with battery management capability," *Power Electronics, IEEE Transactions on*, vol. 29, pp. 695–706, Feb 2014.

[119] C. Gavriluta, I. Candela, A. Luna, J. Rocabert, and P. Rodriguez, "Adaptive droop for primary control in mtdc networks with energy storage," in *Power Electronics and Applications (EPE), 2013 15th European Conference on*, pp. 1–9, Sept 2013.

[120] I. Serban, R. Teodorescu, and C. Marinescu, "Energy storage systems impact on the short-term frequency stability of distributed autonomous microgrids, an analysis using aggregate models," *Renewable Power Generation, IET*, vol. 7, pp. 531–539, Sept 2013.

[121] F. Katiraei and C. Abbey, "Diesel plant sizing and performance analysis of a remote wind-diesel microgrid," in *Power Engineering Society General Meeting, 2007. IEEE*, pp. 1–8, June 2007.

[122] G. Pistora, *Berechnung von Kurzschlussströmen und Spannungsfällen*. VDE Verlag, 2004. (in German).

[123] S. Wall, "Performance of inverter interfaced distributed generation," in *Transmission and Distribution Conference and Exposition, 2001 IEEE/PES*, vol. 2, pp. 945–950 vol.2, 2001.

[124] N. Jayawarna, N. Jenkins, M. Barnes, M. Lorentzou, S. Papthanassiou, and N. Hatziargyriou, "Safety analysis of a microgrid," in *Future Power Systems, 2005 International Conference on*, pp. 7 pp.–7, Nov 2005.

[125] R. Mallwitz, "Leistungselektronik zur wandlung photovoltaisch gewonnener energie," in *Internationaler ETG-Kongress*, VDE-Verlag Berlin, November 2013. (in German).

[126] M. Brucoli, T. Green, and J. McDonald, "Modelling and analysis of fault behaviour of inverter microgrids to aid future fault detection," in *System of Systems Engineering, 2007. SoSE '07. IEEE International Conference on*, pp. 1–6, April 2007.

[127] D. V. Tu and S. Chaitusaney, "Impacts of inverter-based distributed generation control modes on short-circuit currents in distribution systems," in *Industrial Electronics and Applications (ICIEA), 2012 7th IEEE Conference on*, pp. 1645–1650, July 2012.

[128] J. Keller and B. Kroposki, *Understanding Fault Characteristics of Inverter-Based Distributed Energy Resources*, Technical Report NREL/TP-550-46698 2010.

[129] T. Ustun, C. Ozansoy, and A. Ustun, "Fault current coefficient and time delay assignment for microgrid protection system with central protection unit," *Power Systems, IEEE Transactions on*, vol. 28, pp. 598–606, May 2013.

[130] N. Jayawarna, M. Barnes, C. Jones, and N. Jenkins, "Operating microgrid energy storage control during network faults," in *System of Systems Engineering, 2007. SoSE '07. IEEE International Conference on*, pp. 1–7, April 2007.

[131] N. Hatziargyriou, ed., *Microgrids Architectures and Control*. Wiley IEEE Press, 2014.

[132] W. Planitz, *Beiträge zur Erkennung elektrischer Fehler in Inselnetzen mit kleinem Kurzschluss-Strom und variabler Betriebsfrequenz*. Fortschritt-Berichte VDI, 1992. (in German).

[133] S. Chiang, C.-H. Lin, and C. Yen, "Current limitation control technique for parallel operation of ups inverters," in *Power Electronics Specialists Conference, 2004. PESC 04. 2004 IEEE 35th Annual*, vol. 3, pp. 1922–1926 Vol.3, June 2004.

[134] M. Hauck, *Bildung eines dreiphasigen Inselnetzes durch unabhängige Wechselrichter im Parallelbetrieb*. PhD thesis, Universität Fridericiana Karlsruhe, 2002. (in German).

[135] A. Gkountaras, S. Dieckerhoff, and T. Sezi, "Evaluation of current limiting methods for grid forming inverters in medium voltage microgrids," in *Energy Conversion Congress and Exposition (ECCE), 2015 IEEE*, Sept 2015.

[136] M. Marwali and A. Keyhani, "Control of distributed generation systems-part i: Voltages and currents control," *Power Electronics, IEEE Transactions on*, vol. 19, pp. 1541–1550, Nov 2004.

[137] C. Plet, M. Brucoli, J. McDonald, and T. Green, "Fault models of inverter-interfaced distributed generators: Experimental verification and application to fault analysis," in *Power and Energy Society General Meeting, 2011 IEEE*, pp. 1–8, July 2011.

[138] Y. W. Li and C.-N. Kao, "An accurate power control strategy for power-electronics-interfaced distributed generation units operating in a low-voltage multibus microgrid," *Power Electronics, IEEE Transactions on*, vol. 24, pp. 2977–2988, Dec 2009.

[139] W. Yao, M. Chen, J. Matas, J. Guerrero, and Z. ming Qian, "Design and analysis of the droop control method for parallel inverters considering the impact of the complex impedance on the power sharing," *Industrial Electronics, IEEE Transactions on*, vol. 58, pp. 576–588, Feb 2011.

[140] D. Vilathgamuwa, P. C. Loh, and Y. Li, "Protection of microgrids during utility voltage sags," *Industrial Electronics, IEEE Transactions on*, vol. 53, pp. 1427–1436, Oct 2006.

[141] F. Salha, F. Colas, and X. Guillaud, "Virtual resistance principle for the overcurrent protection of pwm voltage source inverter," in *Innovative Smart Grid Technologies Conference Europe (ISGT Europe), 2010 IEEE PES*, pp. 1–6, Oct 2010.

[142] A. Paquette and D. Divan, "Virtual impedance current limiting for inverters in microgrids with synchronous generators," *Industry Applications, IEEE Transactions on*, vol. 51, pp. 1630–1638, March 2015.

[143] C. Plet and T. Green, "A method of voltage limiting and distortion avoidance for islanded inverter-fed networks under fault," in *Power Electronics and Applications (EPE 2011), Proceedings of the 2011-14th European Conference on*, pp. 1–8, Aug 2011.

[144] M. Moon and R. Johnson, "Dsp control of ups inverter with over-current limit using droop method," in *Power Electronics Specialists Conference, 1999. PESC 99. 30th Annual IEEE*, vol. 1, pp. 552–557 vol.1, Aug 1999.

[145] R. Reibsch, *Entwicklung und Untersuchung von Kurzschlussstrategien für netzbildende Wechselrichter*. Diplom thesis, Fachgebiet Leistungselektronik, TU Berlin, April 2014. (in German).

[146] Bundesverband der Energie und Wasserwirtschaft, *Verordnung zu Systemdienstleistungen durch Windenergieanlagen (SDLWindV)*, May 2009. (in German).

[147] S. Grunau and F. W. Fuchs, "Effect of wind-energy power injection into weak grids," in *EWEA - European Wind Energy Association Conference*, 2012.

[148] S. Alepuz, A. Calle, S. Busquets-Monge, S. Kouro, and B. Wu, "Use of stored energy in pmsg rotor inertia for low-voltage ride-through in back-to-back npc converter-based wind power systems," *Industrial Electronics, IEEE Transactions on*, vol. 60, pp. 1787–1796, May 2013.

[149] H. Nadobny, "Entwicklung und untersuchung von netzstützenden strategien für windkraftanlagen mit vollumrichter," Master's thesis, FG Leistungselektronik, TU Berlin, 2014. (in German).

[150] L. Yang, Z. Xu, J. Ostergaard, Z. Y. Dong, and K. P. Wong, "Advanced control strategy of dfig wind turbines for power system fault ride through," *Power Systems, IEEE Transactions on*, vol. 27, pp. 713–722, May 2012.

[151] M. Mirhosseini, J. Pou, and V. Agelidis, "Single-stage inverter-based grid-connected photovoltaic power plant with ride-through capability over different types of grid faults," in *Industrial Electronics Society, IECON 2013 - 39th Annual Conference of the IEEE*, pp. 8008–8013, Nov 2013.

[152] C.-T. Lee, C.-W. Hsu, and P.-T. Cheng, "A low-voltage ride-through technique for grid-connected converters of distributed energy resources," *Industry Applications, IEEE Transactions on*, vol. 47, pp. 1821–1832, July 2011.

[153] T. Palanisamy, "Charging techniques for a universal lead-acid battery charger," in *Power Sources Symposium, 1990., Proceedings of the 34th International*, pp. 72–76, Jun 1990.

[154] H. chih Chen, C. tse Lee, P. tai Cheng, R. Teodorescu, F. Blaabjerg, and S. Bhattacharya, "A flexible low-voltage ride-through operation for the distributed generation converters," in *Power Electronics and Drive Systems (PEDS), 2013 IEEE 10th International Conference on*, pp. 1354–1359, April 2013.

[155] L. Hadjidemetriou, E. Kyriakides, and F. Blaabjerg, "A grid side converter current controller for accurate current injection under normal and fault ride through operation," in *Industrial Electronics Society, IECON 2013 - 39th Annual Conference of the IEEE*, pp. 1454–1459, Nov 2013.

[156] K. Hatipoglu, I. Fidan, and G. Radman, "Investigating effect of voltage changes on static zip load model in a microgrid environment," in *North American Power Symposium (NAPS), 2012*, pp. 1–5, Sept 2012.

[157] L. Landgraf, *Modellierung von Verteiltransformatoren für Leistungselektronikanwendungen*. Bachelor's thesis, FG Leistungselektronik TU Berlin, 2013. (in German).

List of Figures

List of Tables

Appendices

A Appendix

This appendix contains most of the parameters used in the real time simulation test scenarios presented in the previous chapters. The parameters are organized based on each generator.

A.1 Distributed generators parameters

The pu parameters of the synchronous generator model are given in the following table:

Variable	Description
E_{sbase} (V)	Peak value of rated line-to-neutral voltage
I_{sbase} (A)	Peak value of rated line current
S_{sbase} (VA)	Rated apparent power, $S_{sbase} = 3\frac{E_{sbase}I_{sbase}}{2}$
f_{base} (Hz)	Rated electrical frequency
ω_{base} (rad/sec)	Electrical angular velocity
t_{base} (sec)	Base time quantity, $t_{base} = \frac{1}{\omega_{base}}$; $\frac{d}{dt} = \frac{1}{\omega_{base}}\frac{d}{dt}$
p	Pole pairs

Table A.1: Base units for pu system

Solving the system of Eq. 3.4 the rest of the DQ parameters needed to complete the machine model can be obtained in Table A.4.
Table A.5 provides the parameters of the two controllers governing the behavior of the synchronous generator, as presented in chapter 3. Their structure can be found in Fig. 3.8 & 3.7. The selection of the upper limits was done accordingly to the provided detailed machine datasheet, as well as guidelines from [10] & [31].

Variable	Value
Rated power, S_{sbase} (kVA)	6750
Phase-to-phase rms voltage, V_{sbase} (kV)	11
Phase voltage amplitude, E_{sbase} (V)	8980
Current amplitude, I_{sbase} (A)	500
Electrical frequency, f_{base} (Hz)	50
Pole pairs, p	2
Nominal speed, n_n (rev/min)	1500
Over-speed, n_{max} (rev/min)	1800
Base impedance, Z_b (Ω)	17.93
Synchronous reactance, D-axis X_d (pu)	2.773
Synchronous reactance, Q-axis X_q (pu)	1.392
Stator winding leakage reactance, X_l (pu)	0.108
Stator winding DC resistance, R_s (pu)	0.00833

Table A.2: *Alpha SGT100* Parameters (i)

Variable	Value
Field winding DC resistance, R_f (Ω)	0.204
D-axis OC transient time constant, $T'_{d0} = T_{g,oc}$ (sec)	4.31
D-axis SC transient time constant, T'_d (sec)	0.503
D-axis OC sub-transient time constant, T''_{d0} (sec)	0.059
D-axis SC sub-transient time constant, T''_d (sec)	0.04
Q-axis OC sub-transient time constant, T''_{q0} (sec)	0.188
Q-axis SC sub-transient time constant, T''_q (sec)	0.042
Armature DC time constant, T_a (sec)	0.120
Full load torque, T_m (kNm)	35.26
Rotor inertia, J (kgm^2)	254
Exciter time constant, T_e (sec)	0.1
Machine starting time, $T_{g,m}$ (sec)	0.92
Diesel turbine time constant, T_t (sec)	0.62

Table A.3: *Alpha SGT100* Parameters (ii)

Variable	Value
Self inductance of rotor winding , L_f (pu)	0.234
D-component of mutual inductance , L_{ad} (pu)	2.65
Q-component of mutual inductance , L_{aq} (pu)	1.28
D-component of self inductance of amortisseur circuit , L_{1d} (pu)	0.223
Q-component of self inductance of amortisseur circuit , L_{1q} (pu)	0.234
Resistance of amortisseur circuit , R_1 (pu)	0.0028

Table A.4: DQ parameters of the machine

Speed governor	
Proportional gain, k_p	24.5
Integral gain, k_i	18.5
Derivative gain, k_d	6.51
Lower limit, SpG_{low} pu	0
Upper limit, SpG_{up} pu	1.1

Automatic voltage regulator	
Proportional gain, k_p	40.58
Integral gain, k_i	18.25
Derivative gain, k_d	2.75
Lower limit, AVR_{low} pu	0
Upper limit, AVR_{up} pu	2.5

Table A.5: Synchronous generator controller parameters

Table A.6 & Table A.7 obtain all parameters for the grid inverter models used in the chapters of this work. The output voltage PI controller refers to the grid forming mode, whereas the DC-link voltage controller refers to grid feeding mode of operation. The inner current controller remains the same for both cases.

Rated power, S_n (MVA)	1	2
Inverter topology	2-Level	
Grid voltage, V_g (kV)	1	
DC-link voltage, V_{DC} (kV)	1.7	
Switching frequency, f_s (kHz)	2.5	
DC-link capacitance, C_{DC} (mF)	3.5	4.8
LC(L) filter converter inductance, L_1 (mH)	1	0.86
Inductor equivalent series resistance, R_L $(m\Omega)$	3.3	1.7
LC(L) filter capacitance, C_f (mF)	0.42	0.506
LC(L) filter grid inductance, L_2 (mH)	0.31	0.26
Passive damping resistor, R_d (Ω)	0.205	0.142
Transformer leakage inductance, L_{tr} (mH)	0.15	0.079
Proportional gain of current PI controller, k_{p_c}	1.3	0.75
Integral gain of current PI controller, k_{i_c}	0.39	0.38
Proportional gain of output voltage PI controller, k_{p_v}	0.14	0.1693
Integral gain of output voltage PI controller, k_{i_v}	0.79	0.95
Proportional gain of DC-link voltage PI controller, $k_{p_{DC}}$	0.35	0.49
Integral gain of DC-link voltage PI controller, $k_{i_{DC}}$	5.9	8.1
Antiwind-up gain for output voltage PI controller, AW_v	0.06	0.08
Antiwind-up gain for current PI controller, AW_c	0.007	0.009

Table A.6: Grid inverter parameters (i)

Rated power, S_n (MVA)	3	4	5	6	6.75
Inverter topology	3-Level (NPC)				
Grid voltage, V_g (kV)	3.3				
DC-link voltage, V_{DC} (kV)	5.5				
Switching frequency, f_s (kHz)	2				
DC-link capacitance, C_{DC} (mF)	5	5.4	5.6	5.9	6.2
LC(L) filter converter inductance, L_1 (mH)	1.11	0.81	0.64	0.55	0.48
Inductor equivalent series resistance, R_L $(m\Omega)$	1.1	0.8	0.66	0.55	0.48
LC(L) filter capacitance, C_f (mF)	0.09	0.12	0.16	0.19	0.21
Passive damping resistor, R_d (Ω)	0.7	0.55	0.41	0.32	0.27
Transformer leakage inductance, L_{tr} (mH)	0.57	0.44	0.35	0.28	0.257
Proportional gain of current PI controller, k_{p_c}	1.4	1.3	0.8	0.85	0.5
Integral gain of current PI controller, k_{i_c}	1.41	1.31	0.79	0.85	0.5
Proportional gain of output voltage PI controller, k_{p_v}	0.031	0.04	0.052	0.06	0.079
Integral gain of output voltage PI controller, k_{i_v}	3.51	4.6	5.8	7	7.9
Proportional gain of DC-link voltage PI controller, k_{pDC}	0.15	0.17	0.18	0.183	0.19
Integral gain of DC-link voltage PI controller, $k_{i_{DC}}$	2.57	2.8	2.9	3.8	3.99
Antiwind-up gain for output voltage PI controller, AW_v	0.095	0.11	0.126	0.15	0.17
Antiwind-up gain for current PI controller, AW_c	0.011	0.0124	0.014	0.016	0.017

Table A.7: Grid inverter parameters (ii)

The last detailed model of a generator is the battery pack with the dc/dc converter at its output. Its parameters are given in the following table:

Variable	Value	Variable	Value
Inner resistance, R_e $(m\Omega)$	50	Switching frequency, $f_{DC/DC}$ (kHz)	1.5
Charge transfer resistance, R_{ct} $(m\Omega)$	80	Open-circuit voltage, V_{OC} (kV)	1500
Double layer capacitance, C_{dl} (F)	5.7	Design variable for current loop, s_x	0.62
Warburg resistance, R_W $(m\Omega)$	54	Desired system pole, α_1	500
Warburg capacitance, C_W (kF)	2.2	Voltage controller 1^{st} zero, β_1	24.7
DC/DC converter inductance, L_B (mH)	0.33	Voltage controller 2^{nd} zero, β_0	7.27
DC-link capacitance, C_B (mF)	6.8	Controller gain, k_{x_1}	2.65

Table A.8: 2 MW Battery pack and DC/DC controller parameters

A.2 Phase locked loop (PLL) implementation

As briefly mentioned in chapter 3, the phase balance method modified from [59], shown in Fig. A.1b was followed in this work. The typical method of controlling the q-component of the voltage to extract the voltage angle is also depicted in Fig. A.1a, [60].
Observing Fig. A.1b and Eq. 3.16, it can be seen that the phase balance method is identical to controlling the d-component of the voltage.

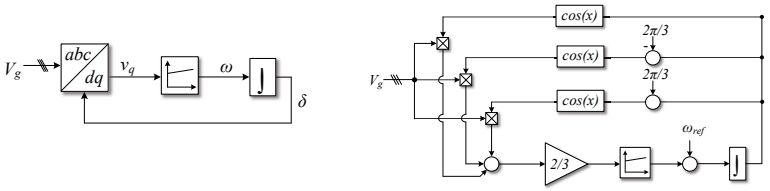

(a) Controlling the q-component (b) Phase balance method

Fig. A.1: PLL methods

A.2.1 PLL Controller Design

Q-component based The transfer function of the closed loop of the PLL depicted in Fig. A.1a can be easily calculated in Eq. A.1. In the same equation the standard transfer function with a zero is also shown, to derive the necessary relations for the PLL controllers.

$$H_s = \frac{k_p s + \frac{k_p}{T_i}}{s^2 + k_p s + \frac{k_p}{T_i}} \qquad \Leftrightarrow \qquad G(s) = \frac{2\zeta\omega_n s + \omega_n^2}{s^2 + 2\zeta\omega_n s + \omega_n^2} \tag{A.1}$$

where k_p, T_i are the PLL PI controller parameters, ζ, ω_n is the damping factor and corner frequency of the second order system. Choosing an appropriate settling time and overshoot for the system, the controller parameters can be derived.

Phase balance method Designing the PI controller of the PLL based on the phase balance method, a straight-forward guideline from [59] is followed. To achieve fast convergence and no overshooting, as well as simple hardware implementation, the controller parameters are given by the following equations:

$$c = \frac{2\pi}{M} \quad , \quad k_p = \frac{0.5}{c} \quad , \quad k_i = 0.1c \tag{A.2}$$

where k_p, k_i are the controller parameters and M is the typical number of samples per measurement cycle, $M = 64$.

A.3 Real time simulation test scenarios parameters

A.3.1 Black start and synchronization test scenarios

Table A.10 provides the necessary model parameters for the synchronization scenarios performed in chapter 4. All three distributed generators in these scenarios have the same rated power, therefore identical droop gains. Only the 2^{nd} grid forming inverter connects through a distribution line to the rest of the microgrid. For the synchronization algorithm for the grid forming inverter, the values for the pulses imply the **time point** that the pulse is applied, whereas for the restoration ramps their **duration**. The restoration ramps are applied as soon as the corresponding pulse has been applied.

Variable	Value
P/f droop gain, k_p (Hz/MW)	0.04
Q/V droop gain, k_q $(pu/MVar)$	0.05
2^{nd} inverter line length , l_2 (km)	10
Line resistance, R_{l2} (Ω)	0.5
Line inductance, L_{l2} (mH)	2.96

Table A.9: Model parameters for synchronization test scenarios (i)

	1^{st} inverter	2^{nd} inverter
Q_{set} pulse, c_v @ $t =$ (sec)	40.05	100.01
f^* pulse, c_f @ $t =$ (sec)	40.05	100.01
P_{set} pulse , c_A @ $t =$ (sec)	60	100.05
Q_{set} restoration ramp, t_v (sec)	20	1
f^* restoration ramp, t_f (sec)	20	1
P_{set} restoration ramp, t_A (sec)	20	5

Table A.10: Model parameters for synchronization test scenarios (ii)

A.3.2 Load sharing considerations test scenarios

Table A.11 provides the necessary model parameters for the first load sharing investigations test scenario.
The introduced parameters for the simulation test scenario that involves transient load sharing under the presence of a grid feeding unit are given in the following table.

Variable	Value
Initial microgrid central load , P_{init} (MW)	3.95
Step load change , P_{step} (MW)	1.2
Inverter current limitation, I_{lim} (pu)	1.1
Diesel generator P/f droop gain, $k_{p_{DG}}$ (Hz/MW)	0.05
Diesel generator Q/V droop gain, $k_{q_{DG}}$ $(pu/MVar)$	0.07
Inverter P/f droop gain, $k_{p_{inv}}$ (Hz/MW)	0.17
Inverter Q/V droop gain, $k_{q_{inv}}$ $(pu/MVar)$	0.23

Table A.11: Load sharing parameters for first test scenario

Variable	Value
Initial microgrid central load , P_{init} (MW)	6
Rated power of Grid feeding inverter , $S_{G_{Feed}}$ (MVA)	5
Distribution line length, $l_{G_{Feed}}$ (km)	5
Line resistance, R_{l2} (Ω)	0.25
Line inductance, L_{l2} (mH)	1.48
Step change for power reference of Grid feeding inverter P_{step} (pu)	0.24

Table A.12: Load sharing parameters for third test scenario

A.3.3 Short circuit strategy test scenarios

	Grid forming inverters	Grid feeding inverters
Rated power S (MVA)	2x2	1x3 & 1x5
Grid-connecting voltage V_{PCC} (kV)	1	3.3
Transformer leakage inductance X_{tr} (pu)	0.05	
Line cable inductance (mH *per* km)	0.3	
Line cable resistance (Ω *per* km)	0.06	

Table A.13: Simulation parameters for the circuit of Fig. 6.22

Universitätsverlag der TU Berlin

Modeling Techniques and Control Strategies for Inverter Dominated Microgrids

The character of modern power systems is changing rapidly and inverters are taking over a considerable part of the energy generation. A future purely inverter-based grid could be a viable solution, if its technical feasibility can be first validated. The focus of this work lies on inverter dominated microgrids, which are also mentioned as ‚hybrid' in several instances throughout the thesis. Hybrid, as far as the energy input of each generator is concerned. Conventional fossil fuel based generators are connected in parallel to renewable energy sources as well as battery systems. The main contributions of this work comprise of: The analysis of detailed models and control structures of grid inverters, synchronous generators and battery packs and the utilization of these models to formulate control strategies for distributed generators. The developed strategies accomplish objectives in a wide time scale, from maintaining stability during faults and synchronization transients as well as optimizing load flow through communication-free distributed control.

ISBN 978-3-7983-2872-3 (print)
ISBN 978-3-7983-2873-0 (online)

ISBN 978-3-7983-2872-3

http://verlag.tu-berlin.de